Joint Mineralogical Meeting
MIN 20 WIEN 23
DMG — ÖMG — SMS

You are cordially invited to attend

MinWien2023

17 to 21 September 2023

A joint meeting of the three Mineralogical Societies

DMG Deutsche Mineralogische Gesellschaft

ÖMG Österreichische Mineralogische Gesellschaft

Slovenská mineralogická spoločnosť

Topics: Mineralogical, Petrological, Geochemical Sciences, deposits & related disciplines (basic, applied & industrial topics)

Pre-confe

Male Ko

16-17 S

Guides: P. Bačik I. Bro

Conference dinner

Wednesday 20 September 2023
Festival Hall, Vienna's City Hall

Half-day tours

18-21 September, 2023

Programme

Sunday, 17 September 2023
Mineralogy for the public
Young Scientists meet each other
Opening Ceremony
ether Party

Thursday,
September 2023
Scientific sessions
Poster presentations
Industrial exhibition

Poster Prizes for young scientists
DMG - General Assembly
Public lecture

Abstracts, A - G

Conference Site: Alma Mater Rudolfina - University of Vienna
Geozentrum - UZAII, Josef-Holaubek-Platz 2, 1090 Vienna
Organisation: Institut für Mineralogie und Kristallographie
Further information: https://minwien2023.univie.ac.at
e-mail: minwien2023.mineralogie@univie.ac.at

Photo on courtesy of Stephan Wolfsried

DOI: https://doi.org/10.23689/fidgeo-6024

Experimental study of hydrothermal alteration of volcanic rocks from the Volcanic Eifel

A. Abel[1], D. Sorger[1], T. Müller[1]

[1]*Geoscience Centre Göttingen, Georg-August-University, Germany*
e-mail: angelina.abel@stud.uni-goettingen.de

Hydrothermal alteration is known to cause intensive chemical and mineralogical changes in rocks driven by element fluxes between rock and infiltrating fluid depending on alteration conditions. Volume changes are commonly the result of mineral reactions associated with hydrothermal alteration and can lead to reaction-induced fracturing. In this experimental study we investigate the replacement of leucite by analcime in mafic rocks at near-surface hydrothermal conditions. The mineral reactions are shown to generate sufficient stresses to trigger fractures and even complete disintegration of the host rock depending on starting porosity and initial mineral modes. Tephritic and phonolitc foidites were collected in the Eifel Volcanic Fields in Western Germany. Both samples exhibit a porphyritic texture with clinopyroxene as dominant phenocrysts and a matrix consisting of clinopyroxene, feldspathoids and feldspar. The samples were reacted with a Na-K-Ca-Cl solution similar to seawater composition at 200 °C and 16 bars for intervals ranging from 1 to 8 weeks. Intact rock cores were placed into a batch reactor with fluid amounts twice their mass (W/R = 2). After the experiments, BSE and EDS measurements were used to identify and characterize reaction products and textures using a W-SEM. Samples were powdered and subsequently analysed with XRD including a Rietveld refinement for quantification. The cation concentrations in the reacted fluid were analysed by ICP-OES measurements. A replacement reaction of leucite by analcime was confirmed by both, SEM and XRD measurements. ICP-OES analyses reveal an increasing K^+ concentration in the fluid while Na^+ and Ca^{2+} concentrations decreased in contrast to the staring fluid. After 2 weeks of reaction, a steady state was reached for Na^+, K^+, and Ca^{2+} concentrations. No significant difference between the two starting materials could be measured for element fluxes between rock and fluid, but a variation in porosity increase was observed. In the phonolithic foidite, starting with lower porosity, complete disintegration of the rock formation was observed, while the tephritic foidite only showed reaction-induced fracturing. As the replacement reaction is associated with a 10 % increase in volume, crystallisation pressure lead to stresses that are potentially high enough for fracturing.

Uranium incorporation in andraditic garnet

C. Ackermann[1,2], H.R. Marschall[1,2], M. Kutzschbach[3], D.C. Hezel[1,2], A.B. Woodland[1,2], L.J. Millonig[1,2], J.B. Walters[1,2], A. Schmidt[1,2]

[1]Institut für Geowissenschaften, Goethe Universität, Altenhöferallee 1, 60438 Frankfurt am Main, Germany
[2]Frankfurt Isotope and Element Research Center (FIERCE), Goethe Universität, 60438 Frankfurt am Main
[3]Institut für Angewandte Geowissenschaften, Technische Universität Berlin, Ernst-Reuter-Platz 1, 10587 Berlin, Germany
e-mail: cl.ackermann@gmx.de

Minerals of the garnet supergroup are widespread in, e.g., medium- to high-pressure metamorphic rocks, where they form an integral part of many well-established geobarometers and -thermometers. Since a few years, garnet U-Pb dating by (in-situ) LA-ICPMS is being developed. This method offers rapid analysis of a large set of samples with high spatial resolution and an age precision comparable to other geochronometers. However, the success rate of the method is hampered by our limited ability to predict the suitability of a particular sample for U-Pb dating. This limitation is due to current ambiguities regarding the incorporation of uranium (and Pb) in garnet.

In this study we investigate the incorporation of Uranium in (Ti-bearing) andraditic garnet, from alkaline igneous rocks and skarns. Previous studies on the incorporation of U into the garnet structure were restricted to elbrusite that contains U as a major component (up to 27 wt.%) in conjunction with Zr (Galuskina et al., 2010). Most natural andradite, however, contains only trace levels of U (typically 1–50 µg/g) and the substitution and incorporation mechanisms at this concentration level are unknown. Furthermore, previous studies even have claimed that U is not incorporated in garnet at all, and that the analysed U content is due to U-bearing inclusions (e.g., Lima et al., 2014). On our suite of five andradites, two of which originated from alkaline igneous rocks and three from skarn deposits, we completed a full chemical characterization. This included major and trace-element analyses and mapping by EPMA and LA-ICPMS, determination of the oxidation state of Fe by the EPMA flank method and by Mössbauer spectroscopy, and U-Pb dating by LA-ICPMS. Our results demonstrate that uranium concentrations strictly follow the oscillatory growth zoning of garnet, and one sample even exhibited sector zoning of U in garnet (Fig. 1). In general, U shows a positive correlation with Th and with Ce, and no correlation between U and Zr, showing that the elbrusite substitution vector does not (necessarily) operate at the trace-element level in andradite. Instead, U is likely incorporated in the dodecahedral site and charge compensated by octahedral divalent ions and/or tetrahedral Fe^{3+}.

Our results show that U, together with Th and the LREE, is indeed incorporated into the structure of garnet, as opposed to U being present only in submicroscopic inclusions. Also, the LREE abundance can be used as a proxy for U-enriched zones. Garnet U–Pb geochronology by LA-ICPMS on andraditic garnet will, thus, be able to reveal the age of the garnet crystallization itself, if U-rich inclusions are avoided. This conclusion agrees with mass-balance estimates presented by Millonig et al. (2020) for metamorphic garnet.

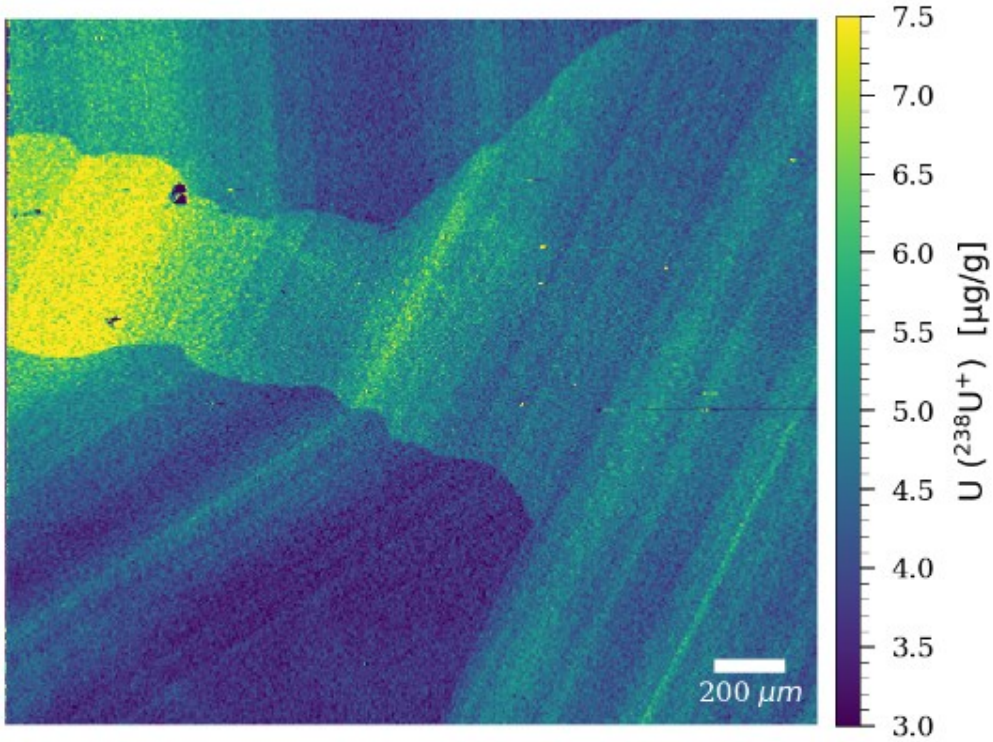

Figure 1. LA-ICP-QQQ-MS mapping of ^{238}U in a Ti-rich andradite from Magnet Cove, Arkansas. Notice the very distinct oscillatory and sector zoning.

Galuskina IO, Galuskin EV, Armbruster T, Lazic B, Kusz J, Dzierżanowski P, Gazeev VM, Pertsev NN, Prusik K, Zadov AE, Winiarski A, Wrzalik R, Gurbanov AG (2010): Elbrusite-(Zr)–A new uranian garnet from the Upper Chegem caldera, Kabardino-Balkaria, Northern Caucasus, Russia. - Amer Mineral 95, 1172-1181

Lima SM, Corfu F, Neiva AMR, Ramos JMF (2012): U-Pb ID-TIMS dating applied to U-rich inclusions in garnet. - Amer Mineral 97, 800-806

Millonig LJ, Albert R, Gerdes A, Avigad D, Dietsch C (2020): Exploring laser ablation U–Pb dating of regional metamorphic garnet The Straits Schist, Connecticut, USA. - EPSL 552, 116589

Plagioclase hosted magnetite micro-inclusions from oceanic gabbro: shape orientation and implication for bulk magnetic properties

O. Ageeva[1], G. Bian[1], G. Habler[1], R. Abart[1]

[1]University of Vienna, Department of Lithospheric Research
e-mail: olga.ageeva@univie.ac.at

In gabbro, fine-grained magnetite (MT) micro-inclusions hosted by rock-forming silicates contribute to bulk-rock magnetism. Specific crystal orientations of micro-inclusions relative to the silicate host may dramatically affect the direction and/or intensity of natural remanent magnetization (NRM) of the rock. Understanding the influence of oriented silicate-hosted magnetite micro-inclusions on rock-magnetism is important for obtaining reliable paleomagnetic data and for revealing rock magnetic fabrics, which may shed light on the mechanisms of rock formation or the tectonic evolution. We studied needle- and lath-shaped magnetite micro-inclusions in plagioclase of oceanic gabbro from the slow-spreading Mid Atlantic Ridge (11-17°N), aiming to reveal the genesis and ferromagnetic contribution of the MT inclusions to the magnetic properties of grains of host plagioclase. To this end, we combined a detailed petrographic study on magnetite-bearing plagioclase with crystal orientation analysis by electron backscatter diffraction (EBSD), measurements of the anisotropy of magnetic remanence (AMR) and alternating field (AF) demagnetization. The results show that:

(i) Needle and lath shaped MT inclusions have systematic shape orientations following eight specific crystallographic directions that coincide with the poles of low-index crystal planes/directions of the plagioclase host.

(ii) Statistically, the MT inclusions show two types of shape orientation distribution (Ageeva et al., 2022): One type is characterized by a predominantly oblate shape orientation distribution, due to a high fraction of needle-shaped inclusions oriented sub-parallel to the (010) plane of plagioclase and forming an about 30º wide "(010)-girdle". These inclusions are considered to be of primary magmatic origin (Bian et al. 2023a). The other type of shape distribution features a high fraction of inclusions oriented parallel to the c-axis of the plagioclase-host. These inclusions are interpreted as secondary (Bian et al. 2023b), replacing primary inclusions in domains where high-temperature hydrothermal alteration of plagioclase was effective.

(iii) Twinning of plagioclase following the Albite, Pericline, Carlsbad and Manebach twin laws increases the dispersion of inclusion orientations within the (010)-girdle, and strengthens the lineation caused by the presence of inclusions oriented parallel to [001] of plagioclase.

(iv) The anisotropic shape orientation distribution of the MT-inclusions causes anisotropy of magnetic remanence (AMR) in the plagioclase grains (Ageeva et al., 2022). A good correspondence between the shape orientation distribution of the MT-inclusions and AMR is established in the majority of the studied plagioclase grains: The direction of minimum magnetic remanence R_{min} is sub-perpendicular to the (010)-girdle. The direction of maximum magnetic remanence R_{max} lies in the (010)-girdle and often is close to parallel to the PL [001] direction, which often corresponds to a maximum in the shape orientation distribution of MT-inclusions in twinned plagioclase.

(v) The vector of natural remanent magnetism (NRM) tends to lay in the (010)-girdle, often parallel to the maximum in the elongation orientation distribution of inclusions or/and parallel to the direction of maximum magnetic remanence.

The results indicate that oriented needle- and lath-shaped MT micro-inclusions in plagioclase endow the grains of host plagioclase with anisotropic ferromagnetism. Consequently, in case of preferred orientation of grains of magnetite-bearing plagioclase, which is typical for many geological settings including mid-ocean ridges and layered intrusions, a magnetic fabric may form. The identified characteristics of the plagioclase magnetic anisotropy are highly relevant for petrological and paleomagnetic studies of oceanic gabbro.

Ageeva O, Habler G, Gilder SA, Schuster R, Pertsev A, Pilipenko O, Bian G, Abart R (2022): Oriented magnetite inclusions in plagioclase: Implications for the anisotropy of magnetic remanence. – Geochem Geophys Geosystems 23, e2021GC010272

Bian G, Ageeva O, Roddatis V, Li C, Pennycook TJ, Habler G, Abart R (2023a): Crystal structure controls on oriented primary magnetite micro-inclusions in plagioclase from oceanic gabbro. - J Petrol 64, egad008

Bian G, Ageeva O, Roddatis V, Habler G, Schreiber A, Abart R (2023b): Oriented secondary magnetite micro-inclusions in plagioclase from oceanic gabbro. - Amer Miner, doi: 10.2138/am-2022-8784

Magmatic-hydrothermal versus metamorphogenic origin of tungsten mineralization: Examples from the Eastern Alps

F. Altenberger[1], J.G. Raith[1], J. Krause[2], C. Auer[3], J. Weilbold[3], H. Paulick[3]

[1]Montanuniversität Leoben, Chair of Resource Mineralogy, Peter-Tunner-Straße 5, 8700 Leoben Austria
[2]Helmholtz Institute Freiberg for Resource Technology, Chemnitzer Straße. 40, 09599 Freiberg, Germany
[3]GeoSphere Austria, Department of Mineral Resources, Neulinggasse 38, 1030 Wien, Austria,
e-mail: florian.altenberger@unileoben.ac.at

The increasing demand for tungsten in the European high-tech industry is offset by an increased supply risk. Hence, this metal has been on the list of critical raw materials for the EU since 2011. Global tungsten production is primarily from ore deposit types genetically related to granitic intrusions (e.g., skarn-type, vein-type, porphyry deposits etc.) and linked with magmatic-hydrothermal processes.

Europe's largest tungsten mine is located at Felbertal in Austria in (pre-)Variscan units of the Tauern Window in the Eastern Alps. Recent studies also support a magmatic-hydrothermal model and re-interpreted the Felbertal deposit as a metamorphosed vein-stockwork scheelite deposit associated with chemically evolved, W-rich granitic melts emplaced during the Variscan orogeny (Kozlik & Raith 2017). In the Eastern Alps, however, there are still numerous smaller (sub-economic) tungsten showings that differ significantly from the Felbertal deposit in terms of their geological and mineralogical characteristics. Most of them lack a direct relation to igneous intrusions but occur proximal to large-scale tectonic structures in Paleozoic strata with metacarbonate rocks (e.g., Tux-Lanersbach, Mallnock) of the low-grade metamorphic Austroalpine units. Syngenetic/syndiagenetic sedimentary-exhalative models were suggested in the past but a metamorphogenic origin as discussed by Palmer et al. (2022) for the formation of this style of mineralization elsewhere is also plausible.

Scheelite ($CaWO_4$) is the most common tungsten mineral in the Eastern Alps and was analyzed by the combined use of cathodoluminescence, electron probe microanalysis and in-situ LA-ICP-MS analysis to determine the mineralogical-chemical signature of scheelite from different styles of tungsten mineralization. The combination of geological-mineralogical information and trace element analysis of scheelite allows to distinguish three generic mineralization styles in the Eastern Alps, i.e., 1) *intrusion-related*, 2) *polymetallic* (As, Sb, Au), and 3) *carbonate-hosted stratabound* scheelite mineralization. Mineral chemistry shows that the trace elements Na, Sr, Nb, Mo and REE+Y in particular are suitable for differentiating scheelites from these different ore forming environments.

We demonstrate that the "Felbertal" magmatic-hydrothermal signature of scheelite is distinctly different from other styles of mineralization and that these findings can be used as an indicator in future exploration to evaluate the regional tungsten potential.

Kozlik M, Raith JG (2017): Variscan metagranitoids in the central Tauern Window (Eastern Alps, Austria) and their role in the formation of the Felbertal scheelite deposit. - Lithos 278-281, 303-320

Palmer MC, Scanlan EJ, Scott JM, Farmer L, Pickering D, Wilson VJ, Oelze M, Craw D, le Roux PJ, Luo Y, Graham Pearson D, Reid MR, Stirling CH (2022): Distinct scheelite REE geochemistry and $^{87}Sr/^{86}Sr$ isotopes in proximally- and distally-sourced metamorphogenic hydrothermal systems, Otago Schist, New Zealand. - Ore Geology Reviews 144, 104800

G.O.Joe: A new software for the evaluation and correction of LA-ICP-MS concentration data

F. Altenberger[1], T. Auer[2], J. Krause[3], A. Auer[2], J. Berndt[4]

[1]Montanuniversität Leoben, Chair of Resource Mineralogy, Peter-Tunner-Straße 5, 8700 Leoben Austria
[2]Moonshot Pioneers GmbH, Dorfbeuern 35, 5152 Dorfbeuern, Salzburg, Austria
[3]Helmholtz Institute Freiberg for Resource Technology, Chemnitzer Straße 40, 09599 Freiberg, Germany
[4]Westfälische Wilhelms-Universität Münster, Corrensstraße 24, 48149 Münster, Germany
e-mail: florian.altenberger@unileoben.ac.at

Laser ablation-inductively coupled plasma-mass spectrometry (LA-ICP-MS) is widely used for spatially resolved measurements of the elemental and isotopic composition of solid materials. One of the problems of trace element analyses by LA-ICP-MS is the existence of interferences that cannot be resolved instrumentally. The software G.O.Joe was developed to calculate trace element concentrations in solid samples obtained by LA-ICP-MS analysis, offering several types of interference corrections. The software´s algorithms are written in the Dart programming language within the Flutter programming environment and follow the procedure described in Jochum et al. (2006 and 2007). G.O.Joe operates online, allowing for immediate data evaluation. It efficiently processes large datasets, offering the flexibility to change parameters at any stage of the workflow. The software also includes features for uploading and storing multiple recovery files (.gojoe), thereby preserving the information from previously evaluated datasets.

A series of three self-instructive interfaces guide the user through a straightforward process of data evaluation. Clear visualization of raw data aids the evaluation of each measurement, facilitating the selection of background and sample signals. Concurrently, inclusions or mixed analyses can be excluded. The input of instrument settings and information about the reference material follows the data processing and is used to convert the isotope count rates to element concentrations. Importantly, advanced calculations can be applied to correct the measurements for isobaric or molecular interferences and abundance sensitivity. These essential advantages of G.O.Joe are demonstrated in different case studies that focus on the mineral chemistry of tungstates (i.e., scheelite) and silicates (e.g., garnet) including the relevant correction methods.

The exported result file (.xlsx) includes the calculated element concentrations, relevant statistical parameters, input data, and instrument settings, ensuring a transparent data processing. While G.O.Joe serves as a time-efficient, transparent, and easy-to-use tool for trace element analysis for experienced LA-ICP-MS users, it is also particularly appealing to newcomers to LA-ICP-MS data analysis. Notably, it is planned as non-commercial software and does not require installation. A first version of G.O.Joe is currently in the final stages of development and will be made available with further information at https://www.gojoe.software.

Jochum KP, Stoll B, Herwig K, Willbold M (2006): Improvement of in situ Pb isotope analysis by LA-ICP-MS using a 193 nm Nd:YAG laser. - J Analyt Atomic Spectrom 21, 666-675

Jochum KP, Stoll B, Herwig K, Willbold M (2007): Validation of LA-ICP-MS trace element analysis of geological glasses using a new solid-state 193 nm Nd:YAG laser and matrix-matched calibration. - J Analyt Atomic Spectrom 22, 112-121

Crystal structure and Li-ion conductivity in $Li_7La_3Zr_{12}O_{24}$ garnets: a review

G. Amthauer[1], D. Rettenwander[2], R. Wagner[1], G.J. Redhammer[1]

[1]University of Salzburg
[2]Norwegian University of Science and Technology Trondheim
e-mail: Georg.amthauer@plus.ac.at

Recent research has shown that certain Li-oxide garnets with more than 3 Li atoms per formula unit, such as $Li_7La_3Zr_2O_{12}$, have high ionic conductivities, as well as good chemical and physical properties for use in solid-state batteries (Murugan et al. 2007).

"Garnet" is the common name for a large number of natural and synthetic metal-oxide phases. Conventional oxide garnets have the general formula $A_3B_2C_3O_{12}$ and crystallize in the cubic space group $Ia\bar{3}d$. The O^{2-} ions, in the general crystallographic positions 96*h*, form a framework with interstices occupied by the A cations, such as Ca^{2+}, Fe^{2+}, Y^{3+}, La^{3+} in the 8-fold coordinated position 24*c* (point symmetry 222), the B cations, such as Al^{3+}, Fe^{3+}, Zr^{4+}, Sn^{4+}, Sb^{5+}, etc. in the 6-fold coordinated position 16*a* (point symmetry $\bar{3}$), and the C cations, such as Li^+, Al^{3+}, Fe^{3+}, Ga^{3+}, Ti^{4+}, Si^{4+}, etc. in the 4-fold coordinated 24*d* position (point symmetry $\bar{4}$). In addition to these cation sites, there are other interstices within the oxygen framework, which are empty in the conventional garnet structure, e.g. (i) the 6-fold coordinated 16*b* positions with point symmetry 32, (ii) the 6-fold coordinated 48*g* positions with point symmetry 2, and (iii) an additional 4-fold coordinated 96*h* position with point symmetry 1. In **"$Li_7La_3Zr_2O_{12}$"** garnet (LLZO)**,** these interstices are filled by "excess" Li^+ ions giving rise to the excellent ionic conductivity.

There is a low temperature tetragonal modification of pure LLZO (SG: $I4_1/acd$) and a high temperature non quenchable cubic phase of LLZO (SG: $Ia\bar{3}d$). The tetragonal phase has distinctly lower ion conductivity than the cubic phase. Fortunately, the cubic phase can be stabilized at low temperatures by doping with low amounts of Al, Ga, and Fe (Buschmann et al. 2011; Rettenwander et al. 2016). In our contribution the results of single crystal X-ray diffraction studies will be presented. While Al-doped LLZO garnets always crystallize within the space group $Ia\bar{3}d$, Ga and Fe-doped LLZO garnets crystallize within the space group $I\bar{4}3d$ (Wagner et al. 2016). This symmetry change is combined with an increase in ionic conductivity up to 10^{-3} S cm^{-1} which is very high for those kind of solid state electrolytes used in Li-ion batteries. These results will be discussed on the basis of the slightly different topologies of both space groups, respectively. Similar structural changes are observed by the incorporation of Co (Mir et al. 2023).

Buschmann H, Dölle J, Berendts S, Kuhn A, Bottke P, Wilkening M, Heitjans P, Senyshyn A, Ehrenberg H, Lotnyk A (2011): Structure and dynamics of the fast lithium ion conductor "$Li_7La_3Zr_2O_{12}$". - Phys Chem Chem Phys 13, 19378-19392

Murugan R, Thangadurai V, Weppner W. (2007): Fast lithium ion conduction in garnet-type $Li_7La_3Zr_2O_{12}$. - Angew Chem Int Ed 46, 7778-7781

Mir MUD, Ladenstein L, Ring J, Knez D, Smetaczek S, Kubicek M, Sadeqi-Moqadam M, Ganschow S, SalagreE, Enrique G. Michel, Stefanie Lode, Gerald Kothleitner, Iulian Dugulan, Jeffrey G. Smith, Limbeck A, Fleig J, Donald J. DJ, Redhammer GJ, Daniel Rettenwander D (2023): A guideline to mitigate interfacial degradation processes in solid-state batteries caused by cross diffusion. - Adv. Funct Mater 2023, 2303680

Wagner R, Redhammer GJ, Rettenwander D, Senyshyn A, Schmidt W, Wilkening M, Amthauer G (2016): Crystal structure of garnet-related Li-ion conductor $Li_{7-3x}Ga_xLa_3Zr_2O_{12}$: Fast Li-ion conduction caused by a different cubic modification? - Chem Mater 28, 1861-1871

Rettenwander D, Redhammer G, Preishuber-Pflügl F, Cheng L, Miara L, Wagner R, Welzl A, Suard E, Doeff MM, Wilkening M, Fleig J, Amthauer G (2016): Structural and Electrochemical Consequences of Al and Ga cosubstitution in Li7La3Zr2O12 solid electrolytes. - Chem Mater 28, 2384-2392

Trace metals in hydrothermal magnetite – current knowledge, application, and experimental approaches

T. Angerer[1], R. Bakker[2], F. Melcher[3]

[1]*GeoSphere Austria, Department of Mineral Resources and Geoenergy, Vienna*
[2]*Montanuniversity Leoben, Chair of Resource Mineralogy*
[3]*Montanuniversity Leoben, Chair of Geology and Economic Geology*
e-mail: thomas.angerer@geosphere.at

Hydrothermal ore deposits host significant resources of iron and base, precious, and critical metals. In order to understand ore-forming hydrous fluid-rock interaction geoscientists analyse co-genetic mineral assemblages, fluid inclusions, elemental and isotopic geochemistry to approximate temperature, fO_2, pH, and metal and ligand composition of hydrothermal fluids. Because the accessibility or applicability of measurable proxies is often limited in a given ore deposit, there is the need for other "recorders" of fluid-rock-interaction, preferentially ubiquitous, robust, and comfortably to analyse. In recent years, trace element abundances in magnetite have become a favourite study object due to its ability to robustly record complex fluid-rock interaction (Dupuis & Beaudoin 2011; Nadoll et al. 2014; Dare et al. 2014; Canil et al. 2016; Huang et al. 2018). The understanding of trace metal signatures has grown steadily, yet is far from being satisfactory. Here, the quantification of trace metal partitioning coefficients D between mineral and fluid as functions of system variables is a crucial requirement. For magnetite, empirical D' have been determined in numerous crystal/melt experimental studies, however, only a hand full of studies have dealt with trace metal partitioning in hydrothermal systems (e.g., Ilton & Eugster 1989; Lipko et al. 2020; Simon et al. 2006; Smagunov et al. 2021). In most published setups, experimental fluids were far away from representing natural ore-forming fluids, but designed to synthesise magnetite most efficiently. Metastudies for melt, metamorphic, or aqueous fluid systems reveal that magnetite D' values for given cations vary significantly (Dare et al. 2012; Dare et al. 2014; Nadoll et al. 2014; Nadoll et al. 2017). The present contribution provides an update on the use of magnetite chemistry, the present knowledge and experimental approaches, and introduces a new joint initiative to investigate hydrothermal magnetite.

In an FWF-funded 3-year postdoctoral project at GeoSphere Austria and Montan-universität Leoben we are going to study systematically metal cation partitioning and fractionation in magnetite-rich high-T hydrothermal mineralisations. A multi-analytical approach will enable us to obtain and compare D' from hydrothermal magnetite from supercritical natural and synthetic samples. Magnetite synthesis from Fe-Si rich and trace metal doped chloride solutions can be archived in cold-seal Ni-steel autoclaves (Figure 1). Investigated systems comprise setups at ~1.5 kbar, 500-750 °C and various O_2 buffers (IM, MW, CCO, and MMO in outer capsules). Ore samples from similar systems will be selected to obtain complementary natural D' from magnetite and fluid inclusion chemistry in co-genetic transparent phases. To enhance the robustness of data, the competition for trace metals between magnetite and co-genetic phases such as silicates, sulfides, phosphates, and oxides will be considered, as well as any inter- and intra-grain chemical heterogeneity and solid inclusions at the micro- to nano-scale (Deditius et al. 2019, Verdugo-Ihl et al. 2021).

Building on the characterisation of co-existing mineral assemblages and fluid inclusions by petrography, EPMA, laser ablation ICPMS, microthermometry, and Raman spectroscopy, we plan following collaborative analyses: TEM petrography and ELNES with Liane Benning and Vladimir Roddatis from GFZ and Max Wilke from Uni Potsdam, SIMS O

isotopes with Etienne Deloule at CRPG-CNRS Nancy, fluid inclusion LA-ICPMS with Tobias Fußwinkel at RWTH Aachen, and alternative experimental setups with Bastian Joachim-Mrosko, Uni Innsbruck. We will select samples from own collections and from Robert Marschik, LMU Munich, and Christin Kehrer, TU Freiberg.

Datasets from our holistic approach will provide an unprecedented, cross-validated, reservoir of quantitative information on the behaviour of cations in magnetite under distinct high-T hydrothermal conditions. New D' datasets may allow calibrating thermometers and O_2-barometers and approximating hydrothermal fluid chemistries from mineral chemistry.

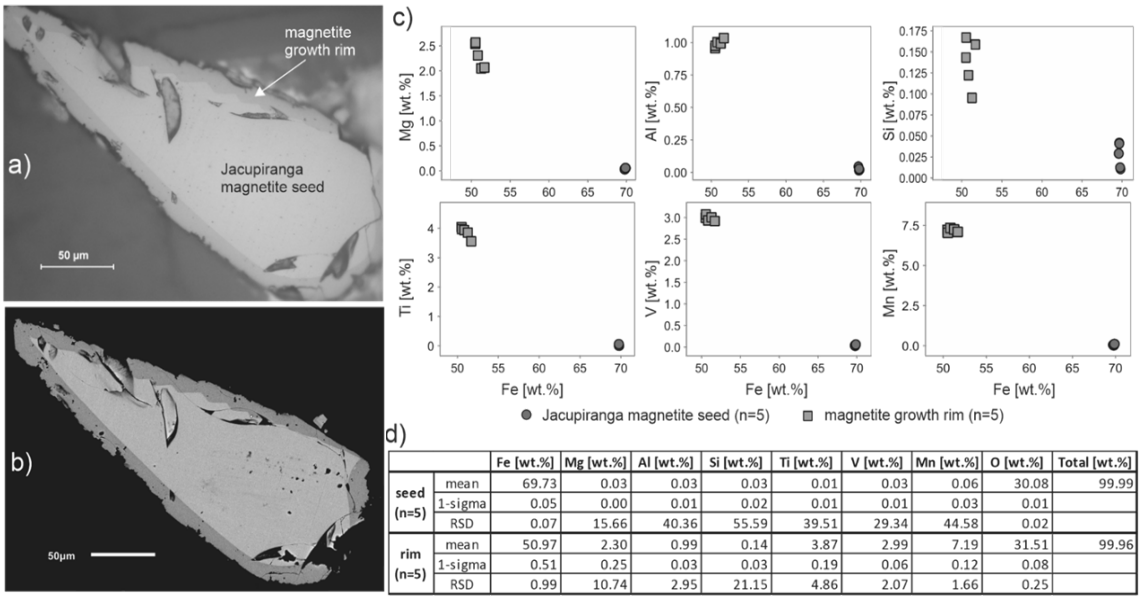

d)

		Fe [wt.%]	Mg [wt.%]	Al [wt.%]	Si [wt.%]	Ti [wt.%]	V [wt.%]	Mn [wt.%]	O [wt.%]	Total [wt.%]
seed (n=5)	mean	69.73	0.03	0.03	0.03	0.01	0.03	0.06	30.08	99.99
	1-sigma	0.05	0.00	0.01	0.02	0.01	0.01	0.03	0.01	
	RSD	0.07	15.66	40.36	55.59	39.51	29.34	44.58	0.02	
rim (n=5)	mean	50.97	2.30	0.99	0.14	3.87	2.99	7.19	31.51	99.96
	1-sigma	0.51	0.25	0.03	0.03	0.19	0.06	0.12	0.08	
	RSD	0.99	10.74	2.95	21.15	4.86	2.07	1.66	0.25	

Figure 1. Magnetite seed with growth rim from a trial experimental run of 14 days at 600 °C and 1 kbar: (a) a plain polarized reflected light micrograph and (b) SEM backscatter image, both exposing a growth rim. (c, d) EPMA elemental analyses data show the distinct chemistry between seed and rim.

Canil D, Grondahl C, Lacourse T, Pisiak LK (2016): Trace elements in magnetite from porphyry Cu–Mo–Au deposits in British Columbia, Canada. - Ore Geol Rev 72, 1116-1128

Dare SA, Barnes S-J, Beaudoin G, Méric J, Boutroy E, Potvin-Doucet C (2014): Trace elements in magnetite as petrogenetic indicators. - Mineral Deposita 49, 785-796

Dupuis C, Beaudoin G (2011): Discriminant diagrams for iron oxide trace element fingerprinting of mineral deposit types. - Mineral Deposita 46, 319-335

Huang X-W, Boutroy É, Makvandi S, Beaudoin G, Corriveau L, De Toni AF (2018): Trace element composition of iron oxides from IOCG and IOA deposits: relationship to hydrothermal alteration and deposit subtypes. - Mineral Deposita 1-28

Ilton ES, Eugster HP (1989): Base metal exchange between magnetite and a chloride-rich hydrothermal fluid. - Geochim Cosmochim Acta 53, 291-301

Lipko S, Tauson V, Bychinskii V (2020): Gold partitioning in a model multiphase mineral-hydrothermal fluid system: Distribution coefficients, speciation and segregation. - Minerals 10, 890

Nadoll P, Angerer T, Mauk JL, French D, Walshe J (2014): The chemistry of hydrothermal magnetite: A review. - Ore Geol Rev 61, 1-32

Nadoll P, Mauk JL, Hayes TS, Koenig AE, Box SE (2017): Element partitioning in magnetite under low-grade metamorphic conditions – a case study from the Proterozoic Belt Supergroup, USA. - Eur J Mineral 29, 795-805

Simon AC, Pettke T, Candela PA, Piccoli PM, Heinrich CA (2006): Copper partitioning in a melt–vapor–brine–magnetite–pyrrhotite assemblage. - Geochim Cosmochim Acta 70, 5583-5600

Smagunov, N., Tauson, V., Lipko, S., Babkin, D., Pastushkova, T., Belozerova, O. and Bryansky, N. (2021) Partitioning and Surficial Segregation of Trace Elements in Iron Oxides in Hydrothermal Fluid Systems. Minerals 11, 57

Deditius AP, Reich M, Simon AC, Suvorova A, Knipping J, Roberts MP, Rubanov S, Dodd A, Saunders M (2018): Nanogeochemistry of hydrothermal magnetite. - Contrib Mineral Petrol 173, 46

Verdugo-Ihl MR, Ciobanu CL, Cook NJ, Ehrig K, Slattery A, Courtney-Davies L, Dmitrijeva M (2021): Nanomineralogy of hydrothermal magnetite from Acropolis, South Australia: Genetic implications for iron-oxide copper gold mineralization. - Amer Mineral 106, 1273-1293

Decompression of high-grade metamorphic mafic rocks constrained by small-scale compositional layering, Gföhl Unit, Moldanubian Zone

R. Asenbaum[1], M. Racek[2], R. Abart[1]

[1]Department of Lithospheric Research, University of Vienna, Austria
[2]Institute of Petrology and Structural Geology, Faculty of Science, Charles University Prague, Czech Republic
e-mail: rene.asenbaum@univie.ac.at

Mafic–ultramafic lenses embedded in felsic granulites of the Gföhl Unit, Moldanubian Zone, are considered as mantle fragments incorporated into mid-crustal levels of the Variscan orogenic crust. We investigated a several 100 m sized mafic lens mainly formed by eclogites. Several samples were collected from loose boulders. Petrographic features provide evidence for an early HP-HT eclogite-facies peak metamorphism overprinted to variable degrees by HT granulite-facies metamorphism at lower pressures.

The primary eclogite facies mineral assemblage comprises garnet, sodium-rich clinopyroxene (up to $X_{Na\_M2} = 0.29$), kyanite, rutile and quartz. The rocks are characterized by compositional layering on the mm-scale, which is reflected by corresponding systematic variation of the compositions of garnet porphyroblasts. The garnets show homogeneous compositions in their internal domains defining plateaus, the compositional characteristics of which correlate with the compositional layering of the rocks and vary from Alm_{19} Prp_{55} Grs_{27} to $Alm_{15\text{-}18}$ $Prp_{42\text{-}50}$ $Grs_{32\text{-}43}$. The systematic variation of garnet compositions with the bulk rock compositional layering testifies to lack of equilibration on the mm scale during HP-HT eclogite-facies metamorphism.

The HT-granulite-facies overprint is evident from the breakdown of the eclogite facies mineral assemblage. This is evident, for example, from the formation of sapphirine–spinel–an-rich plagioclase symplectites in garnet supposedly replacing garnet-hosted kyanite and clinopyroxene inclusion. Another peculiar feature is represented by the partial resorption of garnet by plagioclase and clinopyroxene in the form of corrosion tubes penetrating the garnet in a worm-like fashion. Finally, garnet is partially or entirely replaced by plagioclase–spinel–orthopyroxene—clinopyroxene symplectite, where Grs-rich garnets are systematically more strongly affected by this replacement than Grs-poor garnets. Quartz is consumed during the decompression reactions and can only be found as rare relic grains. When relic quartz is surrounded by a clinopyroxene matrix, the clinopyroxene becomes successively more Si-rich due to inverse Tschermak substitution towards the relic quartz grain.

Throughout the samples and irrespective of the layer they pertain to, the garnets show similar pronounced secondary compositional zoning in the outermost 200 μm. The zoning is characterized by a strong decrease of the Grs content accompanied by an increase of the Alm and Prp contents towards the rim. The compositional changes in garnet are gradual suggesting diffusion-mediated re-equilibration at decreasing pressures, and the composition of the garnet at the interface to the rock matrix is the same throughout the specimen indicating that the rock equilibrated on the cm scale during the HT overprint.

Pressure and temperature were estimated on the basis of equilibrium phase diagrams. They indicate peak pressures above 1.8 GPa and temperatures of around 1000 °C for the primary mineral assemblages and the different garnet cores. In accordance with peak P-T, the garnet rims indicate pressures of around 1.2 GPa with the same temperature.

Considering the regional metamorphic setting of the Moldanubian Zone, the relatively localized secondary chemical zoning of garnet at its rim indicates that the granulite-facies metamorphism was remarkably short-lived and suggests rapid transport of the mafic–ultramafic lithologies from mantle depths to the mid-crustal level. Very likely incorporation of the relatively hot mafic lens into a supposedly cooler dominantly felsic environment led to immediate cooling of the mafic lens.

The position of vanadium in the crystal structure of zoisite, a variety tanzanite

P. Bačík[1,2], M. Wildner[3], J. Cempírek[4], R. Škoda[4], P. Cibula[1], T. Vaculovič[5]

[1]Comenius University in Bratislava, Faculty of Natural Sciences,
Department of Mineralogy, Petrology and Economic Geology, Ilkovičova 6, 842 15 Bratislava, Slovak Republic
[2]Earth Science Institute of the Slovak Academy of Science,
Dúbravská cesta 9, 84005 Bratislava, Slovak Republic
[3]Institut für Mineralogie und Kristallographie, Geozentrum, Universität Wien,
Josef-Holaubek-Platz 2, 1090 Wien, Austria
[4]Masaryk University, Department of Geological Sciences, Kotlářská 2, 61137 Brno, Czech Republic
[5]Department of Chemistry, Faculty of Science, Masaryk University, Kamenice 5, Brno 62500, Czech Republic
e-mail: peter.bacik@uniba.sk

Tanzanite is the most valued gemmological variety of zoisite in which V is the dominant trace element and chromophore. However, the exact position and state of V in the zoisite structure are quite enigmatic and subject to many hypotheses based mainly on spectroscopic evidence but lacking any definite structural proof. Therefore, we combined a structure refinement with optical absorption spectroscopy and used two separate theoretical approaches to shed some light on this enigma.

Structure refinement of the zoisite–tanzanite structure did not provide sufficient evidence of the V location in the zoisite structure due to the small V content in tanzanite as evidenced by Electron-Probe Micro-Analysis and Laser-Ablation Inductively Coupled Plasma Mass Spectrometry. Structure refinement of the studied sample revealed an average bond length of the less distorted $M1,2O_6$ octahedron lower than 1.90 Å. At the same time, $M3O_6$ has slightly longer bonds with an average of ca. 1.96 Å. The *M*1,2 site has a slightly higher bond valence sum (BVS) of 3.03 vu, whereas BVS of *M*3 is significantly lower (2.78 vu).

Optical absorption spectra of the studied sample with measured bands at 13 160, ~15 500, 16 350, 16 700, 18 800, 26 120, 26 650, and 34 000 (?) cm^{-1} revealed that most V is trivalent with only a small portion likely in a four-valent state. Therefore, a crystal-field superposition-model and bond-valence model calculations were applied here with two necessary basic assumptions: (1) V is at octahedral sites; (2) it can be present in two oxidation states, V^{3+} or V^{4+}. Crystal field superposition model calculations made to interpret the optical spectra indicated that V^{3+} prefers occupying the *M*1,2 site; the preference of V^{4+} was impossible to determine from the present data.

Bond-valence model calculations showed no unambiguous preference for V^{3+}, although based on the simple bond-length calculation, the preference of the *M*3-site could be suggested. In contrast, it is quite straightforward to assume that the *M*1,2 site has a more natural environment for V^{4+}. However, if the calculated octahedral distortions are taken into account, the $M1,2O_6$ octahedron shows a smaller change in distortion if occupied by V^{3+} than the $M3O_6$ octahedron.

Consequently, based on both the crystal field superposition model and bond-valence model calculations, it can be concluded that both V^{3+} and V^{4+} prefer the *M*1,2 site.

”Gold” hydrogen in natural fluid inclusions

R. J. Bakker

Resource Mineralogy, Department Applied Geoscience and Geophysics, Montanuniversity Leoben, Austria
e-mail: bakker@unileoben.ac.at

Fluid inclusions in minerals are natural storage vessels of fluids. The most common fluids that are preserved in inclusions are mixtures of water, carbon-dioxide and salts. In reduced geological environments gases such as methane (and other thermogenic alkanes, also known as “abiotic”), nitrogen, and hydrogen may be included. The present study gives some new results on the occurrence of hydrogen in natural fluid inclusions in specific geological settings.

Hydrogen is a highly volatile gas component that is not assumed to retain within the crust and mantle for a long period, but is continuously outgassed. Several natural seeps of hydrogen-rich fluids are already considered for exploration (so-called “gold” hydrogen). This hydrogen may be captured within fluid inclusions in environments with sufficient concentrations. Both seeps and fluid inclusions are aspects of the existence of a hydrogen-rich fluid that may circulate in rock. The latter may also provide information on hydrogen-rich flows in the geological past, because inclusions may preserve paleo fluid properties.

There are only few studies that mention the existence of hydrogen within fluid inclusions, that provide abundant speculative models of the origin of hydrogen within rock, usually with a lack of sufficient and relevant data. For example, both serpentinization and de-serpentinization were considered as formation processes of hydrogen. Redox conditions in rock are the main factors that define the composition of a fluid phase in deep rock, that only occupy a minor volume fraction of the system. This fluid is buffered by the coexistence of solid phases within the rock. Highly reduced conditions are common within mantle rock. Methane is closely related to the occurrence of hydrogen as both represent these reduced conditions. Similar conditions exist in Si-undersaturation igneous environments (e.g. nepheline syenite). An alternative source of hydrogen is radiolysis, but this is not sufficiently supported by fluid inclusion studies.

Hydrogen-rich fluid inclusions are analysed in three different geological settings: 1. In Upper Cretaceous strongly serpentinized mantle rock (Troodos, Cyprus); 2. In Neogene pegmatites closely related to serpentinite host-rock from metamorphosed ophiolitic-sedimentary tectonic units (Elba, Italy) (Bakker & Schilli, 2016); 3. In Mesoproterozoic metasediments of the Mt Painter Inlier, Arkaroola (Australia) (Bakker & Elburg, 2006)

Inclusions in pyroxene in strongly serpentinized areas in Troodos contain mixtures of CH_4, H_2 and H_2O (Fig. 1). Similar fluids are observed in chromite in mantle rock that is hardly affected by serpentinization (McElduff, 1989).

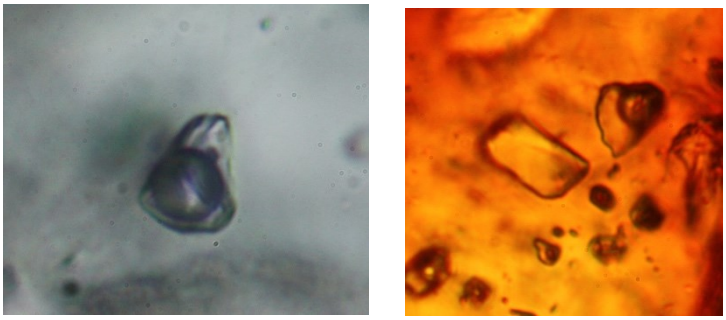

Figure 1. Fluid inclusions (ca. 10 µm) in pyroxene (left) and chromite (right).
The vapour phase is highly enriched in H_2.

Fluid inclusions in pegmatites from Elba represent a complex interaction between magmatic and metamorphic fluids. Multiple pulses of low salinity H_2O-rich magmatic and reduced metamorphic fluid stages are recorded. Magmatic fluids are characterized by the presence of minor amounts of CO_2 and H_3BO_3, whereas the metamorphic fluids contain CH_4 and H_2 (minor N_2, H_2S, and C_2H_6) that may origin from the input of more reduced fluids from serpentinites, that may completely replace the magmatic fluid. H_2-rich fluid inclusions were observed in andalusite, quartz, plagioclase, and tourmaline.

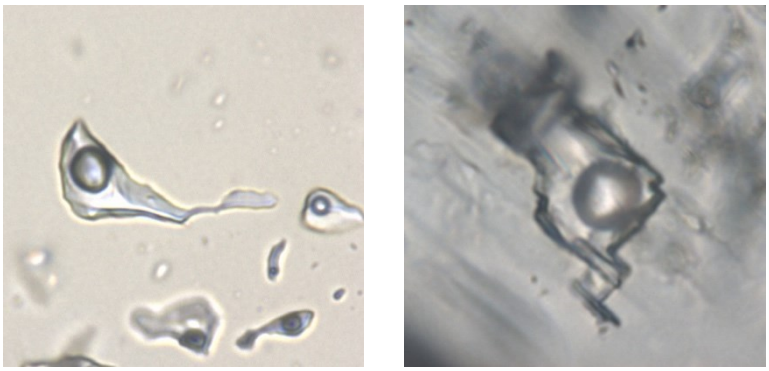

Figure 2. Fluid inclusions (ca. 20 µm) in quartz (left) and plagioclase (right) (Bakker & Schilli, 2016). The vapour phase is a mixture of mainly H_2 and CH_4.

A massive hydrothermal event in Arkaroola is demonstrated by an epithermal hematite-quartz assemblage, bladed calcite, and fluorite (Fig. 3). Fluid inclusions in fluorite contain a mixture of H_2O and H_2. The hydrogen occurs preferentially within the purple fluorite, which also includes some uranium mineralizations (radiation damage centres). These mineralizations are also proposed to be responsible for defining the colour of fluorite from green to purple that grew contemporaneously with the late hydrothermal quartz–hematite mineralization. The origin of hydrogen in fluid inclusions in fluorite is suggested to be radiolysis.

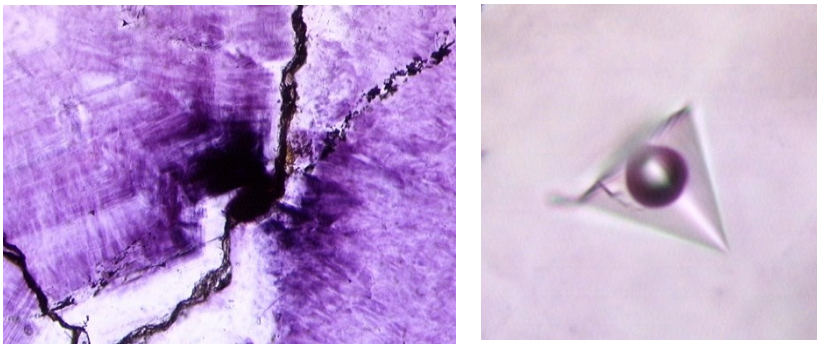

Figure 3. Purple fluorite with radiation damage centres (left), and H_2-rich fluid inclusions, ca. 10 µm (right) (Bakker & Elburg, 2006). Left image has a length of 200 µm.

Diffusion of hydrogen is a common aspect to explain the absence of hydrogen in most rock, even in environments where hydrogen is assumed to be a major fluid component. The examples illustrate that hydrogen may be preserved within fluid inclusions, similar to most fluid components.

Bakker RJ, Elburg MA (2006): A magmatic-hydrothermal transition in Arkaroola (northern Flinders Ranges, South Australia): from diopside-titanite pegmatites to hematite-quartz growth. - Contrib Mineral Petrol 152, 541

Bakker RJ, Schilli SE (2016): Formation conditions of leucogranite dykes and aplite-pegmatite dykes in the eastern Mt. Capanne plutonic complex (Elba, Italy): fluid inclusion studies in quartz, tourmaline, andalusite and plagioclase. - Mineral Petrol 110, 43

McElduff, B (1989): Inclusions in chromite from Troodos (Cyprus) and their petrological significance. - Ph.D. Thesis, Montanuniversität Leoben, Austria

The role of mineralogy: Case studies from Austr(al)ia

A. Baldermann[1]

[1]*Institute of Applied Geosciences, Graz University of Technology, NAWI Graz Geocenter, Rechbauerstraße 12, 8010 Graz, Austria*

The role and value of mineralogy in geosciences and material sciences have recently been hotly debated. In particular, the contribution of this long-established discipline in modern science and academic education has been questioned. So, what will mineralogy be focused on in the future, especially in the light of fundamental vs more applied perspectives? A closer look on mineralogy and the linked fields of crystallography, geochemistry and petrology, indicates interdisciplinary knowledge among the highly diverse fields of expertise to be key to an advanced process understanding in the various facets of human kind, climate change, resource scarcity, and technical challenges (Fig. 1).

In this contribution, various aspects of kinetic and equilibrium water-rock/mineral-gas interactions in low temperature settings are discussed, which are of high relevance for geo- and material scientist's present and future works. Focus is given on the assessment, identification and quantification of fundamental reaction mechanisms of mineral formation, dissolution, and transformation, tailoring/conditioning of (geo-)materials, and advanced understanding of the Earth system evolution throughout space and time. Case studies presented herein comprise of (i) carbonate vein infillings of vertical fractures (Erzberg), (ii) carbonation and external sulphate attack on concrete/shotcrete (Bosruck), (iii) (de)contamination/stabilization of soils using novel nZVI-bentonite nano-composites (Stadtschlaining), and (iv) environmental reconstruction of seawater chemistry by previously unrecognized archives (glauconites from the Arrowie and Amadeus basins, Australia). Recent advances in the analytical toolbox of mineralogists and (isotope) geochemists, such as in-situ Rb-Sr dating via LA-ICP-MS/MS, high-resolution optical imaging, and SEM-based automated mineral mapping, are highlighted, which offer new perspectives in geosciences and material sciences.

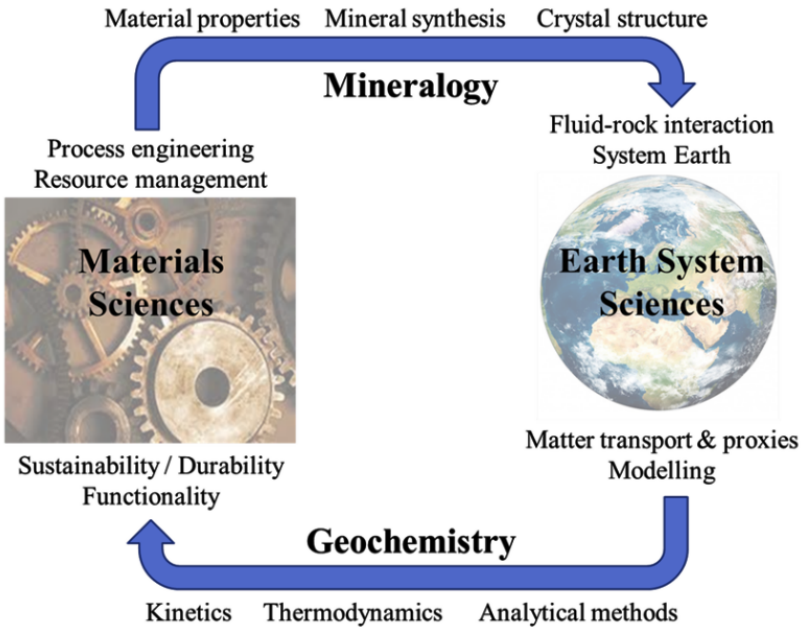

Figure 1. The role of mineralogy/geochemistry in geosciences and material sciences.

Zircon uses baddeleyite nanoparticles as fundamental building blocks

C. Ballhaus[1], H. Helmy[2], R. Wirth[3], V. Roddatis[3], T. Nagel[4], A. Schreiber[3]

[1]Universität Bonn, Germany
[2]Minia University, Egypt
[3]GFZ Potsdam, Germany
[4]Bergakademie Freiberg, Germany
e-mail: ballhaus@uni-bonn.de

Numerous experiments have been performed in the past to determine the crystallization temperature of zircon from silicate melts (Watson & Harrison 1983; Boehnke et al. 2013; Gervasoni et al. 2016; Borisov & Aranovich 2019; Marxer & Ulmer 2019). In designing those experiments, the implicit assumption was that zircon is a primary magmatic phase that crystallizes directly from the melt. Factors that determine the saturation of zircon are the Zr^{4+} (or ZrO_2) content of the melt, its silica activity ($aSiO_2$), and the cation ratio M = (Na + K + 2Ca) / (AI * Si) (Watson & Harrison 1983). The latter parameter roughly reflects the polymerization degree of a melt.

Our experiments give a somewhat different picture. We performed experiments with a phonolite composition that is modeled on a ne-normative pumice of the Laacher See, Eifel. The composition contains 60.6 SiO_2, 20.1 Al_2O_3, 2.5 FeO and CaO each, MgO 0.5, and total alkalies of 12.5 (all in wt.%). It is just corundum-normative. To prevent the introduction of zircon seeds, a synthetic aliquot of oxides and carbonates (Ca, alkalies) was synthesized. After the sample was sintered at 950 °C and CO_2 was expelled, Zr was added as $ZrCl_2O$ ICP standard solution. The mixture was then equilibrated at 1200 °C and 300 MPa in a piston cylinder press for 2 to 24 hours. After completion of the experiments, the Zr contents of the glasses were 1300 ± 160 ppm (average ± 1σ of 20 EPMA analyses).

Liquidus phases at 1200 °C were silicate melt and corundum (crn). Zircon did not crystallize because the composition is undersaturated with respect to zircon by factor of 10 (Fig. 1). Four Focussed Ion Beam (FIB) sections cut from experimental glasses showed that all charges crystallized at 1200 °C crystalline (and possibly amorphous) ZrO_2 nanophases (baddeleyite) (Fig. 2). The smallest and earliest ZrO_2 nanoparticles are found as inclusions in crn. These nanophases are as small as 3 to 4 nm and comprise perhaps 500 unit cells. They are so small because their growth was arrested after they were trapped by crn.

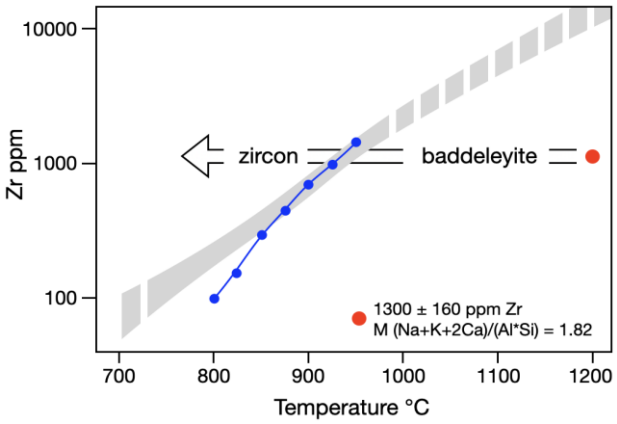

Figure 1. Starting mix with 1300 ± 160 ppm Zr - red circle. Grey - region in Zr-temperature space where magmatic zircon is stabilised (Watson & Harrison 1983; Boehnke et al. 2013; Gervasoni et al. 2016; Borisov & Aranovich, 2019). Blue symbols - zircon satutation experiments by Marxer & Ulmer (2019). For our composition zircon is expected to become stable at ~ 900 °C.

The results imply that zircon uses nanometer-sized ZrO_2 particles as building blocks when it nucleates from silicate melt. Zircon is stabilized by the reaction ZrO_2 (nanoparticle) + SiO_2 (melt) → $ZrSiO_4$ (crystal). We think that in nature this reaction is a solution-precipitation reaction. Direct crystallization of zircon from Zr^{4+} and SiO_2, if it indeed occurs, may be the exception rather than the rule. We assume that the ZrO_2 nanoparticles illustrated in Fig. 2 are stable, that they nucleated in local ΔG minima.

Many igneous rocks undersaturated with zircon may carry baddeleyite (e.g., Heaman & LeCheminant 1993). However, because baddeleyite tends to be extremely small, its presence is easily overlooked.

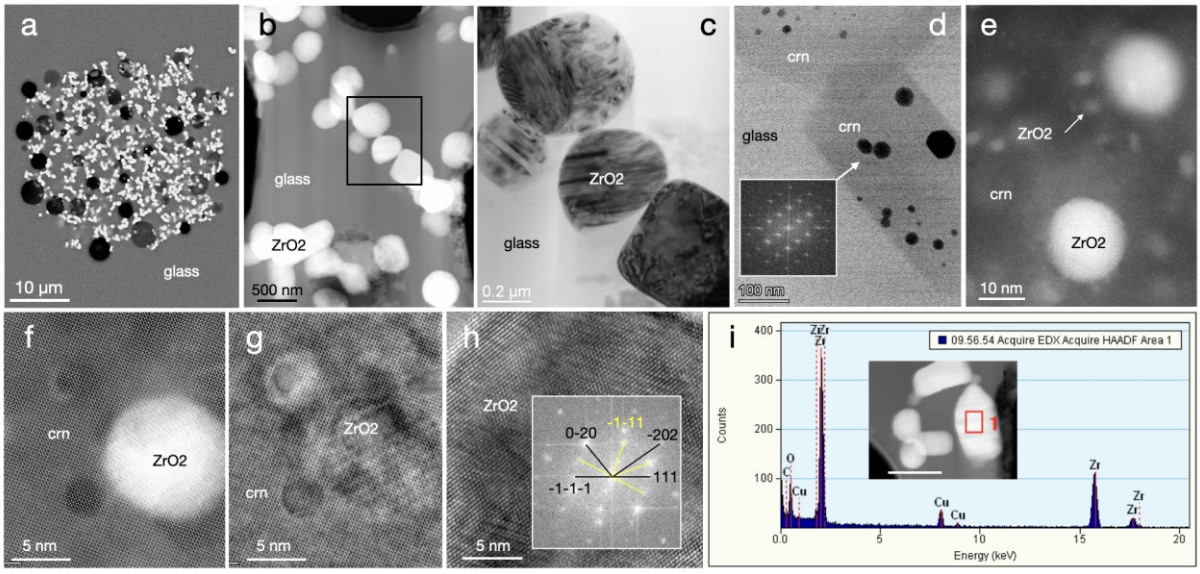

Fig. 2. ZrO_2 nanoparticles. (a) Baddeleyite (bdy) cluster in glass, after 10 hours at 1200 °C, in (b) TEM image at higher magnification; note tendency of bdy to attach and align to clusters and chains. (c) Brightfield (BF) image of twinned bdy in glass. (d) ZrO_2 nanoparticles trapped by liquidus corundum (crn). (e) HAADF image of ZrO_2 nanoparticles < 4 nm, in crn. (f) and (g) HAADF images, ZrO_2 nanoparticles in crn. (h) FFT of HREM, ZrO_2 in crn (crn in yellow). (i) Energy-dispersive spectrum to illustrate composition of bdy.

Boehnke P, Watson EB, Trail D, Harrison TM, Schmitt AK (2013): Zircon saturation re-revisited. - Chem Geol 351, 324–334

Borisov A, Aranovich L (2019): Zircon solubility in silicate melts: New experiments and probability of zircon crystallization in deeply evolved basic melts. - Chem Geol 510, 103-112

Gervasoni F, Klemme S, Rocha-Júnior ERV, Berndt J (2016): Contr Mineral Petrol 171, 21, DOI 10.1007/s00410-016-1227-y

Heaman LM, LeCheminant AN (1993): Paragenesis and U-Pb systematics of baddeleyite (ZrO_2). - Chem Geol 110, 95-126

Marxer F, Ulmer P (2019): Crystallisation and zircon saturation of calc-alkaline tonalite from the Adamello Batholith at upper crustal conditions: an experimental study. - Contr Mineral Petrol, https://doi.org/10.1007/s00410-019-1619-x

Watson EB, Harrison TM (1983): Zircon saturation revisited: temperature and composition effects in a variety of crustal magma types. - Earth Planet Sci Letters 64, 295-304

What does tourmaline reveal about the polymetamorphic evolution of the Matsch unit (Vinschgau, S-Tyrol, Italy)?

E. Bernabe[1], P. Tropper[1], C. Morelli[2], V. Mair[2]

[1]University of Innsbruck, Institute of Mineralogy and Petrography, 6020 Innsbruck, Austria
[2]Amt für Geologie und Baustoffprüfung, Autonome Provinz Bozen - Südtirol
e-mail: peter.tropper@uibk.ac.at

The currently mapped sheet Schlanders (Project CARG F012) offers the chance to carefully investigate the Austroalpine units in the Vinschgau and their tectonic contacts and to implement them into a tectonic model based on new petrological, geochronological and structural data. The Austroalpine nappe stack in the investigated area, located in the Vinschgau area (South Tyrol), comprises from bottom to top the Campo-Ortler-nappe, the Texel-unit, the Ötztal-nappe and the Matsch unit. The Matsch unit in the northern flank of the Vinschgau valley shows a clear polymetamorphic evolution history which can be well reconstructed using the spatial distribution of the alumosilicates, the chloritoid-isograd and the observation of chemical zoning patterns in garnets, which, depending on the geographical position and the geological setting, exhibit single-phase, two-phase or even three-phase compositions. Geothermobarometry yielded a strong increase in eo-Alpine temperature conditions of 500 °C and 0.8 GPa to 650 °C and 1-1.2 GPa.

Tourmaline is especially well-suited as petrogenetic indicator owing to its expansive *P–T* stability, occurrence in rocks of widely varying composition, and settings ranging from sedimentary, to hydrothermal, metamorphic, and magmatic. Tourmaline composition varies systematically with changing *P–T* conditions in its host environment. A gradual increase in Al on the Y-site, the Mg/Fe-ratio, the vacancy content at the *X* site, accompanied by increasing Ca correlates with increasing metamorphic grade for metapelitic tourmalines.

Chemically the tourmalines are dravites. The tourmalines west of the chloritoid-isograd show a complex chemical zoning pattern with 3-5 zones, whereas east of the isograde only tourmalines with 2-4 zones occur. Chemical zoning within these western tourmalines reveals in the outermost rims a sharp increase in Ca(X), Al(Y), and the vacancy on X. The inner zones most likely represent stages of the pre-Alpine metamorphic evolution since the cores contain quite high Ca(X). The 3-zone eastern tourmalines show a clear prograde evolution with increasing Ca(X), Al(Y) and Mg/Fe. Overall, the Ca-content of tourmaline as indicator of increasing Eoalpine metamorphic conditions increases from the west (0.113 apfu) to the east (0.171 apfu).

The data show that most tourmalines in the western part of the Matsch nappe record mostly zones of pre-Alpine growth and only the outermost zone with sharp increases in Al, Ca and vacancy contents represents the Eoalpine growth stage. The eastern tourmalines on the other hand show almost no pre-Alpine growth stages (e.g., Ca-rich cores) and their zoning clearly shows the Eoalpine prograde metamorphic evolution.

Unearthing genetic insights through a multi-method geochemical approach of the sediment-hosted Cu-Co Dolostone Ore Formation deposit, Namibia

V. Bertrandsson Erlandsson[1*], R. Ellmies[2], F. Melcher[1]

[1]Montanuniversität Leoben, Leoben, Austria
[2]Gecko Namibia, Swakopmund, Namibia
e-mail: of communicating viktor.erlandsson@unileoben.ac.at

The sediment-hosted Cu-Co-Zn Dolostone Ore Formation (DOF) deposit is a recently discovered Cu-Co-Zn mineralization in the Kunene region of northwestern Namibia and is the first recognized Co mineralization in Namibia (Ellmies 2018). Understanding the geological formation processes responsible for Co deposits is vital due to the ever-increasing demand of Co for modern high-tech and green technologies (Alves Dias et al. 2018). As sediment-hosted Cu-Co deposits from the Central African Copperbelt are responsible for ca. 70% of global Co supplies (USGS 2020), the DOF deposit could prove to be a valuable asset for future Co production, especially as the DOF is situated in analogous stratigraphic and tectonic settings to the Co deposits of the Central African Copperbelt (Miller 2013; Bertrandsson Erlandsson et al. 2022). This study applies an array of geochemical methods to constrain genetic aspects of the DOF deposit, with the aim of better the understanding of sediment-hosted Cu-Co deposits.

Hosted in calcareous siltstones and argillites of the Ombombo Subgroup, which is part of the Neoproterozoic Damara Supergroup, the DOF is expressed as a horizon with a bell curve-like Cu-Co-Zn distribution. The highest metal (in particular Co) enrichment is referred to as the "Main DOF horizon", whilst the extended Cu-Zn enrichment is called the "Wider DOF horizon" (Fig. 1). The sulfide mineralogy is relatively simple, with predominantly pyrite, pyrrhotite, chalcopyrite, sphalerite, linnaeite, and subordinate amounts of cobaltpentlandite and galena. Sulfides occur in six types of mineralization styles: disseminated, nodules, clusters, veins, pressure shadows, and "Events". Events are a term coined by the exploration company Gecko Namibia and refer to vein-like structures that portray both ductile and brittle deformation. (Bertrandsson Erlandsson et al. 2022).

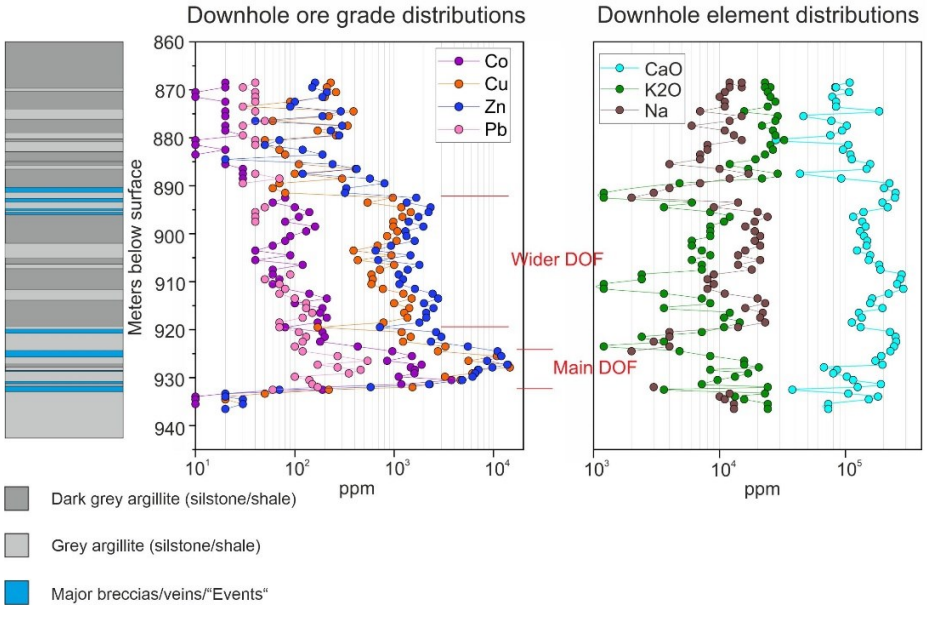

Figure 1. Simple drill core log from one of the studied DOF boreholes, with additional exploration assay data of selected elements, shown besides the drill core log.

Laser ablation inductively coupled mass spectrometry (LA-ICP-MS) analyses of sulfides from the six different mineralization styles reveal two main populations; disseminated, nodule, cluster, and Event sulfides group together (Group 1), whilst Group 2 comprises vein- and pressure shadow-hosted sulfides (Bertrandsson Erlandsson et al. 2022). The Ga-Ge-In-Mn-Fe in sphalerite geothermometer (Frenzel et al. 2016) indicates that the DOF mineralization formed at temperatures >310 °C, which suggests that they formed during regional metamorphism of the Damara Orogeny. Group 2 sulfides seem to have formed at relatively lower temperatures. This together with petrographic observations indicates that Group 2 sulfides (veins and pressure shadows) formed during a late orogenic stage of the Damara Orogeny (Bertrandsson Erlandsson et al. 2022). This interpretation is also supported by ore-associated hydrothermal monazite ages.

Petrographic evidence shows that Group 1 sulfides did not all form at once, but rather through several progressive stages. Cobalt is believed to have been initially hosted in pyrite, which was later remobilized due to changes in oxygen and/or sulfur fugacity to first form cobaltpentlandite and eventually linnaeite. It was after this that Group 1 sphalerite and chalcopyrite precipitated, partially overgrowing the preexisting sulfides. This resulted in extremely Co-rich sphalerite (>1 wt%). Atom probe tomography of this extremely Co-rich sphalerite revealed that the Co^{2+} occurs through direct substitution of Zn^{2+} (Bertrandsson Erlandsson et al. 2023).

Trace element comparison of DOF sulfides to other sediment-hosted Cu(-Co) metallogenic districts (i.e., the Polish Kupferschiefer and the Central African Copperbelt) by Random Forest and Factor analyses indicate that sulfide trace element composition is heavily host basin dependent and that local metal sources dictate the sulfide composition (Bertrandsson Erlandsson et al. *in review*).

Alves Dias P, Blagoeva D, Pavel C, Arvanitidis N (2018): Cobalt: demand-supply balances in the transition to electric mobility. - Publications Office of the EU 10, p. 97710

Bertrandsson Erlandsson V, Foltyn,K, Muchez P, Rantitsch G, Ellmies R, Melcher F (in review). Sulfide geochemistry in sediment-hosted Cu(-Co) metallogenic districts: LA-ICP-MS analyses of chalcopyrite, sphalerite, and pyrite. - Mineral Dep (*in review*)

Bertrandsson Erlandsson V, Gopon P, Waldl H, Misch D, Ellmies R, Melcher F (2023): Sphalerite as a non-traditional critical metal source: Correlative microscopy (EPMA, EBSD, and APT) of cobalt-enriched sulfides from the sediment-hosted copper-cobalt Dolostone Ore Formation deposit, Namibia. - Front Earth Sci, 10.3389/feart.2023.1171859

Bertrandsson Erlandsson V, Wallner D, Ellmies R, Raith JG, Melcher F (2022): Trace element composition of base metal sulfides from the sediment-hosted Dolostone Ore Formation (DOF) Cu-Co deposit in northwestern Namibia: Implications for ore genesis. - Jour Geoch Expl 243, 107105

Ellmies R (2018): Extensive stratiform Cu-Co-mineralisation at Okondaurie, Kunene Region. - Internal Report, Kunene Resources (Pty) Ltd. (unpublished)

Frenzel M, Hirsch T, Gutzmer J (2016): Gallium, germanium, indium, and other trace and minor elements in sphalerite as a function of deposit type—A meta-analysis. - Ore Geo Revs 76, 52–78

Miller R (2013): Comparative Stratigraphic and Geochronological Evolution of the Northern Damara Supergroup in Namibia and the Katanga Supergroup in the Lufilian Arc of Central Africa. - Geosci Canad 40, Article 2, 118–140

USGS (2020): Mineral commodity summaries 2020, DOI: 10.3133/mcs2020

Influence of deformation and fluids on Ti exchange in natural quartz

M. Bestmann[1], G. Pennacchioni[2], B. Grasemann[1], B. Huet[2], M.W.M Jones[3], C.M Kewish[4]

[1]Department of Geology, University of Vienna, 1090 Vienna, Austria
[2]Department of Geosciences, University of Padova, 35131 Padova, Italy
[3]Department of Hard Rock Geology, Geological Survey of Austria, 1030 Vienna, Austria
[4]Central Analytical Research Facility, Queensland University of Technology, Brisbane, 4000, QLD, Australia
[5]Australian Synchrotron, ANSTO, Clayton, 3186, Vic, Australia
e-mail: michel.bestmann@univie.ac.at

For over 10 years, the TitaniQ geothermometer has been used to constrain deformation temperatures in quartz-rich rocks. The calibration of the thermometer rests on the direct correlation of the titanium trace element concentration in quartz with respect to the ambient temperature. However, the processes and parameters which lead to re-equilibration of the Ti-in-quartz system during deformation are not yet fully understood. Here we analysed deformed quartz veins from the Eastern Alps (Prijakt Nappe) applying a combination of microstructural, spectroscopic, and geochemical analyses. In contrast to recent studies which highlight the importance of strain, we show that the availability of free grain boundaries, fluids, and their partitioning play the dominant role in Ti resetting towards lower concentrations in our studied case of retrograde deformation. We employ a robust analytical approach to investigate the interplay between grain-scale deformation, fluid-rock interactions, and geochemical exchange during increasing strain in the quartz mylonites. With this approach, the microstructures representing most re-equilibrated sites for the application of the titanium-in-quartz geothermometer can be readily identified, even at lower greenschist facies deformation conditions and a recrystallization regime dominated by subgrain rotation.

These coarse-grained quartz veins, that formed at amphibolite facies conditions, were overprinted by lower greenschist facies deformation to different degrees. During the overprint, subgrain rotation recrystallization was dominant during progressive deformation to ultramylonitic stages. The initial [Ti] (3.0-4.7 ppm) and cathodo-luminescence (CL) signature of the vein crystals decrease during deformation mainly depending on the availability of fluids across the microstructure. The amount of strain played a subordinate role in resetting to lower [Ti] and corresponding darker CL shades. Using a microstructurally-controlled analysis we find that the most complete re-equilibration in recrystallized aggregates ([Ti] of 0.2-0.6 pm) occurred (i) in strain shadows around quartz porphyroclasts, acting as fluid sinks, and (ii) in localized microshear zones that channelized fluid percolation. [Ti] resetting is mainly observed along wetted high angle boundaries (misorientation angle >10-15°), with partial [Ti] resetting observed along dry low angle boundaries (<10-15°). This study shows for the first time that pure subgrain rotation recrystallization in combination with dissolution-precipitation under retrograde condition provide microstructural domains suitable for the application of titanium-in-quartz geothermobarometry at deformation temperatures down to 300-350 °C.

Evolution history of plagioclase hosted Fe-Ti oxides micro-inclusions from oceanic gabbros

G. Bian[1], O. Ageeva[1], A. Kovacs[2], G. Habler[1], R. Abart[1]

[1]University of Vienna, Department of Lithospheric Research
[2]Forschungszentrum Jülich, Ernst Ruska-Centrum für Mikroskopie und Spektroskopie mit Elektronen (ER-C)
e-mail: biang92@univie.ac.at

Fe-Ti oxides are commonly observed as oriented needle- and lath-shaped micro-inclusions in plagioclase. Our study focused on these inclusions in plagioclase from oceanic gabbros in the Mid-Atlantic ridge with distinct petrogenetic histories. Previous research indicates that the inclusions formed through precipitation from Fe-bearing plagioclase at temperatures ≥ 600 °C and low oxygen fugacity (Bian et al. 2021). They subsequently undergo a complex evolution, as determined through correlated polarisation microscopy, mineral chemical analysis by electron microprobe analyzer, scanning transmission electron microscopy and crystal orientation analyses.

Two evolutionary pathways are discerned. For both pathways, the Fe-Ti oxide micro-inclusions first formed as homogeneous titanomagnetite at ≥ 600 °C upon slow cooling and/or oxygen fugacity change. Such homogeneous titanomagnetite inclusions are rarely preserved.

Along pathway A, the inclusions experienced high temperature oxidation leading to formation of ilmenite-magnetite intergrowth. Ilmenite (Ilm) is typically present as lamellae in a matrix of magnetite (Mt) with Mt{111} || Ilm(0001). The magnetite still contains a small amount of Ti. As temperature decreases < ~600 °C, the Ti-bearing magnetite exsolves into ulvospinel (Usp) and magnetite. These inclusions thus contain ilmenite lamellae and extremely fine ulvospinel lamellae within a matrix of Ti-poor magnetite.

Along pathway B, high temperature oxidation did not occur, and the inclusions are devoid of ilmenite lamellae. This indicates comparatively low fO_2 at the early stage. When cooling below ~600 °C, titanomagnetite exsolves forming magnetite-ulvospinel intergrowth with a significant proportion of ulvospinel. At a later stage, ulvospinel may be oxidised into secondary magnetite (Mt_s) and ilmenite (Ilm_s) which tend to form aggregates along the contacts between exsolved ulvospinel and magnetite. The oxidation is likely linked to relatively low-temperature hydrothermal activity.

Inclusions in both pathways may form plate shaped Ilm or relics of ilmenite particles due to preferential dissolution of magnetite. The crystallographic orientation relationships (COR) of ilmenite inclusions to the plagioclase are determined by the COR between ilmenite lamellae and the dissolved magnetite hosting the ilmenite in the first place.

Two pathways represent different cooling conditions, with the key distinction being high-temperature oxidation during early hydrothermal alteration in A, which is absent in B. Path A is typical for non-altered oceanic gabbros (Ageeva et al. 2020; Bian et al. 2021), but was also revealed in the oceanic gabbro that was affected by felsic magmatism and high temperature hydrothermal overprint (Ageeva et al. 2016).

Path B was revealed in the plagioclase of gabbroic rocks from the Vema lithospheric section, the petrogenetic history of which shows several stages (Pertsev et al. 2015). Stage I: early magmatic crystallization of coarse-grained pyroxene-plagioclase assemblage. Stage II: late magmatic syn-deformation interaction between the crystal aggregate and residual melt with local magmatic-aqueous fluid at 800-900 °C. Stage III: local high temperature (about 600 °C) reducing hydrothermal alterations as a result of interaction with brine (20-21 % NaCl) remained after low temperature (< 500 °C) interaction of seawater with mantle peridotites. Stage IV: low temperature hydrothermal alteration associated with the infiltration of seawater derivatives with salinity (< 7 wt% NaCl) during tectonic exhumation of the lithospheric section.

The microstructural and textural evolution of the Fe-Ti oxide micro-inclusions can be linked to the main events in the petrogenetic history of the gabbro. In particular, the late magmatic stage with magmatic-aqueous fluid at the Stage II catalysed precipitation of Fe-Ti oxides from plagioclase forming the micro-inclusions. The ulvospinel-magnetite inclusions appeared as a result of exsolution of titanomagnetite during the reducing hydrothermal alterations (Stage III). Likely, this process was preceded by recrystallization of primary inclusions, because in these gabbros only micro-inclusions elongated parallel to the [001] direction of plagioclase are present, which is typical for recrystallized inclusions (Bian et al. 2023). The Ilm_s-Mt_s micro-inclusions are related to water-rock interaction during the low temperature hydrothermal stage (Stage IV).

The magnetic signals recorded by plagioclase with oriented Fe-Ti oxide micro-inclusions may exhibit differing biases for pathway A and B. Consequently, comprehending the evolution of these micro-inclusions is crucial for paleomagnetic reconstructions.

Ageeva O, Habler G, Pertsev A, Abart R (2016): Orientation relationships of Fe-Ti-oxide micro-inclusions and their hosts in the oceanic gabbro. - EMC-2016. Minerals, rocks and fluids: alphabet and words of planet Earth. Book of Abstract. p. 218

Ageeva O, Bian G, Habler G, Pertsev A, Abart R (2020): Crystallographic and shape orientations of magnetite micro-inclusions in plagioclase. - Contrib Mineral Petrol 175, 95

Bian G, Ageeva O, Recnik A, Habler G, Abart R (2021): Formation pathways of oriented magnetite micro-inclusions in plagioclase from oceanic gabbro. - Contrib Mineral Petrol 176, 1–21

Bian G, Ageeva O, Roddatis V, Habler G, Schreiber A, Abart R (2023): Oriented secondary magnetite micro-inclusions in plagioclase from oceanic gabbro. - Amer Mineral, doi: 10.2138/am-2022-8784

Pertsev AN, Aranovich LY, Prokofiev VY, Bortnikov NS, Cipriani A, Simakin SS, Borisovskiy SE (2015): Signatures of Residual Melts, Magmatic and Seawater-Derived Fluids in Oceanic Lower-Crust Gabbro from the Vema Lithospheric Section, Central Atlantic. - J Petrol 56, 1069-1088

Matching crystal structure plots to "atomic-resolution" HR-TEM images

J. Birkenstock[1], S. Pokhrel[2,3,4], L. Mädler[2,3,4]

[1]University of Bremen, FB5-GEO/Crystallography & Geomaterials, Klagenfurter Straße 2-4, 28359 Bremen
[2]Faculty of Production Engineering, University of Bremen, Badgasteiner Straße 1, 28359 Bremen
[3]Leibniz Institute for Materials Engineering IWT, Badgasteiner Straße 3, 28359 Bremen
[4]MAPEX Center for Materials and Processes, University of Bremen, 28359 Bremen
e-mail: jbirken@uni-bremen.de

High-resolution TEM images of single crystals, oriented with a prominent zone axis [uvw] parallel to the electron beam, display periodic arrangements of light and dark contrast. Considering that modern TEM instruments are claimed to supply sub-Ångström ($< 10^{-10}$ m) resolution one would expect that the interpretation should be easy, assuming that the light or dark contrast represent single atoms or voids. However, only in rare cases, e.g., using deep learning algorithms, automatic recognition has been applied to simple structures like graphene layers (Madsen et al. 2018) where the orientation of the layer with respect to the beam is previously known. If certain features like open, void channels exist and the channels are oriented parallel to the beam, recognizing the orientation of the crystal structure from its observed pattern is also quite easy, as e.g., shown by MacLaren & Ramasse (2014).

For complex structures without such features, determining the orientation of the crystal structure for an observed periodic pattern of dark and light contrasts presents a more difficult task. The reasons for this are manifold: It starts with noting that the observed image usually does not represent an atomic monolayer but results from transmission through a more or less thick stack of material. Accordingly, the observed pattern is a projection of the crystal structure, which can be more or less complex in terms of the number of independent crystallographic sites, involving chemical complexes in different orientations, solid solution sites etc. Thus, a single light or dark feature in the resulting HR-TEM image may represent any of these stacked on top of each other along the viewing direction, perfectly aligned or offset by fractions of an atomic diameter. On the other hand, some atoms may "invisible" in the respective image. Furthermore, light and dark contrast may be interchanged depending on the actual settings of the microscope, e.g., with respect to focus. Accordingly, even if the crystal structure is comprehensively known, interpretation of the observed dark and light contrast in the HR-TEM image in terms of a given crystal structure can be a major challenge.

The procedure presented here for matching a certain crystal structure to an observed periodic HR-TEM pattern relies on these steps:

1) Measurements of d-spacings d_{obs} via normal distances between parallel "rows" of either light or dark contrast in several directions in the observed patterns and determination of the angle(s) between pairs of normal distance directions (i.e., between their d-spacing vectors $\mathbf{d}_{obs}$). Notes: 1. Two directions will usually be sufficient since they define a plane in space, 2. d-spacings from HR-TEM images may suffer from systematic errors (often several percent) which should be considered by a standard uncertainty (of several percent) in observed d-spacings.
2) Comparison of observed d-spacings with a list of d-spacings calculated from the crystal structure and identification of potential *hkl* planes matching them.
3) Calculation of angles between the $\mathbf{d}_{hkl}$ vectors of the identified lattice planes to find matches for the angles, too. Notes: 1. To find matches in the angles symmetrically equivalent *hkl* planes may have to be considered, too, 2. one pair of two lattice planes matching a single observed angle is usually sufficient.

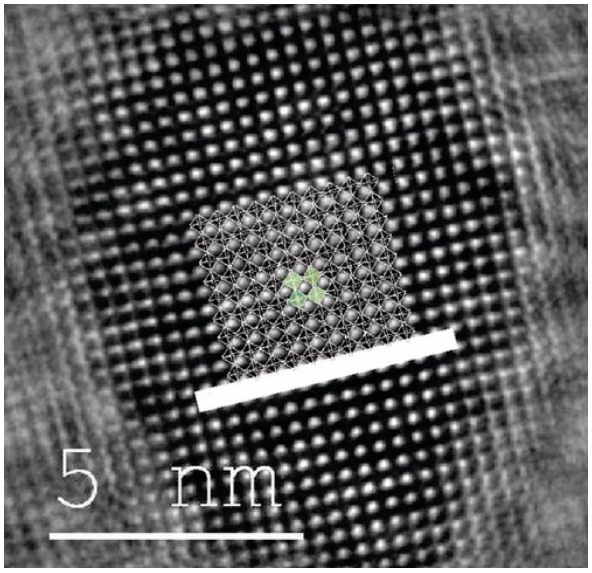

Figure 1. Crystal structure of WO_3 (monoclinic) matched onto the HR-TEM of nanoparticles of WO_3 which displays a pseudo-cubic arrangement when projected along [001] direction ([010] and [100] similar). The scale bar in the crystal structure is 5 nm, too.

4) If a match of two *hkl* planes and their angle is found, calculate the zone axis to identify the crystallographic direction [*uvw*] that was parallel to the beam on measurement.
5) In the software used for displaying the crystal structure (e.g. VESTA, Momma & Izumi, 2011), create a structure model with a sufficiently large number of unit cells, set the viewing direction to [*uvw*] from step 5. Add a scale bar matching that of the HR-TEM image.
6) Copy the crystal structure plot in semi-transparent mode onto the HR-TEM image, resize the crystal structure image to match the two scale bars.
7) Match the crystal structure to the dark and light contrast by translations and rotations of the crystal structure image on top of the HR-TEM image.

Further notes: If the identification of *hkl* was correct some details in the periodic motifs of the crystal structure or in the observed periodic dark and light contrast may be left unmatched. As a result, modifications in the crystal structure plot may have to be considered: 1) small scaling of the plot (a few percent only!), 2) display of selected crystallographic sites only since some (groups of) atoms may be missing in the contrast details, 3) as noted above, a single light or dark contrast may represent a single atom or groups of atoms from different crystallographic sites, potentially offset by fractions of an atomic diameter. Accordingly, highlighting groups of atoms, e.g., via polyhedral representation, may be indicated as well.

In this contribution we will show some well-documented, previously published examples which were taken from Pokhrel et al. (2023), Li et al. (2021), Dreyer et al. (2016), Kemmler et al. (2012), Pokhrel et al. (2009, see Figure 1).

Momma K, Izumi F (2011): VESTA3 for three-dimensional visualization of crystal, volumetric and morphology data. – J Appl Cryst 44, 1272-1276

Madsen J, Liu P, Kling J, Wagner JB, Hansen TW, Winther O, Schiøtz J (2018): A deep learning approach to identify local structures in atomic-resolution transmission electron microscopy images. - Adv Theory Simul 1, 1800037

MacLaren I, Ramasse QM (2014): Aberration-corrected scanning transmission electron microscopy for atomic-resolution studies of functional oxides. – Int Mater Rev 59, 115-131

Dreyer JAH, Pokhrel S, Birkenstock J, Hevia MG, Schowalter M, Rosenauer A, Urakawa A, Teoh WY, Mädler L (2016): Decrease of the required dopant concentration for δ-Bi_2O_3 crystal stabilization through thermal quenching during single-step flame spray pyrolysis. – Cryst Eng Comm 18, 2046-2056

Kemmler JA, Pokhrel S, Birkenstock J, Schowalter M, Rosenauer A, Bârsan N, Weimar U, Mädler L (2012): Quenched, nanocrystalline $In_4Sn_3O_{12}$ high temperature phase for gas sensing applications. – Sens Actuators B Chem 161, 740-747

Li H, Erinmwingbovo C, Birkenstock J, Schowalter M, Rosenauer A, La Mantia F, Mädler L, Pokhrel S (2021): Double flame-fabricated high-performance $AlPO_4$/$LiMn_2O_4$ cathode material for Li-ion batteries. – ACS Appl Energy Mater 4, 4428-4443

Pokhrel S, Birkenstock J, Schowalter M, Rosenauer A, Mädler L (2009): Growth of ultrafine single crystalline WO_3 nanoparticles using flame spray pyrolysis. – Cryst Growth Des 10, 632-639

Pokhrel S, Stahl J, Groeneveld JD, Schowalter M, Rosenauer A, Birkenstock J, Mädler L (2023): Flame aerosol synthesis of metal sulfides at high temperature in oxygen-lean atmosphere. – Adv Mater 2023, 2211104

$CaCO_3$ precipitation in drainage systems of subsurface infrastructure – Monitoring approaches and crystal growth control

R. Boch[1], M. Pettauer[1], S. Eichinger[2], A. Leis[3], H. Wagner[2], M. Dietzel[1]

[1]Graz University of Technology, Institute of Applied Geosciences
[2]ÖBB Infrastruktur AG, SAE, FB Bautechnik-Tunnelbau
[3]JR-AquaConSol GmbH
e-mail: ronny.boch@tugraz.at

Methodological approaches and enhanced process understanding interconnecting fundamental research with (geo)technical settings and problems benefit from each other regarding the calcium carbonate chemical system (cf. Boch 2020). The effective draining of subsurface infrastructure is frequently faced with unwanted mineral precipitation (Fig. 1A) based on elevated mineral and gas contents of the discharging groundwater being of high relevance for cleaning downtimes and maintenance of the infrastructure (Eichinger et al. 2020). Owing to regional geology in Austria (limestones, calcareous contents) and construction materials used in subsurface infrastructure (concrete, mortar), carbonate deposits consisting of various $CaCO_3$ polymorphs and accessory constituents are most abundant in the drainage systems (Fig. 1B) next to iron precipitates and interacting biomass (bacterial biofilms).

In the context of existing subsurface infrastructure (e.g. Semmering highway tunnels) and new excavations (e.g. Koralmtunnel) the recent years strongly increased the understanding of critical processes based on in-situ monitoring campaigns as well as related laboratory analyses and computer modelling. The drainage system and maintenance strategies were adapted based on the implementation of an underground "sinter test track" (Fig. 1C) and local test fields with typical construction materials but different constructive designs (Wedenig et al. 2022). The on-site and online application of sensors/data loggers and mobile instrumentation in combination with sample analyses provided new insights to water-gas-mineral-biology-substrate interaction and to the major controls of calcium carbonate precipitation.

An approach to systematically influence the nucleation and crystal growth of the unwanted deposits consists in the application of specific chemical additives ("green inhibitors") to the ground-/drainage waters. In laboratory and field tests various substances (e.g. polyaspartic acid) and concentrations were investigated and a new test procedure was developed (Wedenig et al. 2021). This resulted in new insights concerning relevant parameters such as $CaCO_3$ supersaturation, pCO_2, Mg/Ca and water flow conditions in relation to mineralogy (polymorphism; Fig. 1D), crystal shapes/sizes, substrate effects (e.g. different plastic types) and further regarding proactive controls on fabrics and material consistency (hardness) of the deposits.

Figure 1. Diverse mineral precipitates (A) in the course of continuous groundwater discharge underground can block a tunnel drainage system (B) and were investigated by in-situ field tests (C) targeting an increased process understanding of the precipitation conditions (e.g. D: $CaCO_3$ polymorphism) as well as efficient countermeasures (e.g. optimized drainage design, addition of inhibitors).

Boch R (2020): Carbonates in natural and geotechnical settings – Chemical sediments as environmental archives. – Jb Geol.-BA 159, 67-130

Eichinger S, Boch R, Leis A, Koraimann G, Grengg C, Domberger G, Nachtnebel M, Schwab C, Dietzel M (2020): Scale deposits in tunnel drainage systems – A study on fabrics and formation mechanisms. – Science of the Total Environment 718, 137140

Wedenig M, Boch R, Leis A, Wagner H, Dietzel M (2021): Green inhibitor performance against $CaCO_3$ scaling: Rate-modeling aided test procedure. – Crystal Growth and Design 21, 4, 1959-1971

Wedenig M, Eichinger S, Boch R, Leis A, Wagner H, Dietzel M (2022): Understanding of tunnel drainage scale formation by in-situ monitoring. – Tunnelling and Underground Space Technology, 131(A43), 104853

Assessing enrichment efficiency: A study of mineralogical and physical characteristics of Pb-Zn ore from Erzgebirge, Germany

A. Bravo[1], O. Popov[1], H. Lieberwirth[1]

[1]Institute for Minerals Processing Machines and Recycling Systems Technology (IART), Technische Universität Bergakademie Freiberg, Germany
e-mail: bravo@iart.tu-freiberg.de

The mineralogical and physical properties of minerals play a crucial role in understanding their behaviour during the comminution process, where materials are reduced into different sizes. Accurate determination of the characteristics of mineral phases present in the materials is essential to assess their potential selectivity during comminution. Then differences in the physical properties of gangue and ore minerals can be exploited. As a result, the valuable minerals appear in a different particle size than the gangue material and can be separated by classifying techniques.

In this study, an integrated assessment was conducted on samples of Pb-Zn ore from Reiche Zeche, located in Saxony's prominent mining district in Germany, the Ore Mountains, Erzgebirge Region. The Ore Mountains are mainly composed of metasediments (grey gneisses) and metamagmatites (red and grey gneisses) and exhibit hydrothermal polymetallic mineralisation including lead, zinc and silver. The veins are commonly categorised based on their orientation and mineral associations.

Smaller vein-like deposits along with the typical host rock gneiss from Freiberg, have been chosen as research environment for evaluating the enrichment of different sieve classes before and after undergoing jaw crusher and cross Beater mill processes. The mineralogical characterisation was performed using automated mineralogy through Mineral Liberation Analysis (MLA). The material's properties, such as the Point Load strength index, Vickers Hardness Number, and fracture toughness, were determined. MLA provided information on particle size distribution, liberation degree, association, and modal mineralogy for each fraction. The preliminary results showed an enrichment of smaller sieve classes for specific phases, including chalcopyrite, galena, sphalerite, and pyrite. These results were correlated with the rock's physical properties, including textural observations, as well as the behaviour of grains and grain boundaries within the rock.

Reviewing the formation and transformation behaviour of amorphous calcium carbonate: implications for environmental proxies

J-M. Brazier[1,2], M. Pettauer[1], K.E. Goetschl[1], M. Dietzel[1]

[1]Graz University of Technology, Institute of Applied Geosciences, Rechbauerstraße 12, 8010 Graz, Austria
[2]Current address: University of Bern, Institute of Geological Sciences, Baltzerstraße 1+3, 3012 Bern, Switzerland
e-mail: michael.wedenig@tugraz.at

The elemental and isotopic compositions of $CaCO_3$ minerals are commonly used as proxies to reconstruct the (paleo)environmental conditions that existed during their formation. Amorphous calcium carbonate (ACC) is known to be a metastable phase and a precursor to crystalline phases within the so-called "non-classical" nucleation pathway. Various factors can influence its formation, lifespan, structure, and transformation pathways, raising questions regarding the reliability of the crystalline phase resulting from precursor transformation as an archive for (paleo)environmental conditions. Evaluating the elemental and isotopic composition of such crystalline phases requires considerations of the specific pathways of $CaCO_3$ formation and transformation, as well as the system conditions, such as reaction kinetics versus equilibrium. In this review, we discuss the elemental and isotopic fractionations between ACC/crystalline $CaCO_3$ and the precipitating solution, focusing on structural characterization, ion exchange behaviour, precipitation kinetics, and transformation behaviour in open versus closed systems.

Monazite stability as a tool used for identification of granite stacking (a case study from the Western Carpathians)

Igor Broska[1], Igor Petrík[1]

[1]*Earth Science Institute Slovak Academy of Sciences, 840 05 Bratislava*
e-mail: Igor.Broska@savba.sk

The presence of monazite or allanite in granites is not only an important aspect of assessing their parental rocks to the I- or S-type, but their mutual relationship can also help to estimate PTX conditions in a given magmatic system. In the Western Carpathians, allanite and monazite became an effective tool for discrimination Variscan granites in terms of their I- or S-types affinity, in addition to the bulk-rock granite composition (Petrík & Broska 1994). For the S-type granites, typical is a reduction paragenesis of accessory ilmenite, monazite and apatite with higher content of Mn (Mn in reduced bivalent form easily replaces Ca). On the other hand, the I-type granites were identified by the presence of allanite, higher content of apatite with a low Mn and Fe, titanomagnetite, phlogopite (Mg-biotite), titanite, late pure magnetite, and locally also amphibole indicating a higher oxidation stage in this magmatic system compared to the S-type. It probably reflects initially a higher water content manifested also by late or post-magmatic oxidation of titanomagnetite, biotite and allanite.

Primary magmatic monazite and allanite: In arc orogenic granites, such as the Western Carpathian granites the presence of monazite is determined by PTX conditions, where parameter X represents the content of CaO and the REE`s. At a higher ratio of CaO/REE in granite the allanite is stable (Gieré & Sorensen 2004; Janots et al. 2008; Spear 2010). The S-type granites, where the whole-rock CaO content greater than 2.5 wt % stabilises allanite can also produce a monazite due to local decrease of CaO activity, e.g. after massive crystallization of plagioclase which was at the beginning suppressed by higher water contents (Johannes and Holtz 1996). A relict allanite in such case, as a precursor of monazite, was documented in accessory paragenesis of granites from the Tribeč and the Malé Karpaty Mts. Alternatively, some Western Carpathian S-type granites, rich in the REEs, may also have changed early allanite for monazite due to a pressure drop whereby their PT path crosses the Aln/Mnz boundary and the parent granites were emplaced into upper part of the crust. Monazite in this sense represents a mineral whose dating can records the cooling time of the parental granite system.

Monazite breakdown to allanite and REE epidote: In the granites of the Alpine Tatric Unit, monazite is typically stable or only weakly altered, on the other hand (Fig. 1A), the granites from the higher Alpine nappes as the Fatric and Veporic units, show monazite breakdown forming coronas of the apatite and allanite (Fig. 1B). The monazite breakdown into apatite-allanite coronas is facilitated by the higher content of CaO, Al_2O_3, and LREE, and alkali-rich fluids (Budzyń et al. 2011). The monazite breakdown in metamorphic granites is illustrated by stability diagrams of monazite – allanite (Spear, 2010). In the case of the Western Carpathians in the Tribeč crystalline basement, the monazite breakdown in high CaO granites is predicted for the estimated pressure of ca 4 kbar at the temperature of about 450 °C due to crossing the monazite/allanite stability boundary by cooling along a near-isobaric PT trajectory (Broska et al. in prep.). Since an Alpine monazite has not been detected in these granites, the

breakdown of monazite has occurred due to prolonged residence in deeper parts of the Earth's crust achieving the isobaric trajectory. On the other hand, the non-altered monazite presented in the underlying Tatric granites in this Tribeč granite nappe system was preserved by the rapid ascent of granite into the upper crust, where the PT trajectory is close to isothermal. The rapid cooling here in the Tribeč field documents the shallow intrusion of the granites into phyllites.

Granite duplex: The undeformed S-type granites with unaltered monazite in the Tribeč Mts are found at deep part of the crystalline basement, i.e. these underlying granites are attributed to the Tatric Unit where unaltered monazite typically occursed. On the other hand, the granites from the higher, crest part of the mountain range, are metamorphosed and hydrothermally affected (altered) and contain monazite with breakdown coronas (Fig. 1B). Since both granite blocks, the upper metamorphic and the lower non-metamorphic, are similar in the age, the different monazite behaviour indicates existence of two different granite blocks. They had been originally at the time of generation during Variscan orogen at different crustal positions because otherwise they would not have shown different monazite responses. Moreover, the overlying granites with altered monazite are Alpine metamorphosed in PT conditions close to those known in the Veporic or Fatric unit but not high enough to produce a new Alpine monazite. Thus, in the present position of the Tribeč basement, there are two granite blocks one above the other, metamorphic block thrust on the non-metamorphic one. The stacking of the metamorphosed over non-metamorphosed block was flat and inclined to the northwest at an angle of about 20°, and in the present position represents an Alpine granite duplex. With altered granites Lower Triassic quartzites of the Lúžna formation were probably also moved, from which Uher et al. (2009) described a hydrothermal vein mineralization associated with fluids from the underlying granites forming in quartzites spectacular lazulite. The age of granite stacking is indicated by Ar/Ar age from muscovite of the overlying granites and it gives the age of 78 Ma. It postdates the stacking, since the dated muscovites have not been deformed. The identification of Tribeč granite alpine duplex can be considered as an example of the use of monazite stability for solving of geodynamic events.

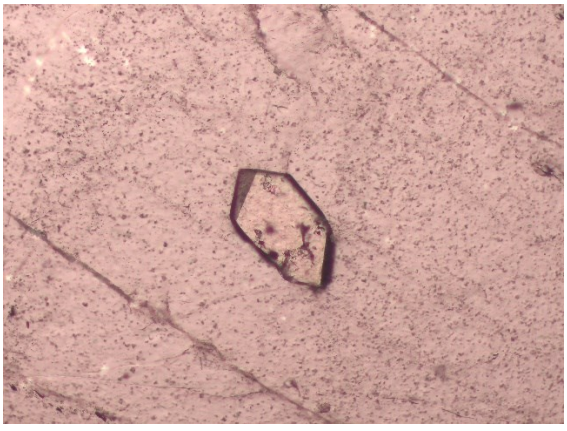

Fig 1A Stable monazite from low a CaO S-type granite; Nízke Tatry Mts, Tatric Unit. (Photo: I. Petrík, polarised light, lengths of monazite crystal is ca 300 μm).

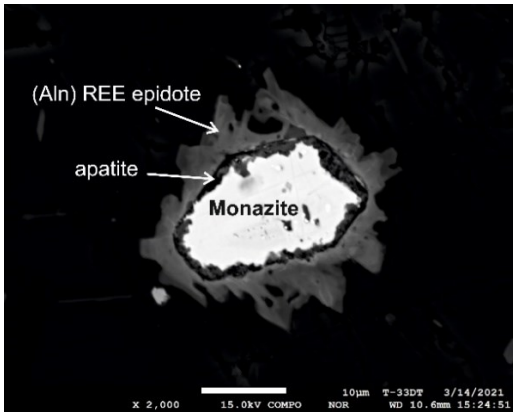

Fig. 1B Monazite breakdown into coronas of apatite and allanite in the S-type granite (Tribeč Mts. Fatric Unit). BSE image.

Acknowledgement: Authors thank to project VEGA 75/20 for financial support.

Budzyn B, Harlov D, Williams ML, Jercinivic MJ (2011): Experimental determination of stability relations between monazite, fluorapatite, allanite, and REE-epidote as a function of pressure, temperature, and fluid composition. - Amer Miner 96, 1547–1567

Giieré R, Sorensen SS (2004): Allanite and other REE-rich epidote-group minerals. In: Liebscher A, Franz G (eds): Epidotes. - Rev Miner Geochem 56, 431-493, http://dx.doi.org/10.2138/gsrmg.56.1.431

Janots E, Engi M, Berger A, Allanz J, Schwarz J-O, Spandler C. (2008): Prograde metamorphic sequence of REE-minerals in pelitic rocks of the Central Alps: implications for allanite-monazite-xenotime phase relations from 250 to 610 °C. - J Metamorphic Geol 26, 509-526

Petrík I, Broska I (1994): Petrology of two granite types from the Tribeč Mts., Western Carpathians: an example of allanite-magnetite vs. monazite-ilmenite dichotomy. - Geol J 29, 59-78, https://doi.org/10.1002/gj.3350290106.

Uher P, Mikuš T, Milovský R, Biroň A, Spišiak J, Lipka J, Jahn J (2009): Lazulite and Ba, Sr, Ca, K-rich phosphates-sulphates in quartz veins from metaquartzites of Tribeč Mountaions, Western Carpathians, Slovakia: Compositional variations and evolution. - Lithos 112, 447-460

Spear FS (2010): Monazite-allanite phase relations in metapelites. - Chem Geol 279, 55-62

Accessory minerals in the Isua Supracrustal Belt

H. Brüschke[1], D. Sorger[1], A. Kronz[1], A.A.G. Webb[2], T. Müller[1]

[1]Geoscience Center Göttingen, Georg-August-University Göttingen, Germany
[2]Department of Earth Sciences, The University of Hong Kong, Hong Kong, China
email: h.brueschke@stud.uni-goettingen.de

The Isua supracrustal belt (ISB) is an example of Archean crustal evolution and well-known as it hosts Earth's oldest 10s-of-km scale supracrustal rocks. However, the conditions and timing of its metamorphic evolution are controversially debated. Most importantly, this knowledge is underpinning the different existing hypothesis of Eoarchean vs. Neoarchean tectono-metamorphic events and geodynamic models of horizontal vs. vertical tectonic evolution. Recent studies have shed light on the metamorphic conditions based on geothermobarometry and phase equilibria modeling of major rock forming minerals. However, data from accessory minerals in the ISB have only been sparsely studied despite their potential to better constrain the metamorphic evolution of the belt. In this work, we study structure, composition, and its spatial variation of the accessory phases, especially their rare earth element (REE) contents.

A total of 5 samples with bulk composition resembling so-called "mafic pelites" have been investigated. The typical mineral assemblage comprises garnet porphyroblasts, biotite, quartz and chlorite being the major rock forming phases. Garnet porphyroblasts indicate two stages of garnet growth marked by an inclusion-rich core (M1) and inclusion-poor overgrowth rim (M2). Zircon, monazite, rutile and ilmenite are the most prominent accessory minerals present in the studied lithology.

Backscattered electron images and polarization microscopy were used to petrographically describe the textural context. Major and trace elements have been analyzed using an electron microprobe.

Preliminary results reveal that zircons occur as 5 to 10 microns inclusions within garnet (both core and rim), biotite and chlorite. No visible CL pattern could be found in any of the studied grains indicating substantial metamictization. Despite the presence of zircons in the rocks, Zr-in-Rutile measurements of matrix grains are often below or around detection limit of the electron microprobe, resulting in unresolvable low temperature estimates.

Monazite grains occur as individual grains in the matrix and as inclusions in both, rim and core of garnet porphyroblasts. Rare earth element analysis indicates the absence of an Eu-anomaly in all types of monazites, suggesting growth in the absence of feldspar. Monazite inclusions in garnet cores exhibit slightly higher Sm, Gd and Y contents compared to monazite grains in garnet rims and matrix. One possible reason for the higher content of MREE is that this type of monazite was formed in absence of a competitor phase such as garnet or apatite. If true, this possibly indicates a monazite formation either before the first M1 garnet growth stage or in a different environment.

The preliminary results highlight the potential to reconstruct the metamorphic evolution of the belt in more detail. For example, variations in the REE content of accessory phases potentially shed light on the presence or absence of metamorphic index minerals during formation of accessory phases. Such knowledge provides additional information on the timing of the major tectonometamorphic event (M1) and thus feeds into the interpretation of the geodynamic evolution of the ISB.

Do chromium isotope compositions record signs of oxygenation in the Campbellrand-Malmani Platform (2.56 to 2.52 Ga, South Africa)?

S. Bruggmann[1], C. Thomazo[2], J. Marin Carbonne[1], S. Jaccard[1]

[1]University of Lausanne
[2]University of Burgundy
e-mail: sylvie.bruggmann@unil.ch

The oxygenation history of Earth's surface remains a highly investigated topic, with an increasing number of studies indicating a dynamic change from anoxic to oxic conditions in the Precambrian. The Campbellrand-Malmani platform (Transvaal Supergroup, South Africa) was deposited in a shallow marine environment between 2.56 and 2.52 Ga (Sumner and Grotzinger 2004), just before the Great Oxidation Event. The sedimentary rocks hold a large variety of stromatolites, which can produce oxygen through photosynthetic cyanobacteria. While some studies find indications of oxygen production (e.g., Czaja et al. 2012), post-depositional alteration can challenge interpretations of data from non-traditional isotope systems.

We present Cr isotope compositions (δ^{53}Cr) and concentration data (trace metals) in sedimentary rocks from the Campbellrand-Malmani platform to better constrain the robustness of the Cr isotope system to post-depositional changes. Preliminary results show that even though the detrital contribution is low, most dolostone and chert samples show δ^{53}Cr values of around -0.12 ± 0.10 ‰ (2SD, n = 14) and are thus similar to the detrital δ^{53}Cr value. Only two samples fall off the detrital value, with one dolostones sample showing a positive δ^{53}Cr value of 0.26 ± 0.05 ‰ (2SE).

Our preliminary results indicate that many of the δ^{53}Cr values in the studied dolostones and cherts were overprinted by post-depositional processes. With the aid of additional isotope (S, N isotope compositions) and auxiliary data (trace metals), we seek to characterise the drivers of the observed δ^{53}Cr values.

Czaja A, Johnson M, Roden E, Beard B, Voegelin A, Nägler T, Beukes N, Wille M (2012): Evidence from free oxygen in the Neoarchean ocean based on coupled iron-molybdenum isotope fractionation. – Geochim Cosmochim Acta 86, 118-137

Sumner D, Grotzinger J (2004): Implications for Neoarchean ocean chemistry from primary carbonate mineralogy of the Campbellrand-Malmani Platform, South Africa. – Sedimentology 51, 1273-1299

Pressure-Temperature structure of the Makbal UHP complex (NW Kyrgyzstan)

D. Brunner[1], E. Skrzypek[1], S. Schorn[1], C. Hauzenberger[1], K. Stüwe[1], R. Orozbaev[2]

[1]Institute of Earth Sciences, University of Graz
[2]Institute of Geology, Kyrgyz National Academy of Sciences
e-mail: danie.brunner@edu.uni-graz.at

The Makbal ultra-high-pressure (UHP) complex in NW Kyrgyzstan is one of several (ultra-)high-pressure [(U)HP] – low temperature (LT) complexes in the western part of the Tianshan mountain range. It is mainly composed of continental material and can be divided into a ultra-high, high (HP) and medium pressure (MP) unit. The UHP unit is located in the core of the complex and consists of quartzite, garnet-quartz-phengite schist and garnet-chloritoid-talc schist. UHP conditions were inferred from coesite inclusions in garnet from garnet-chloritoid-talc schist (Tagiri et al. 2010). The UHP unit is surrounded by the HP unit, which consists mainly of garnet-phengite±chloritoid schist. The outermost MP unit comprises greenschist facies phyllite and marble.

For HP and UHP unit samples, a maximum temperature of 510-530 °C ± 30 °C was determined using graphite thermometry. Thermodynamic modelling based on garnet and phengite composition yields a prograde P-T path leading from ~15 kbar and ~450 °C to peak conditions of ~18.5 kbar and ~510 °C for a HP sample located close to the MP unit. The HP sample collected at the boundary to the UHP unit indicates P-T conditions of ~19 kbar at ~470 °C for garnet core and ~23 kbar at ~510 °C for peak metamorphism. Electron probe microanalyzer monazite dating in the HP sample near the MP unit yields 488 ± 5.76 Ma (n = 34; MSWD = 0.48) and is interpreted as recording retrograde metamorphism. A garnet-chloritoid-talc schist sample from the UHP unit indicates P-T conditions of ~23.5 kbar and ~520 °C for garnet core and peak conditions of ~29 kbar and ~580 °C.

Our data reveal a continuous increase in P-T conditions towards the core of the UHP complex. This suggests that at least the UHP and HP unit could represent a continuous continental section that was subducted and also exhumed “en masse” as a single block.

Tagiri M, Takiguchi S, Ishida C, Noguchi T, Kimura M, Bakirov A, Sakiev K, Takahashi M, Takasu A, Bakirov A, Togonbaeva A, Suzuki A (2010): Intrusion of UHP metamorphic rocks into the upper crust of Kyrgyzian Tien-Shan: P-T path and metamorphic age of the Makbal Complex. - J Mineral Petrol Sci, 105, 233-250

Annealing of metamict minerals – spectroscopic study

C. Chanmuang N.[1], M. Zeug[1,2], A. Erlacher[1], K.A.G. Sameera[3,4], L. Nasdala[1]

[1]Institut für Mineralogie und Kristallographie, Universität Wien, 1090 Vienna, Austria
[2] Landesamt für Geologie und Bergwesen Sachsen-Anhalt,
An der Fliederwegkaserne 13, 06130 Halle (Saale), Germany
[3]Postgraduate Institute of Science, University of Peradeniya, P.0. Box 25, Peradeniya 20400, Sri Lanka
[4]Geological Survey and Mines Bureau, 569 B120, Sri Jayawardenepura Kotte 10100, Sri Lanka
e-mail: lutz.nasdala@univie.ac.at

In the country of Sri Lanka, efforts were recently undertaken to survey the occurrence of radioactive phases (Kuruppu et al. 2020; Sameera et al. 2020), among others as potential Th sources. However, phase identification is hampered in many cases because corpuscular self-irradiation over geologic periods of time, caused by the radioactive decay of Th and U and their instable daughter products, may cause these phases to undergo crystalline-to-aperiodic transition. The final, glassy state is referred to as *metamict* (Brøgger 1893).

Metamict minerals are difficult to identify, as structural analysis techniques cannot yield specific information. For instance, X-ray powder diffraction patterns of metamict aeschynite–(Y), euxenite–(Y), fergusonite–(Y), polycrase–(Y), pyrochlore, and samarskite–(Y) are widely similar (Erlacher 2021; and references therein). Similarly, Raman spectra of metamict minerals are extremely broadened and hence cannot be reliably distinguished from each other. The initial, crystalline mineral phase may in some cases be identified using annealing experiments. This, however, is only possible if upon dry annealing, the phase under discussion undergoes structural reconstitution but does not decompose. An example for the latter are allanite-group minerals: Already at temperatures as low as ca. 300 °C, potential dehydrogenation and Fe^{2+} oxidation need to be considered (Sobek et al. 2023; and references therein).

The heating-induced recovery of radiation-damaged minerals may be vastly different, depending on the degree of damage. If a specimen consists of aperiodic and remnant crystalline domains, moderate-T growth of the latter may contribute substantially to the reconstitution. In contrast, the recovery of metamict (that is, fully radiation-damaged) phases requires random nucleation in the glassy bulk and, therefore, typically requires more elevated T.

We present herein the identification of two metamict mineral species whose occurrence on the island of Sri Lanka was hitherto unconfirmed, gadolinite–(Y) ($Y_2Fe^{2+}Be_2Si_2O_{10}$) and fergusonite–(Y) ($YNbO_4$). Stepwise annealings of multiple chips of samples was undertaken to study the recovery processes. Metamict gadolinite–(Y) recovers its initially monoclinic structure at above ca. 800 °C. Our Raman spectrum (Fig. 1), obtained after oxidising heating at 1150 °C, matches well with spectra of natural non-metamict (Allaz et al., 2020) and heated gadolinite–(Y) (Gorelova et al. 2021). Annealing of fergusonite–(Y) involves an $\alpha \rightarrow \beta$ transition: At ca. 550–600 °C, tetragonal fergusonite–(Y) forms and at ca. 750 °C and above, monoclinic clinofergusonite–(Y) is present. The Raman spectrum in Fig. 1 was obtained after oxidising annealing at 1000 °C (Erlacher et al. 2021); it matches well the reference spectrum of Ruschel et al. (2010). We can of course not retrace whether fergusonite–(Y) of clinofergusonite–(Y) were initially present. Independent from that, further Raman analysis of annealed heavy minerals from "*katta*" (local name for the dark and radioactive fraction of heavy mineral concentrates) may help to widen our knowledge of metamict phases occurring in Sri Lanka. Photoluminescence spectroscopy might have similar potential; however, it is currently less suitable, because of the lack of a database of reference spectra.

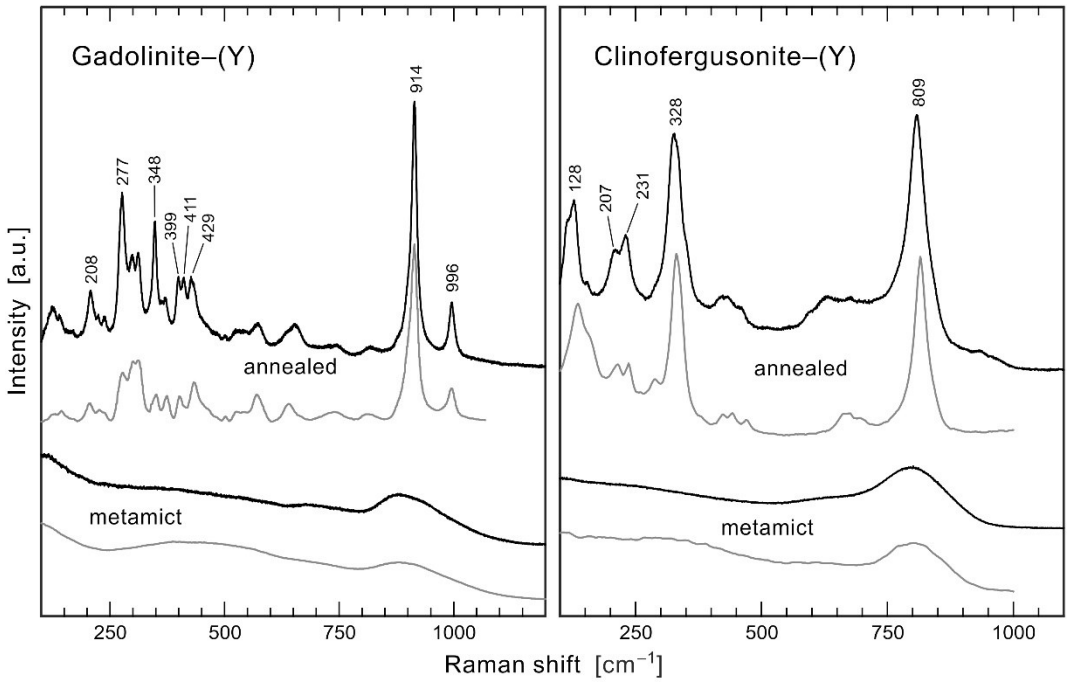

Figure 1. Raman spectra of metamict gadolinite–(Y) and metamict fegrusonite–(Y) and their annealed analogues (black), in comparison with reference spectra (grey). Reference spectrum of metamict gadolinite–(Y) extracted from Tomašić et al. (2020); reference spectrum of annealed gadolinite–(Y) extracted from Gorelova et al. (2021); reference spectra of metamict and annealed clinofergusonite–(Y) extracted from Ruschel et al. (2010).

Allaz JM, Smyth JR, Henry RE, Stern CR (2020): Beryllium-silicon disorder and rare earth crystal chemistry in gadolinite from the White Cloud pegmatite, Colorado, USA. - Canad Miner 58, 829-845

Brøgger WCA (1893): Salmonsens Store Illustrerede Konversationsleksikon 1. - Brødrene Salmonsen, Kopenhagen, 742

Erlacher A, Zeug M, Škoda R, Sameera KAG, Nasdala L (2021): Metamict fergusonite from Kolonna and Masimbula, Sri Lanka. - J Geol Soc Sri Lanka 22, 1-14

Gorelova LA, Panikorovskii TL, Pautov LA, Vereshchagin OS, Krzhizhanovskaya MG, Spiridonova DV (2021): Temperature-versus compositional-induced structural deformations of gadolinite group minerals with various Be/B ratio. - J Solid State Chem 299, 122187

Kuruppu KADDN, Hewathilake HPTS, Illangasinghe IKMSCK, Ranasinghe RANC, Jayasinghe N, Dharmaratne TS (2020): Radioactivity survey on Godakawela gem field in Sri Lanka; to identify the origin of the unknown radioactive mineral. - J Geol Soc Sri Lanka 21, 57-65

Ruschel K, Nasdala L, Rhede D, Wirth R, Lengauer CL, Libowitzky E (2010): Chemical alteration patterns in metamict fergusonite. - Eur J Mineral 22, 425-433

Sameera KAG, Wickramasinghe WAGK, Harankahawa SB, Welikanna CR, de Silva KTUS (2020): Radiometric surveying for Th and U mineralization in southwestern, Sri Lanka: radiological, mineralogical and geochemical characteristics of the radioactive anomalies. - J Geol Soc Sri Lanka 21, 57-80

Sobek K, Losos Z, Škoda R, Hola M, Nasdala L (2023): Crystal chemistry of ferriallanite-(Ce) from Nya Bastnäs, Sweden: Chemical and spectroscopic study. - Mineral Petrol 117, 345-357

Tomašić N, Škoda R, Bermanec V, Šoufek M (2020): Crystal chemistry and microfeatures of gadolinite imprinted by pegmatite formation and alteration evolution. - Amer Mineral 105, 1647-1655

Speciation of La^{3+} in Cl-bearing hydrothermal fluids: Development of a new polarizable force field

R. Chattopadhyay[1], S. Jahn[1]

[1]*Institute of Geology and Mineralogy, University of Cologne, Zülpicher Straße 49b, Cologne, Germany*
e-mail: rchattop@uni-koeln.de

The Rare Earth Elements (REEs) are an important group of elements both geologically as well as economically. REEs find important applications in the fields of green energy, electric vehicles and electronics. They are also important tracers for geological processes under hydrothermal /high grade metamorphic conditions. The ability of fluids to mobilize the REEs depend on the chemical composition and the presence of suitable ligands such as chloride and fluoride. *Ab initio* molecular dynamics simulations (AIMD) have been used to predict stability constants of various REE complexes and REE speciation under hydrothermal conditions (Stefanski & Jahn 2020; Guan et al. 2022). However, AIMD simulations often suffer from significant finite time and size effects.

The development of classical force fields for ions in aqueous solutions is essential in the field of hydrothermal geochemistry. The reliability and accuracy of classical force fields not only depends on its representation of effects of ionic size but also on polarization of solvent and solute charge densities. The latter many-body term becomes important particularly when dealing with highly charged ions (Piquemal et al. 2009) in concentrated solutions (Tribello et al. 2009) and in interfacial environments (Jungwirth & Tobias 2006). Many different polarizable force fields exist, each having a different representation of polarizability. Here, we choose the point polarizability model of Dang & Chang (1997) for H_2O, which was specifically parameterized to describe gas-liquid interface (Dang & Chang 1997).

We develop a new polarizable forcefield for La^{3+} in Cl-bearing hydrothermal fluids. The forcefield has been fitted to snapshots of AIMD simulations of La^{3+} and Cl^- ions in water at hydrothermal conditions (773 K, 5 kbar). We used Maximally Localized Wannier Functions (MLWFs) along with force and dipole matching techniques to fit the parameters of the potential (Tazi et al. 2012). We used the technique of Madden and co-workers to calculate the ionic polarizabilities of the charged ions (Salanne et al. 2012). Experimental and AIMD data (wherever available) were used to test the validity of this new potential by comparing structural and thermodynamic properties. We also investigate the speciation of La^{3+} in highly concentrated hydrothermal brines for which no experimental/AIMD data exists.

Stefanski J, Jahn S (2020): Yttrium speciation in subduction-zone fluids from *ab initio* molecular dynamics simulations. - Solid Earth 11, 767–789

Guan Q, Mei Y, Etschmann B, Louvel M, Testemale D, Spezia R, Brugger J (2022): Speciation and thermodynamic properties of La(III)-Cl complexes in hydrothermal fluids: A combined molecular dynamics and in situ X-ray absorption spectroscopy study. - Geochim Cosmochim Acta 330, 27–46

Piquemal J-P, Perera L, Cisneros GA, Ren P, Pedersen LG, Darden TA (2006): Towards accurate solvation dynamics of divalent cations in water using the polarizable amoeba force field: From energetics to structure. - J Chem Phys 125, 054511

Tribello GA, Bruneval F, Liew C, Parrinello M (2009): A molecular dynamics study of the early stages of calcium carbonate growth. - J Phys Chem B113(34), 11680–11687, PMID: 19650654

Jungwirth, P. and Tobias, D. J. (2006). Specific ion effects at the air/water interface. - Chem Rev 106(4), 1259–1281. PMID: 16608180

Dang LX, Chang T-M (1997): Molecular dynamics study of water clusters, liquid, and liquid–vapor interface of water with many-body potentials. - J Chem Phys 106(19), 8149–8159

Tazi S, Molina JJ, Rotenberg B, Turq P, Vuilleumier R, Salanne M (2012): A transferable *ab initio* based force field for aqueous ions. – J Chem Phys 136(11), 114507

Salanne M, Rotenberg B, Jahn S, Vuilleumier R, Simon C, Madden PA (2012): Including many-body effects in models for ionic liquids. - Theoret Chem Accounts 131, 1143

Al, Si interdiffusion under lower mantle conditions

L. Czekay[1], N. Miyajima[1], C. McCammon[1], D. Frost[1]

[1] *Bayerisches Geoinstitut, University of Bayreuth*
e-mail: laura.czekay@uni-bayreuth.de

The diffusion of atoms in minerals at high temperatures and pressures influences Earth's lower mantle dynamic processes. This study aims to better understand the physical behaviour of Earth's most abundant mineral with implications for lower mantle viscosity. Previous studies that measured Si-self diffusion coefficients in bridgmanite (Brg) showed a value at 25 ± 1 GPa and 1800 °C of $Log_{10}(D_{Si})$ = -18 ± 0.5 (based on units of m^2/s; relevant information can be found by Yamazaki et al. 2000; Dobson et al. 2008; Xu et al. 2011). Our study revealed a significantly slower diffusion coefficient that may challenge previous calculations of lower mantle viscosity. We investigated Al, Si interdiffusion in Brg experimentally at 24 GPa and 1750 to 2000 °C using a multi-anvil apparatus using diffusion couples composed of bridgmanites that were pre-synthesised from 0-5 mol.% Al_2O_3-bearing $MgSiO_3$ enstatite. The Al diffusion profiles were analysed across the diffusion interface in the recovered samples using a scanning transmission electron microscope equipped with an energy-dispersive X-ray spectrometer. The obtained diffusion coefficient for interdiffusion (volume diffusion) at 24 GPa and 1800 °C was $Log_{10}(D_{Al,Si})$ = -20.1 ± 0.7. The resulting data can be used to estimate deformational strain rates of Brg in the lower mantle from viscosity based on different creep mechanisms.

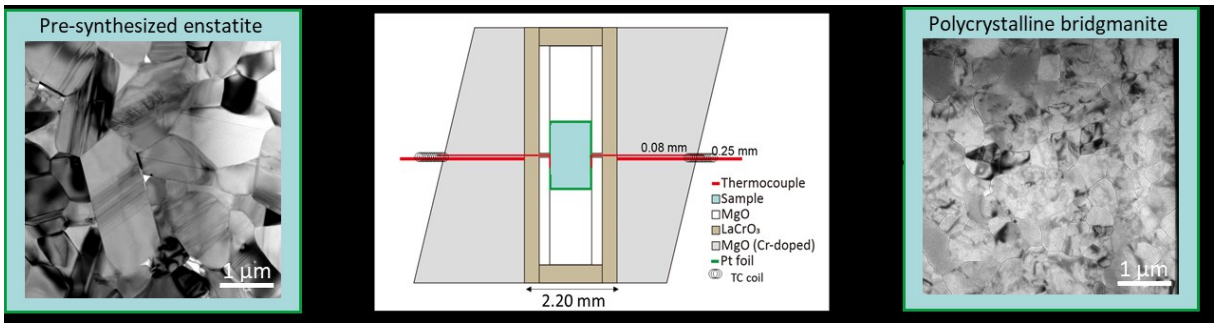

Fig. 1: Experimental setup of the 7/3 assembly and schematic drawing of the experimental path from the pre-synthesized enstatite to the polycrystalline bridgmanite for the diffusion experiments.

Dobson DP, Dohmen R, Wiedenbeck M (2008): Self-diffusion of oxygen and silicon in $MgSiO_3$ perovskite. - Earth Planet Sci Lett 270, 125-129

Xu J, Yamazaki D, Katsura T, Wu X, Remmert P, Yurimoto H, Chakraborty S (2011): Silicon and magnesium diffusion in a single crystal of $MgSiO_3$ perovskite. - J Geophys Res: Solid Earth 116(B12)

Yamazaki D, Kato T, Yurimoto H, Ohtani E, Toriumi M (2000): Silicon self-diffusion in $MgSiO_3$ perovskite at 25 GPa. - Phys Earth Planet Inter [Internet] 119, 299–309

The lower Permian basalt - rhyolite - carbonatite magmatic activity in the Kvetnica volcanic area, Western Carpathians

R. Demko

Turzovka, Stred 373, 023 54, Slovakia
rastislav.demko@geology.sk

The Western Carpathians crystalline basement is built by granite–metamorphic rock complexes, covered by sedimentary sequences tectonically arranged into Alpine nappe structures. The Hronic Unit is one of the most spatially extended tectonic upper Alpine nappe structure in the Western Carpathians. The lithology of the Hronic Unit represents a record of volcanic and sedimentary rocks from the Upper Carboniferous to Upper Triassic and Jurassic period. The volcanism operated in parental Hronic area forming two main volcanic phases in the Lower and the Upper Permian with massive production of basalts, basaltic andesites, basaltic trachyandesites and their pyroclastics.

The presented results focus on news from the Kvetnica quarry near Poprad city in the Low Tatras, which belongs to the well-known locality of Maluzina Fm. During field research, I have identified intrusions of younger basalt accompanied by rhyolite, penetrating a set of older horizontally layered older basaltic lavas.

Based on the TAS classification, it is an intrusion of alkaline basaltic trachyandesite BTA and subalkaline rhyolite with a high SiO_2 content (76.5 wt.%). BTA has a porphyric amygdaloid texture dominated by zonal plagioclases and quartz-calcite amygdales. The rhyolite rock is black, aphanitic, with an association of small phenocrysts: quartz, albite, plagioclase, biotite, garnet, Fe-Ti oxides with accessory zircon and monazite. Garnet contains inclusions of orthopyroxene and ilmenite. The rhyolite rock itself is combined by inserted / mingled rhyolite and carbonatite magma, the relationship of which is determined by their mutual immiscibility, see Figure 1.

This is the first detection of rhyolite rock in the Hronicum unit, directly intruding a thick cover of basaltic effusions. The special composition of the rhyolite rock, made it possible to determine magmatic age of rhyolite as the Lower Permian (Kungurian) 278±6.2 Ma., using U-Th-Pb EPMA of monazites. The identified age is the first analytical geochronological data that assigns age of the Kvetnica paleovolcanic activity to the Lower Permian!

Thermobarometric study of Qtz+Pl+Bt+Grt phenocryst association of rhyolite provides PT data 800-750 °C at 135-200 MPa, indicating the depth of magma chamber emplacement, where BTA magma had differentiated to form rhyolite.

The K_2O (1.5 wt.%) and Fe_2O_3/FeO (0.51) content of the rhyolite rock is very similar to the host alkaline BT-andesite with K_2O (1.74 wt.%) and Fe_2O_3/FeO (0.63). Geochemical analyzes show significant REE fractionate during differentiation of basaltic parental magma, whose La/Yb_{C1} (4.64) and Eu/Eu*(0.82) fractionate toward rhyolitic magma with La/Yb_{C1} (18.43) and Eu/Eu*(0.58). REE modelling of basaltic rocks from the Hronic Unit shows that the first volcanic products (lower Permian) are result of lower melting degree 1.1% melt grt-peridotite & 14% melt of sp-peridotite mixed in mass (1/1.7) with continuous increase to melting of 1.9% melt Grt-peridotite & 13% melt of sp-peridotite mixed in mass 1/2.8 (fractional cumulated melting, McKenzie & O´Nions 1991). BTA composition from Kvetnica, as a parental analogue of rhyolite magma, shows a similarity with other Lower Permian basalts generated by lower degree of melting, which agrees with obtained magmatic age.

Petrographic observations and EPMA study showed existence of interstitial or droplet calcite, which represent a carbonatite melt in the host silicate magma. Their mutual spatial relationships indicate interaction of two immiscible liquids. For the first time in the evolution of BTA-rhyolite differentiation, a carbonatite melt is observed in a sample of BTandesite in form of spirally shaped carbonate globules, inclusions in plagioclase, and thin bounded zones of albite enclosed in intermediate plagioclases (56-54 anorthite mol.%). Thermodynamic MELTS modelling (Gualda et al., 2012; Ghiorso & Gualda 2015), focused on BTA fractionation and composition of feldspars, suggest highly oxidizing conditions in magma chamber. Observed composition of feldspars phenocrysts were reached in 1060-1050 °C and △QFM = +2 or 1040-1030 °C and △QFM = +3. The evolution of observed carbonatite melts is connected with degassing of released CO_2, which interacted with host silicate melt to form carbonatite.

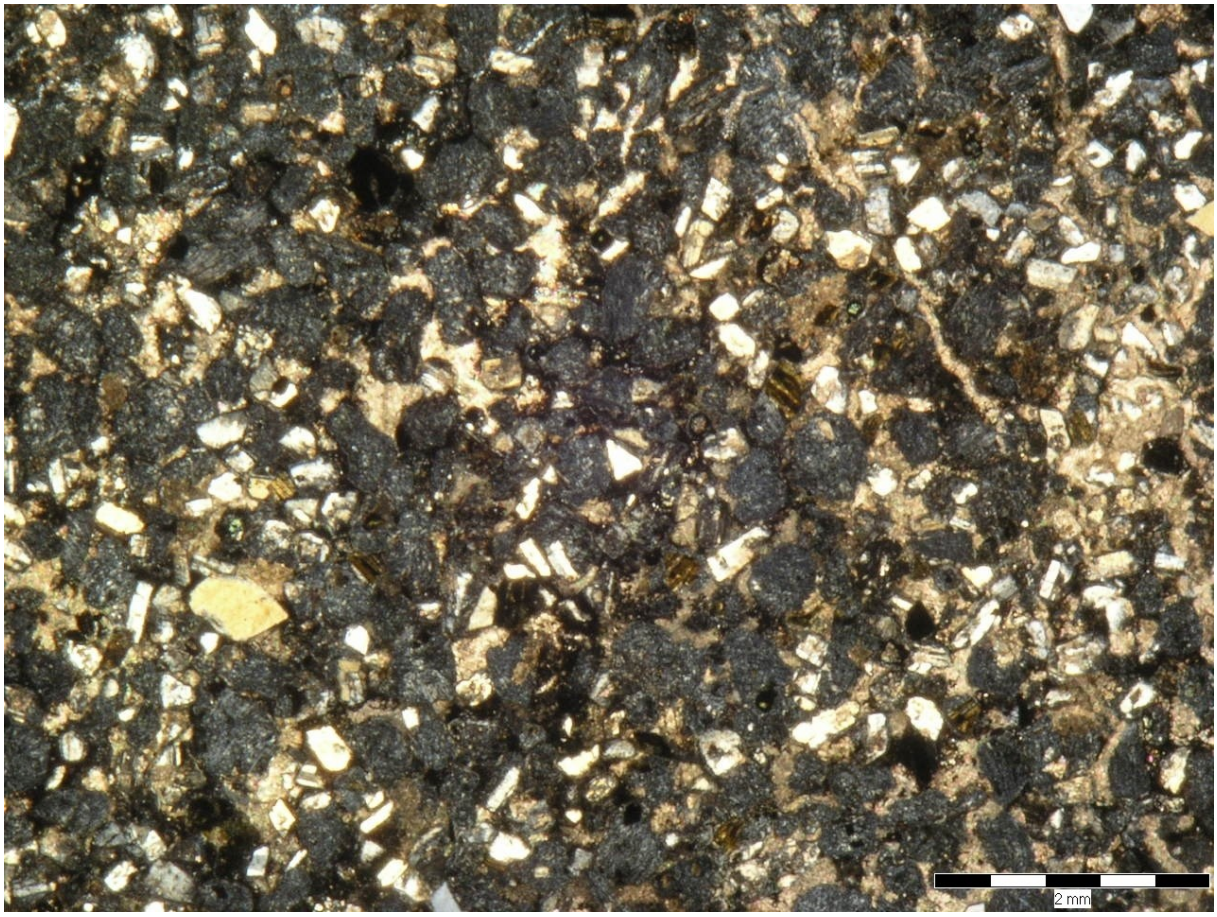

Figure 1: Fragments of rhyolite melt "frozen" between carbonatite immiscible liquid and phenocrysts of quartz, plagioclases, biotite, Fe-Ti oxides and garnet. Photography in polarized light.

Ghiorso MS. Gualda GAR (2015): An H_2O - CO_2 mixed fluid saturation model compatible with rhyolite-MELTS. - Contr Miner Petrol, doi:10.1007/s00410-015-1141-8

Gualda GAR, Ghiorso MS, Lemons RV, Carley TL (2012): RhyoliteMELTS: A modified calibration of MELTS optimized for silica-rich, fluid-bearing magmatic systems. - J Petrol 53, 875-890

McKenzie D, O'Nions RK (1991): Partial Melt Distributions from Inversion of Rare Earth Element Concentrations. - J Petrol 32, 1021–1091

Fingerprinting graphite: The development of a three-step approach to differentiate between natural graphite deposits

V. Dietrich[1], R. Arató[1], F. Melcher[1]

[1]Montanuniversität Leoben, Department of Applied Geosciences and Geophysics, Peter-Tunner-Straße 5, 8700 Leoben
e-mail:valentina.dietrich@unileoben.ac.at

Graphite is considered as a critical raw material due to its significant importance in various industrial applications, such as the steel and refractories industry, but energy storage being the most important industrial sector. Graphite is a vital component in lithium-ion batteries, which are widely used in electric vehicles and other electronic devices. The demand for lithium-ion batteries has been rapidly increasing, driving the demand for graphite and therefore also the interest in the origin of this raw material. Embedded in a framework project aimed at traceability of battery raw materials, this project aims to reinforce transparency, reliability and sustainability of complex critical raw material supply chains.

This study shows an innovative multi-parameter analytical approach in order to differentiate between graphite samples from different locations. Stable carbon isotopes offer a parameter to differentiate between different sources of carbon. The initial carbon in flake and amorphous graphite is of organic origin, whereas carbon in hydrothermal graphite deposits is inorganic and mostly originates from CO_2 or CH_4 rich fluids (Luque 2013). This distinction can be constrained via carbon isotopy and serves as the first step in distinguishing natural graphite deposits. The Raman spectrum of graphite is characteristic for its microstructural state and serves as a basis for estimating peak metamorphic temperatures during graphite formation (Lünsdorf et al. 2016; Rantitsch et al. 2016). As such, it provides a further means to distinguish different deposits. The third part for proving the origin of graphite is provided by trace element analysis. Given that the formation temperature of many flake graphite deposits is similar within error, the geographical origin of individual deposits can be traced only by means of characteristic trace elements. Research is still underway to find a suitable analytical method for this purpose (e.g., ICP-MS, LIBS, XRF). Solution-based analysis (e.g. via ICP-MS), however, proved to be unsuitable, as the complete dissolution of graphite is notoriously difficult, due to the carbon layers being very challenging or even impossible to break up. The digestions and their analytical results are therefore not consistently reproducible and also too costly to withstand routine application as a fingerprinting technology for industry purposes. LA-ICP-MS proved to be much more suitable also due to simpler sample preparation. Although the ablation of very fine-grained material in compressed form also poses challenges, pathfinder elements that allow a geographical differentiation of origins, could be found by LA-ICP-MS. ETV-ICP-OES serves as another potential methodology for discrimination of graphite deposits, especially as an approved methodology for analysis of trace elements in carbon-rich materials (Vogt et al. 2015). However, this methodology for graphite must first be evaluated to prove its suitability. Analytical proof of origin (APO) methods in general are regarded as the least corruptible methods, as they directly relate to the chemical composition of the raw material (Melcher et al. 2021). Other methods such as conventional documents, tracers, QR codes and barcodes can be outmanoeuvred in one way or another.

Lünsdorf NK, Lünsdorf JO (2016): Evaluating Raman spectra of carbonaceous matter by automated, iterative curve-fitting. - Int Jour Coal Geol 160-161, 51-62

Luque FJ, Huizenga JM, Crespo-Feo E, Wada H, Ortega L, Barrenechea JF (2014): Vein graphite deposits: geological settings, origin, and economic significance. - Miner Deposita 49, 261-277

Melcher, F., Dietrich, V., Gäbler, H.-E. (2021): Analytical Proof of Origin for Raw Materials. - Minerals 11, 461

Rantitsch G, Lämmerer W, Fisslthaler E, Mitsche S, Kaltenböck H (2016): On the discrimination of semi-graphite and graphite by Raman spectroscopy. - Int Jour Coal Geol 159, 48-56

Vogt T, Bauer D, Neuroth M, Otto M (2015): Quantitative multi-element analysis of Argonne Premium Coal samples by ETV-ICP OES – A highly efficient direct analytical technique for inorganics in coal. – Fuel 152, 96-102

Mineralogical control of synergetic thallium and antimony weathering

T. Đorđević[1,2], M. Stöger-Pollach[1]

[1]*University Service Centre for TEM, Technische Universität Wien, Wiedner Hauptstraße 8-10, Wien, Austria*
[2]*Institut für Mineralogie und Kristallographie, Universität Wien, Josef-Holaubek-Platz 2, Wien, Austria*
e-mail: tamara.dordevic@tuwien.ac.at

As metals and metalloids have a strong impact on the environment, methods for their detection and speciation have received a particular attention in the last few years. Thallium (Tl), antimony (Sb) and arsenic (As) are important examples of such toxic elements. Their speciation is of the particular interest owing to their toxicity, bioavailability and reactivity. One of the world most famous deposit hosting all these three elements is Sb-As-Tl-Au Allchar deposit in North Macedonia, which mining waste dumps and technosoils served us as an ideal natural laboratory for the investigations of the oxidative processes on the primary sulfide and sulfosalt minerals. Of the particular interest were the weathering processes in the Sb-rich (Sb: 1000–16500 ppm) central part of the deposit, where Tl-concentrations have been measured in the range between 120-840 ppm (Đorđević et al. 2021).

In the scope of our previous study (Đorđević et al. 2021) we have identified primary and secondary mineralogy of the technosoils in the central part of Allchar deposit. As the main primary Tl-sources we have identified sulfosalts fangite, lorándite and pierrotite. Tl dissolved during weathering under circumneutral conditions is reprecipitated as avicennite and as tiny, fibrous Tl-bearing Mn oxides (up to 8.5 at.% of Tl). Furthermore, tiny spherulitic aggregates (up to 3 μm) of a Tl-Sb-oxide (unknown mineral species) have been found intergrown with quartz, muscovite and minor dolomite. Due to their small aggregate size, we have not been able to closer identify these oxides. Therefore, we have decided to take a closer look at these phases using transmission electron microscopy (TEM). The TEM-lamellae were prepared by means of focused ion beam (FIB) and were investigated under cryogenic condition (–184 °C) using high-resolution scanning transmission microscopy (HR-STEM) coupled with electron dispersive spectroscopy (EDS) and electron backscatter diffraction (EBSD). Just after a short electron exposure, Tl_2O_3 crystals in the size up to 100 nm formed on the surfaces of the Tl-Sb-oxides. EBSD on Tl-Sb-oxide particles confirmed that the Tl-Sb-oxide is crystalline and the EDS-line and area scans confirmed Tl:Sb ratio of 2.5, meaning that Tl enters the crystal structure of the new Tl-Sb oxides and is not hosted as the nanophase.

Both nano- and microcrystalline Tl-minerals are important products of oxidative weathering of Tl-bearing metal-sulphides. Our future study focused on the formation and dissolution of these phases will provide a much deeper insight into the mechanisms of formation of specific mineral association and will help to interpret common features in the alteration paths in general.

This work was supported by the Austrian Science Fund (FWF) [grant number P 36828-N to T. Đorđević]

Đorđević T, Kolitsch U, Drahota P, Majzlan J, Peřestá M, Serafimovski T, Tasev G, Boev I, Boev B (2021): Tl sequestration in the middle part of the Allchar Sb–As–Tl–Au deposit, North Macedonia. - Goldschmidt Virtual Conference, Abstracts, Lyon, France, 4–9 July 2021

New applications for digitised historical collections as teaching materials for special mineralogy and petrography

A. Duriagina[1], C. Kehrer[2], G. Heide[1]

[1]TU Bergakademie Freiberg, Institute for Mineralogy, Brennhausgasse 14, 09599 Freiberg
[2]TU Bergakademie Freiberg, Geoscientific Collections, Brennhausgasse 14, 09599 Freiberg
e-mail: Asiia.Duryagina@mineral.tu-freiberg.de

The Geoscientific Collections of the TU Bergakademie Freiberg are among the most extensive and diverse of their kind. Since the founding of the Bergakademie, they have been created in the context of teaching and further education of students as well as for research purposes and have been continuously expanded ever since. Today, the collections still form an important cornerstone within the education of students and specialist staff. In the emerging age of digital media and virtual realities, as well as against the background of an ever-increasing pool of historical collection material, the aim is to present, archive and use these objects appropriately.

Since the teaching collections and their objects are only accessible to a limited extent within the framework of courses, it is necessary, among other things, to digitise them so that they can be made available in interactive teaching formats. Especially in the field of mineralogy, crystallography and petrology, it is particularly important for students to deal with the greatest possible variety of different objects within the teaching collections. This can be optimally realised through the additional digitised content and thus complement conventional teaching. The digital and visualised collection recording is thus indispensable for a location-independent and cross-thematic use in teaching. Through digital recording, background knowledge on the exhibits is prepared in multimedia form, thus making a greater variety of knowledge accessible to the student in addition to classroom studies.

Digitisation also allows us to use other very interesting objects as teaching aids. For example, historical collection of decorative stones from the Altai Mountains (stone-cutting workshop in Kolywan) is usually not suitable for student work due to its rarity and uniqueness, but once it is digitised, it offers enormous potential for study.

The collection, compiled by Bernhard von Cotta (1808-1879) during his journey to Altai (Cotta et al. 1871), comprises 70 hand specimens and 40 thin sections and is housed in the Geosciences Collections of the TU Bergakademie Freiberg. Each rock slab is 8 x 4.5 cm, ground and polished on one side as well as on the edges, the other main side has a fresh fracture. They are mainly granites, felsic igneous rocks with porphyritic structure, marbles and various schists, as evidenced by a post-determination (Weber, 2019). In 2021, the samples were also digitally recorded using multi- and hyperspectral photography to provide reference data for the non-destructive analysis of museum objects. Furthermore, the historical thin sections were microscopically scanned with linear and cross polarised light and matched with the historical images.

Acknowledgements: We would like to thank the foundation "Innovation in der Hochschullehre" for the financial support and Mr. G. Sacher from "Fokus GmbH" for the discussions and talks.

Cotta B von, Teplouchow TA, Geinitz HB, Stelzner AW (1871): Der Altai: Sein geologischer Bau und seine Erzlagerstätten. - Leipzig: Weber JJ

Weber A (2021): Bernhard von Cottas historische Sammlung polierter Gesteinstafeln aus der russischen kaiserlichen Steinschleiferei zu Kolyvan' im Altai. - Perspektive des Sammlungswissens, Humboldt-Universität zu Berlin 48-56, doi.org/10.18452/23914

Fused beads for the analysis of Li bearing samples by LIBS and XRF

D. Ebert[1], R. Möckel[1], A.D. Renno[1], A. Schneider[1,2], T. Dittrich[3]

[1]Helmholtz-Zentrum Dresden-Rossendorf; Helmholtz-Institute Freiberg for Resource Technology, Chemnitzer Straße 40, 09599 Freiberg
[2]TU Bergakademie Freiberg, Institut für Organische Chemie, Leipziger Straße 29, 09599 Freiberg
[3]Deutsche Lithium GmbH, Am Junger-Löwe-Schacht 10, 09599 Freiberg
e-mail: d.ebert@hzdr.de

In recent decades, it has become apparent that due to the increasing complexity of deposits, the complexity of ore samples is also increasing. At the same time, the need for detailed geological and mineralogical information also increased. Therefore, it is important to combine methods in order to obtain more comprehensive conclusions.

We present a method of combining WDXRF (wavelength dispersive X-ray fluorescence) analyses with a wide spectrum of elements and pLIBS (portable laser induced breakdown spectroscopy, see Fig. 1) with a likewise spectrum and the additional possibility to detect light elements such as Li. Nevertheless, the representativeness of LIBS analyses is significantly smaller compared to XRF. To overcome this and effectively combine both methods, we designed and produced fused beads using $Na_2B_4O_7$ as flux. Unfortunately, such beads are transparent to the laser which makes LIBS analysis almost impossible, therefore, we tested two different approaches: 1) dying the bead by adding CuO to the flux and 2) roughen the beads surface. We used a mixture of $Na_2B_4O_7$ (+ CuO) + KI as matrix. Potassium iodide (KI) was added as a releasing agent. We used Greisen rocks from the Altenberg-Zinnwald district with known composition – including Li – and $LiBO_2$ in different concentration ratios to adjust the Li content.

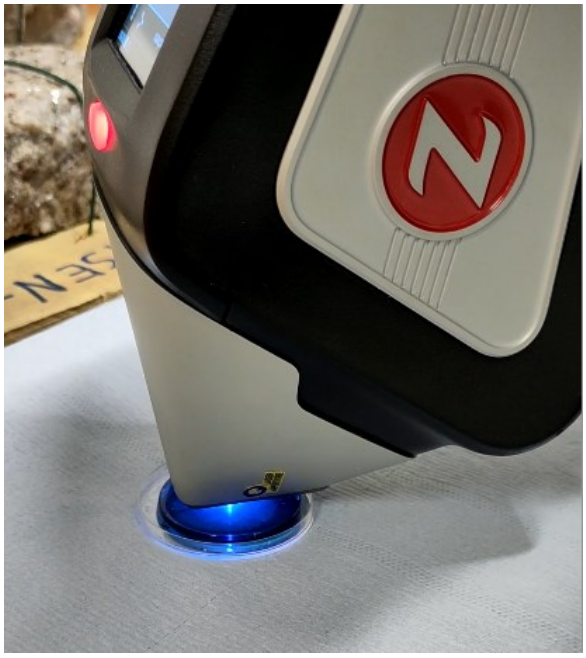

Fig. 1: pLIBS measurement on a fused bead containing Cu as dying agent.

To produce crack-free beads, we had to adapt the melting process in the fully automatic melting furnace TheOx (CLAISSE). For the analytical work, we use a portable LIBS instrument manufactured by SciAps (Z-300, laser wavelength 1064 nm) and a PANalytical Axiosmax minerals XRF spectrometer.

The fused beads will now serve as calibration samples for both XRF and LIBS measurements (see Fig. 2). Samples with unknown composition will be analysed by XRF first. It turned out that roughening the beads has no significant influence on the XRF-spectra as revealed in before and after scan measurements. In a second step the LIBS analysis is performed in particular for light element determination such as Li. Furthermore, adding a dying component such as Cu might be suitable as a robust internal standard for both LIBS and XRF.

The obvious disadvantage of the method is that neither Cu, K nor Na can be included in the quantitative analysis. De-pending on the analytical problem, they would have to be determined in a preceding step (e.g. via a conventional Li-borate melt and XRF).

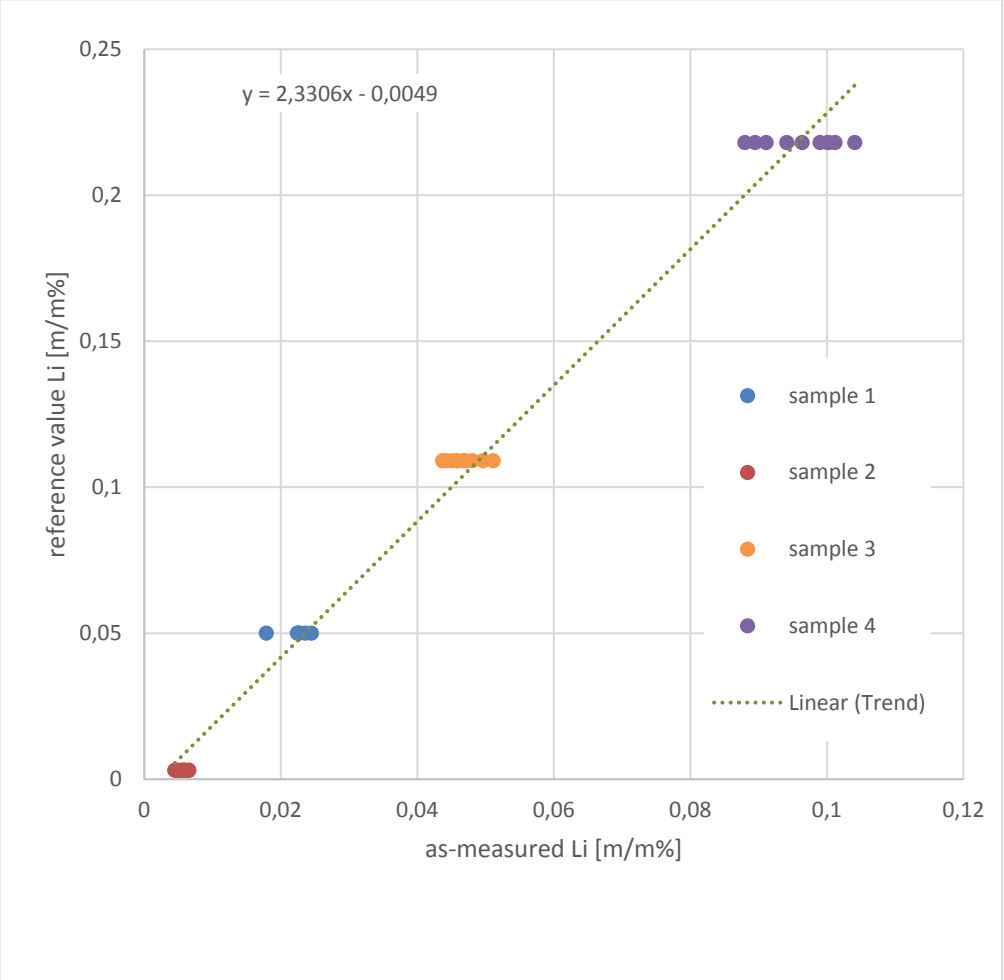

Fig. 2: Calibration factor derived from the initial fused beads, showing robust data on each sample.

Structural diversity in new, synthetic zemannite-type phases

F. Eder[1], A. Marsollier[2], M.Weil[1]

[1]TU Wien, Institute for Chemical Technologies and Analytics, Structural Chemistry
[2]IUT Bordeaux-Gradignan
e-mail: felix.eder@tuwien.ac.at

The mineral zemannite (Matzat 1967; Fig. 1), named in honor of Prof. Josef Zemann (1923−2022), has a composition of $[Zn^{2+}Fe^{3+}(TeO_3)_3]_2[Mg(H_2O)_6]\cdot nH_2O$ ($n \leq 3$), and is the mineral of the MinWien2023 conference. Synthetic zemannite-type phases can be obtained from hydrothermal reactions between transition metal oxides, tellurium dioxide and alkali metal carbonates. In comparison with the usual set-up for a hydrothermal experiment, the drastic reduction of the water content changes the role of water from a typical solvent to a mineralizer. Under these conditions, the formation of numerous new phases with zemannite-type structures was observed (Eder et al. 2023).

The crystal structures of the new zemannite-type phases were determined on basis of single-crystal X-ray diffraction. Like the mineral zemannite itself, the crystal structures of $Fe_2(TeO_3)_3$, $Na_2[Ni_2(TeO_3)_3](H_2O)_{2.5}$, $K_2[Ni_2(TeO_3)_3](H_2O)$, $K_2[Zn_2(TeO_3)_3](H_2O)_2$, $Rb_{1.25}[Co_2(TeO_3)_3](H_2O)_{1.5}$, $Rb_{1.24}[Mn_2(TeO_3)_3](H_2O)_2$, and $Na_{1.79}Mg_{0.11}[Mg_2(TeO_3)_3](H_2O)_{3.86}$ show hexagonal metrics, with $a \approx 9.3$ Å and $c \approx 7.7$ Å. Relative to this unit-cell, different kinds of superstructures are realized for $Na_2[Cu_2(TeO_3)_3](H_2O)_{1.5}$ (threefold), $K_2[Cu_2(TeO_3)_3](H_2O)_2$ (twofold), $K_2[Co_2(TeO_3)_3](H_2O)_{2.5}$ (twofold and incommensurately modulated), $Rb_{1.5}[Mn_2(TeO_3)_3](H_2O)_{1.25}$ (fourfold), and $Cs[Mn_2(TeO_3)_3](H_2O)$ (fourfold).

The formation of these superstructures can be attributed to several influences. Variable water contents (compounds with zemannite-type structures are known for their zeolitic properties (Miletich 1995)), the space requirements of large alkali metal cations like Rb^+ or Cs^+, and Jahn−Teller distortions of the coordination polyhedra of certain framework atoms like Cu^{II} or Mn^{III} play crucial roles in this respect.

Another aspect of zemannite-type crystal structures is the nature and distribution of the contents inside the large hexagonal channels perforating the framework. For most of the investigated phases, alkali metal cations and crystal water molecules are displaced up to 2 Å from the channel center and are disordered around the 6_3 axis (or other symmetry elements containing a threefold rotation axis). In the superstructures of $Rb_{1.5}[Mn_2(TeO_3)_3](H_2O)_{1.25}$ and $Cs[Mn_2(TeO_3)_3](H_2O)$, ordered channel-contents were observed. $Fe_2(TeO_3)$ has empty channels, which causes some Te^{IV} atoms of the framework to "tilt" towards the channel center. In $Na_{1.79}Mg_{0.11}[Mg_2(TeO_3)_3](H_2O)_{3.86}$, both Na^+ and Mg^{2+} cations inhabit the channels together with H_2O molecules, and the superposition of their respective environments can be noticed in the crystal structure refinement.

Figure 1. Zemannite−the mineral of the meeting. Photo: S. Wolfsried

Eder F, Marsollier A, Weil M (2023): Structural studies on synthetic $A_{2-x}[M_2(TeO_3)_3]\cdot nH_2O$ phases (A = Na, K, Rb, Cs; M = Mn, Co, Ni, Cu, Zn) with zemannite-type structures. - Mineral Petrol https://doi.org/10.1007/s00710-023-00814-5

Matzat E (1967): Die Kristallstruktur eines unbenannten zeolithartigen Tellurminerals, $\{(Zn, Fe)_2[TeO_3]_3\}Na_xH_{2-x}\cdot yH_2O$. - Tschermaks Mineral Petrogr Mitt 12, 108–117

Miletich R (1995): The synthetic microporous tellurites $Na_2[Me_2(TeO_3)_3]\cdot 3H_2O$ (Me = Zn, Co): crystal structure, de- and rehydration, and ion exchange properties. - Monatsh Chem 126, 417–430

$CuSeO_4$ and $Cu(SeO_3OH)_2 \cdot 6H_2O$: A tribute to the enlightenment of the stereochemistry of Cu^{2+} ions by Josef Zemann (1923–2022)

H.S. Effenberger[1], G. Giester[1], M. Wildner[1]

[1]*Institut für Mineralogie und Kristallographie, Universität Wien*
herta.silvia.effenberger@univie.ac.at

In the middle of the last century the stereochemistry of divalent copper atoms was mostly unknown. Crystal structure investigations of trippkeite, azurite, linarite, or teineite led Josef Zemann (1923-2022) to understand the coordination figures controlled by the Jahn-Teller-effect. In contrast to the earlier thought CuO_6 octahedra, he described the coordination figures as planar [4], tetragonal pyramidal [4+1], and tetragonal *di*pyramidal [4+2] (Zemann 1961; 1972). The additional ligands have none or only a minor influence on the geometry of the CuO_4 square. In honour to these pioneering investigations, two further compounds with Cu^{2+} ions are presented here: $Cu(SeO_4)$ and $Cu(SeO_3OH)_2 \cdot 6H_2O$. They were synthesized at low-temperature hydrothermal conditions (220 °C) and room temperature, respectively.

Snyman & Pistorius (1964) described two modifications of $CuSeO_4$: one crystallises in the structure type of $ZnSO_4$ (mineral name zincosite, space group *Pnma*), the high-pressure form in the $NiSO_4$-structure type (space group *Cmcm*). The new $Cu(SeO_4)$ modification presented here adopts the $MnAsO_4$-structure type (space group $P2_1/n$), it represents a monoclinic distortion form the *Pnma* modification.

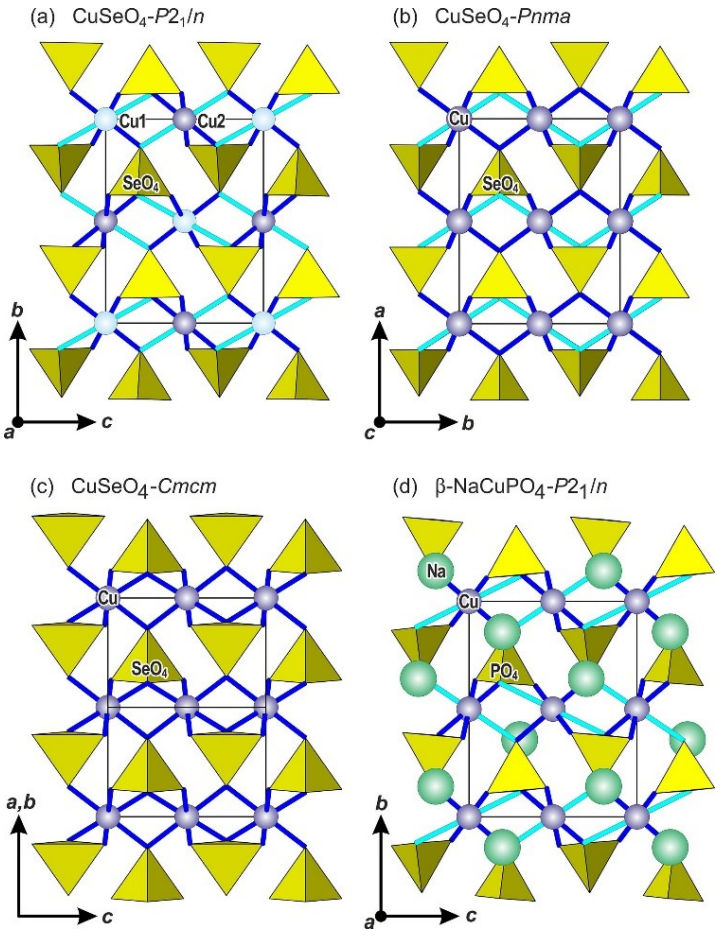

Fig. 1 The crystal structures of
(a) $Cu(SeO_4)$-$P2_1/n$ (structure type $MnAsO_4$),
(b) $Cu(SeO_4)$-*Pnma* (structure type $ZnSO_4$),
(c) $Cu(SeO_4)$-*Cmcm* (structure type $NiSO_4$, and
(d) β-$NaCuPO_4$-$P2_1/n$ (Kawahara et al. 1993).

Mn^{3+} ions exhibit a pronounced [4+2] coordination due to the Jahn-Teller effect. Therefore, the substitution $Cu^{2+} \leftrightarrow Mn^{3+}$ is not surprising. The coupled substitution $Mn^{3+} + As^{5+} \leftrightarrow Cu^{2+} + Se^{6+}$ enables isotypy between $CuSeO_4$-$P2_1/n$ and $MnAsO_4$.

The crystal structure of $Cu(SeO_3OH)_2 \cdot 6H_2O$ crystallizes in a new structure type. It is characterized by three structural units (i.e., $[Cu^{[4+2]}(H_2O_w)_4O_2]$, $[SeO_3(O_hH)]$, and $[H_2O_w7]$). They are connected mainly by hydrogen bonds (Fig. 2). The $Cu^{[4+2]}O_6$ polyhedron forms a quite regular tetragonal *di*pyramid with site symmetry $\bar{1}$. The two pairs of independent Cu—O_w bonds within the CuO_4 square are nearly identical and vary only by 0.0016 Å; O—Cu—O bond angles deviate up to 2° from the ideal value. Hence, the $Cu^{[4+2]}O_6$ *di*pyramid adopts a nearly regular shape, obviously due to the rather soft connection among the structural units. The bond valence sum calculated for the Cu atom is unexpectedly large (2.26 v.u.). It is a general experience that for coordination polyhedra loosely bound to further structural units the cation—anion distances are shortened to compensate for the under-saturation of the anions. Consequently, the bond valence sums are over-estimated. Blocksatz

During the final refinement cycles, anisotropic displacement parameters of the Se, Cu, and O atoms as well as isotropic ones for the H atoms were refined. Only for the atom Ow7 the displacement parameters of the two H ligands were constrained to equal values during the structure refinement. The protonated selenate(VI) group exhibits Se—O bonds of 1.614 to 1.626 Å (to the atoms O1, O2, and O3) whereas the Se—O_h bond is extended to 1.695 Å. This environment is in agreement with the average Se—O_h value in *mono*protonated selenate(VI) groups of 1.71 Å as compiled by Ferraris and Ivaldi (1984).

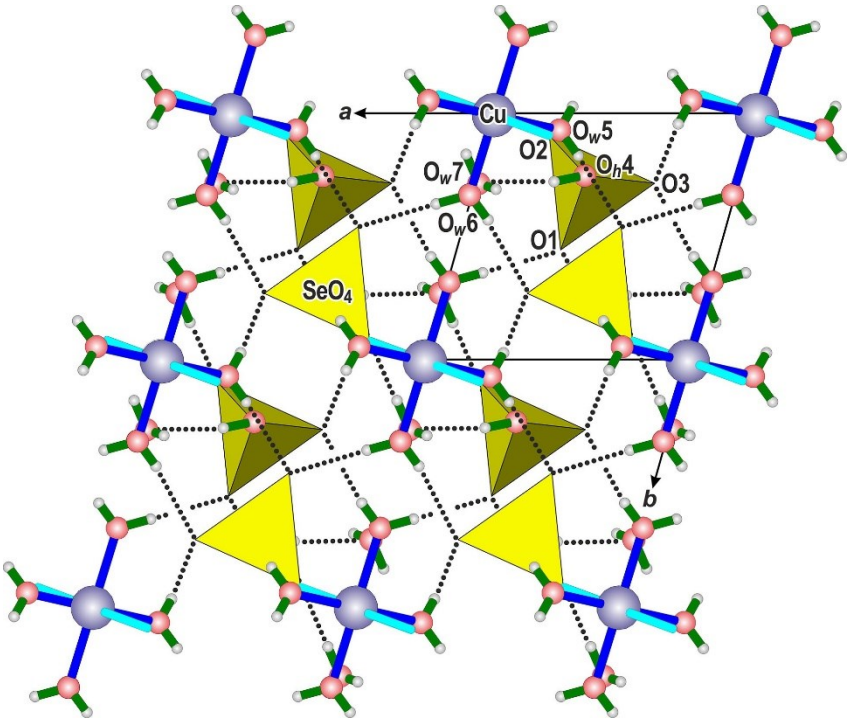

Fig. 2 The crystal structure of $Cu[SeO_3(OH)]_2 \cdot 6H_2O$ in a projection parallel to [001] on (110). "Short" and "long" Cu—O bond lengths are indicated in dark blue respectively turquoise colour.

Ferraris G, Ivaldi G (1984): X–OH and O–H···O bond lengths in protonated oxoanions. – Acta Cryst B40, 1–6

Kawahara A, Kageyama T, Watanabe I, Yamakawa J (1993): Structure du monophosphate synthétique de cuivre et de sodium. – Acta Cryst C49, 1275–1277

Snyman HC, Pistorius CWFT (1964): Polymorphism in the selenates of Mg, Mn, Co and Cu at high pressures. – Z Krist 120, 317–322

Zemann J (1961): Die Kristallchemie des Kupfers. – Fortschr Miner 39, 59–68

Zemann J (1972): Copper. 29-A, Crystal chemistry. – Handbook of Geochemistry, Vol. 11/3, Berlin-Heidelberg-New York: Springer

Josef Zemann (25. Mai 1923 – 16. Oktober 2022)

H.S. Effenberger[1], R. Miletich[1]

[1]*Institut für Mineralogie und Kristallographie, Universität Wien*
herta.silvia.effenberger@univie.ac.at

The MinWien2023 meeting is dedicated to Josef Zemann. He was teacher, mentor, colleague, and friend to many colleagues in Vienna but also all over the world. Josef Zemann was born in Vienna on 25 May, 1923, a time of economic uncertainties and social instabilities. His scientific career started with the doctoral thesis entitled "*Über die Struktur des Pharmakosiderits*", for which he received the academic degree *doctor philosophiae* on 17 July, 1946.

Inspired by crystallography, Josef Zemann stayed for one year at the Massachusetts Institute of Technology in Boston with Martin J. Bürger, one of the pioneers of X-ray crystallography. Quite shortly after his return to Vienna, he became associate professor and some years later full professor at the "Mineralogisch-Kristallographisches Institut" at the Georg-August-Universität in Göttingen. During this time Josef Zemann focussed primarily on topics in crystal chemistry, such as the stereochemistry of Li, Cu and Te atoms, electrostatic lattice energies, as well as crystal absorption spectra in the infrared range. His years in Göttingen constituted a fulfilled time, thanks to the great working conditions and an academically inspiring atmosphere. In 1967 he responded to the call to move to the University of Vienna and succeeded his former teacher Prof. Dr. Karl Ludwig Felix Machatschki. As the head the Institut für Mineralogie und Kristallographie at the Alma Mater Rudolfina - Universität Wien for 22 years until his retirement in 1989 he was scientifically active and an internationally recocknised expert in the field of mineralogical crystallography.

Josef Zemann's early work in Vienna, Bosten, and Göttingen was dedicated to the determination of crystal structures by X-ray diffraction. His interest was the recognition of the stereochemistry of cations, especially of Cu^{2+} and Te^{4+} ions that were basically unexplored at that time. In recognition of his research on the stereochemistry of Te^{4+} ions, a novel tellurite mineral was named after him, i.e. zemannite, $[Zn^{2+}Fe^{3+}(TeO_3)_3]_2[Mg(H_2O)_6{\cdot}nH_2O]$, $n \leq 3$. (Fig. 1).

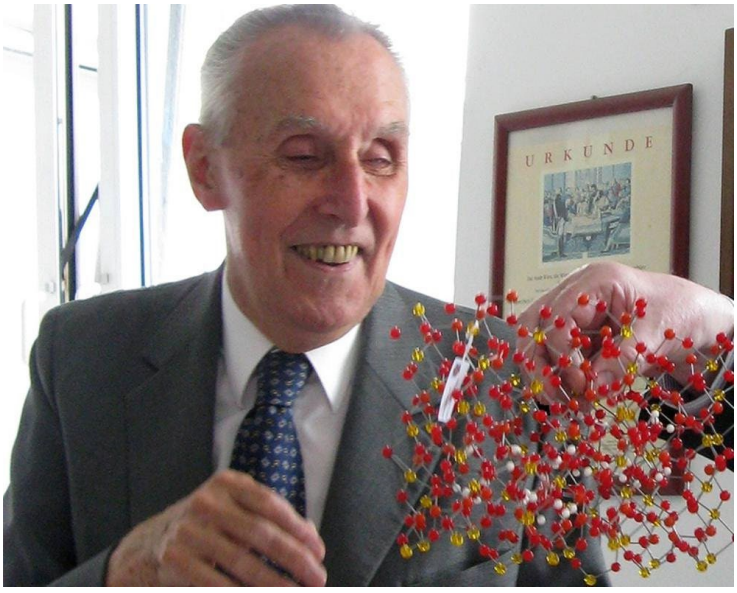

Figure 1. On the occasion of his 85th birthday in 2008 Josef Zemann receives a ball-and-stick model of the crystal structure of his mineral zemannite.
Foto: Kurt Mereiter

Among the milestones of his scientific work were infrared spectroscopic studies, were he tread new conceptual and methodological ground. At one hand he used polarized IR radiation and crystallographically oriented crystal platelets to localize hydrogen bonds associated with OH^- groups or H_2O molecules. At that time, it was practically impossible to localize H atom positions by means of X-ray diffraction techniques. Achievements in applying IR spectroscopy were groundbreaking as he recognized for the first time small amounts of hydroxyl groups to be detectable even in nominally anhydrous rock-forming silicates such as in olivine, andalusite, the three TiO_2 modifications, or in enstatite. Even here he was able to localise the orientation of the OH^- dipols in relation to the crystallographic orientation of the mineral samples and consequently to the atomic arrangement. In addition, it was also possible to discriminate between liquid inclusions and structurally oriented hydroxyl groups incorporated in the crystal lattice. The strong interaction between the IR radiation and the OH^--dipoles allow to detect concentrations in the tenth weight-percent range. In the 1960s it was doubtless assumed that the Earth's mantle does not contain any OH^- or H_2O contents. Today, it is estimated that due to the solubility in the above-mentioned minerals large quantities of OH^- and H_2O are stored in the upper 660 km of the Earth's mantle corresponding to the volume to the Earth's oceans.

Josef Zemann's broad scientific œuvre is supplemented by a series of papers dealing with the crystal chemistry of carbonates, focussing on both the structure types, their topological relations, as well as on the aplanarity of carbonate groups. The calculation of electrostatic lattice energies was a first step towards a modern atomistic modelling and the stability of structure types.

The significance of Josef Zemann's academic work and his reputation within the scientific community was honoured by a large number of honours and awards. He became honorary member of six National Mineralogical Societies (America, Austria, Soviet Union, Poland, Germany, and Romania). The ÖMG appointed him to their Honorary President. He received also numerous awards and medals: the Gustav-von-Tschermak-Seysenegg and the Erwin-Schrödinger medals (both from the Austrian Academy of Science), silver medals (the Abraham-Gottlob-Werner-Medal from the DMG and from the Masaryk University Bruno), a gold medal (Comenius University Bratislava), the Emanuel Bořicky Medal (Karlsuniversität Praha), and he became correspondent of the Geologische Bundesanstalt Wien.

Furthermore, his remarkable contribution to crystal chemistry and his input to the knowledge in mineralogical and crystallographic sciences was honoured by various scientific academic memberships. On leave from Göttingen and as a welcome to Vienna he became Corresponding Member of the Akademie der Wissenschaften zu Göttingen in 1967 and the Österreichische Akademie der Wissenschaften (the latter elected him 1972 as a Full Member). A further membership was awarded by the Academia Mediterranea delle Scienze (Catania, Italy) and a Honorary Membership by the Hungarian Academy of Sciences. He was elected as a Corresponding Member by the Kroatische Akademie der Wissenschaften und Künste and the Polish as well as the Croatian Academies of Sciences. He was particularly pleased, in fact he was proud to become a Member and Senator of the Deutsche Akademie der Naturforscher Leopoldina, which had already founded in 1652.

On the evening of 16 October 2022 Josef Zemann passed away gently and peacefully only a few months ahead of his 100^{th} birthday. His person, his tireless commitment and enthusiasm, his keen sense of observation, but also his kindness and humour remain unforgettable. We will remember Josef Zemann as our teacher, mentor, and an outstanding scientist.

Mechanisms of calcium carbonate mineral formation in a roman aqueduct near Cologne (Germany) - A microstructural and geochemical approach

I. Egartner[1], R. Boch[1], K. Grewe[2], M. Dietzel[1], D. Hippler[1]

[1]Graz University of Technology, Institute of Applied Geosciences, Rechbauerstraße 12, Graz, 8010, Austria
[2]Tannenstraße 18, 53913 Swisttal-Morenhoven, Germany
e-mail: egartner@student.tugraz.at

A special case of freshwater carbonate deposits in man-made settings are calcium carbonate ($CaCO_3$) scale deposits in aqueducts and water conduits of the roman times. They occur across the ancient expansion of the roman empire and therefore in different climate zones, from maritime to continental mid-latitude regions. Such scale deposits can serve as an archive, for the reconstruction of the physico-chemical environmental conditions, the palaeoclimate and the hydrogeology of the catchment and the aquifer. This study therefore aimed to investigate the ancient environmental physico-chemical conditions of the scale deposits of a roman aqueduct channel, the so called „Eifel-Wasserleitung“, that supplied water from the Eifel mountains to the roman city of Cologne, Germany by microstructural and geochemical proxies. In order to reveal the meso- and microstructural fabric as well as geochemical and stable isotope compositions of the $CaCO_3$ scale deposits, petrographic, mineralogical and geochemical analyses have been applied (e.g. light microscopy, XRD, Raman spectroscopy and LA-ICP-MS).

First results revealed differences in carbonate mineral nucleation and growth dynamics that are indicated by individual crystal shapes, arrangements and scale textures. The polished hand specimen of the investigated $CaCO_3$ scale deposit shows mesofabric characteristics of individual horizons ranging from 1 to 5 mm in size and low porosity. At the microfabric level, the calcite, which forms the individual laminae, shows different growth types, occurring as microsparit, elongated columnar calcite crystals and thin micritic layers. These growth types are well comparable to other investigations of $CaCO_3$ scale deposits in aqueducts of the roman empire, but they are also frequently found in freshwater carbonate deposits in man-made settings as well as in natural environments, like speleothems. The results of the macro- and microstructural characterization, major/trace element distributions (e.g., Mg, Ca, Sr, Ba) will be discussed in respect to reaction mechanisms and mineral growth rates, potential microorganic influence, and (water) discharge.

The incorporation of Li in the tourmaline structure

A. Ertl[1,2]

[1]Mineralogisch-Petrographische Abt., Naturhistorisches Museum, Austria,
[2]Institut für Mineralogie und Kristallographie, Universität Wien, Austria.
e-mail: andreas.ertl@a1.net

Using natural and synthetic samples, it was investigated which Li-containing short-range orders can occur in Li-bearing Al-rich tourmalines. The investigated samples have lattice parameters from $a = 15.72$, $c = 7.07$ Å to $a = 15.84$, $c = 7.10$ Å. The general tourmaline formula is $XY_3Z_6(BO_3)_3[T_6O_{18}]V_3W$, where the *X* site is usually occupied by Na, Ca or is vacant. The *Y* site is in such tourmalines usually occupied by Al and Li, and the *Z* site is only occupied by Al. The *T* site can be occupied by Si and by minor amounts of B and Al. The *V* site is usually occupied by OH and the *W* site by OH, O or F.

It is still not clear how Li enters the *Y* site in Li-rich tourmalines. Until now, syntheses have not been successful in producing Li-rich tourmalines (>0.5 apfu ^{Y}Li). It therefore makes sense to take a closer look at which short-range orders Li can be built into. Synthetic Al-rich and Li-bearing tourmalines with no F, but with $^{[4]}$B and $^{[4]}$Al are of special interest, because they contain no Ca, only Na and vacancies (□) at the *X* site and mainly Al and Li at the *Y* site (Ertl et al., 2012). Since these tourmalines (synthesized by David London) do not have such a complex composition, relationships are easier to recognize. In Tab. 1 all short-range orders are listed which can contribute to these synthetic samples (*Z* site is always occupied by Al).

Table 1. Short-range orders in synthetic tourmaline

Number	*X* site	*Y* site	*T* site	*W* site
1.1	Na	Al_2Li	Si_5B	OH
1.2	Na	Al_2Li	Si_5Al	OH
1.3	Na	Al_3	Si_4B_2	O
2.1	□	Al_2Li	Si_6	OH
2.2	□	Al_3	Si_5B	O
2.3	□	Al_3	Si_5Al	O

Short-range order 2.1 is related to the rossmanite end-member. Short-range order 2.3 is related to the alumino-oxy-rossmanite end-member (Ertl et al., 2022), while 2.2 is related to the B-analogue of this tourmaline. It seems confirmed that the short-range order 1.3 is an essential component. Without it, it is not possible to explain the crystal chemical formulae of these synthetic tourmaline samples. The combination of these different short-range orders makes it clear that the Li content in such a tourmaline containing only Na and vacancies at the *X* site will be in the range of 0–1 apfu Li. When correlating the component of the different short-range orders in the examined tourmalines, which were synthesized at different temperatures, it can be recognized that with decreasing temperature the component of 2.1 increases, while it decreases with increasing temperature. This explains why the content of the tetrahedrally coordinated B towards lower temperatures significantly increases. There is no evidence that in these synthetic tourmalines a short-range order occurs, where the *X* and *Y* sites are occupied as in 1.1, but exclusively Si occupies the *T* site and only O occupies the *W* site. Such a short-range order may not be favourable at such pressure/temperature conditions or perhaps even unstable.

A natural Al-rich and Li-bearing tourmaline sample with a vacancy-dominant *X* site (rossmanite; Selway et al., 1998) with the updated crystal chemical formula $^{X}(\square_{0.6}Na_{0.4})$ $^{Y}(Al_{2.2}Li_{0.7}\square_{0.1})$ $^{Z}Al_6$ $(BO_3)_3$ $[Si_{5.6}B_{0.4}O_{18}]$ $^{V}(OH)_3$ $^{W}[(OH)_{0.6}O_{0.3}F_{0.1}]$ seems to consist of the same short-range orders. A minor component may occur additionally: a short-range order with ^{X}Na, $^{Y}(Al_2\square)$, ^{T}Si and ^{W}(OH) (see also Ertl, 2023). However, the dominant component is short-range order 2.2 (Tab. 1), which is not surprising.

There occur natural Al- and Li-rich tourmalines with Li >1.0 apfu. Such tourmalines contain additionally some Ca and significant amounts of F (*e.g.*, Ertl et al., 2006, 2010). The short-range orders occurring in such samples are already listed in Tab. 1, but additional short-range orders might also occur, which are listed in Tab. 2.

Table 2. Additional theoretical short-range orders in natural Al- and Li-rich samples

Number	*X* site	*Y* site	*T* site	*W* site
1.4	Na	Al_2Li	Si_5B	F
1.5	Na	Al_2Li	Si_5Al	F
2.4	□	Al_2Li	Si_6	F
3.1	Ca	Li_2Al	Si_6	F
3.2	Ca	Li_2Al	Si_6	OH
3.3	Ca	$Al_2\square$	Si_5Al	OH
3.4	Ca	$Al_2\square$	Si_5B	OH

Short-range orders 3.1 and 3.2 have (Li_2Al) at the *Y* site. The combination of these components together with short-range orders 1.1, 1.2, 1.4, 1.5, 2.1 and 2.4 produces Li contents in the range 1-2 apfu Li. However, the 2.4 short-range order does not appear to occur, as a summary of approximately 9000 tourmaline analyses from different lithological environments show that for tourmaline with an average *X*-site charge of <+0.5, the maximum F amounts are <0.2 apfu (Henry & Dutrow, 2011). These chemical data of natural tourmalines indicate crystallographic influences. Natural tourmaline with relatively high Li contents always contains relatively high F contents. It seems that the contents of Li and the F are positively correlated (Ertl, 2021). It is therefore possible that short-range orders with Li and F (1.4, 1.5, 3.1; Table 2) are crystal-chemically more favourable than orders with Li and OH (1.1, 1.2, 2.1; Tab. 1; 3.2; Tab. 2). However, further investigations seem to be necessary.

This research was funded by the Austrian Science Fund (FWF) project P 35585.

Ertl A (2021): Why was it not possible to synthesize Li-rich tourmaline? - NATURA 111, 31–32

Ertl A (2023): Are the [6]−coordinated sites in tourmaline in certain cases partially vacant? Mineral Petrol 117, DOI: 10.1007/s00710-023-00815-4

Ertl A, Hughes JM, Prowatke S, Ludwig T, Prasad PSR, Brandstätter F, Körner W, Schuster R, Pertlik F, Marschall H (2006): Tetrahedrally coordinated boron in tourmalines from the liddicoatite-elbaite series from Madagascar: Structure, chemistry, and infrared spectroscopic studies. - Amer Mineral 91, 1847–1856

Ertl A, Rossman G, Hughes JM, London D, Wang Y, O'Leary JA, Darby MD, Prowatke S, Ludwig T, Tillmanns E (2010): Tourmaline of the elbaite-schorl series from the Himalaya Mine, Mesa Grande, California: A detailed investigation. - Amer Mineral 95, 24–40

Ertl A, Giester G, Ludwig T, Meyer H-P, Rossman GR (2012): Synthetic B-rich olenite: Correlations of single-crystal structural data. - Amer Mineral 97, 1591–1597

Ertl A, Hughes JM, Prowatke S, Ludwig T, Lengauer CL, Meyer H-P, Giester G, Kolitsch U, Prayer A (2022): Alumino-oxy-rossmanite from pegmatites in Variscan metamorphic rocks from Eibenstein an der Thaya, Lower Austria, Austria. - Amer Mineral 107, 157–166

Henry DJ, Dutrow BL (2011): The incorporation of fluorine in tourmaline: internal crystallographic controls or external environmental influences? - Canad Mineral 49, 41–56

Selway JB, Novák M, Hawthorne FC, Černý P, Ottolini L, Kyser TK (1998): Rossmanite, $\square(LiAl_2)Al_6Si_6O_{18}(BO_3)_3(OH)_4$, a new alkali-deficient tourmaline: description and crystal structure. - Amer Mineral 83, 896–900

Ammonium-iron-sulfites from a burning coal-mine dump

B. Fehér[1], S. Szakáll[2], M. Ende[3], H.S. Effenberger[3], J. Mihály[4], I. Sajó[5], L. Kótai[4], D. Szabó[6]

[1]Department of Mineralogy, Herman Ottó Museum, Miskolc, Hungary
[2]Institute of Mineralogy and Geology, University of Miskolc, Hungary
[3]Institut für Mineralogie und Kristallographie, Universität Wien, Austria
[4]Institute of Materials and Environmental Chemistry, Research Centre for Natural Sciences, Budapest, Hungary
[5]Szentágothai Research Centre, University of Pécs, Hungary
[6]Department of Mineralogy, Eötvös Loránd University, Budapest, Hungary
e-mail: herta.silvia.effenberger@univie.ac.at

Three ammonium-iron-sulfites from a burning coal dump in an abandoned open coal pit at Pécs-Vasas (Mecsek Mountains, South Hungary) were identified. They were formed by the interaction of decomposing iron sulfides and ammonia released from organic matter. For synthetic analogues to these natural phases see Erämetsä (1943); Erämetsä & Valkonen (1972); Kocsis et al. (2018).

$(NH_4)_9Fe^{3+}(SO_3)_6$ is metastable and decomposes quickly. Larsson & Niinistö (1973) performed a crystal-structure investigation in space group $P\bar{3}$ from powder X-ray data. Identity with the natural samples was proved. Isolated $Fe^{2+}O_6$ polyhedra are corner-connected to sulfite anions. Each corner is shared with an O atom of a $(SO_3)^{2-}$ group forming $[Fe^{3+}(SO_3)_6]^{9-}$ clusters (Fig. 1). Thus, only one O atom of the sulfite group links to a FeO_6 octahedron; the others are acceptor atoms of the hydrogen bonds.

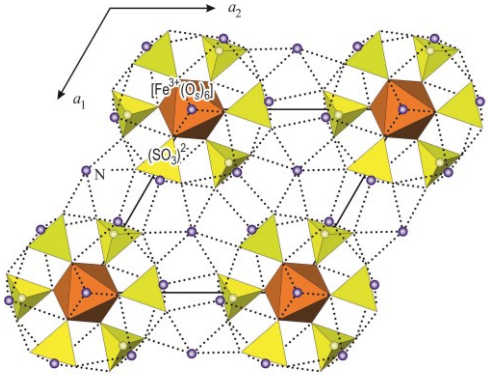

Figure 1. The crystal structure of $(NH_4)_9Fe^{3+}(SO_3)_6$

$(NH_4)_2Fe^{2+}(SO_3)_2$ (AIS-2) crystallizes in space group $R\bar{3}m$ and is characterized by a 2D net with composition $[Fe^{2+}(SO_3)_2]^{2-}$ (Fig. 2). All three O atoms belonging to the sulfite group represent corners in FeO_6 octahedra. Thereby two layers of O atoms are parallel to (0001) and in a close packed arrangement. 1/4 of the octahedral voids in this double layer are filled by Fe^{2+} ions. The apical S atom points into the 2D net, the lone-electron pairs are centred in the $[Fe(SO_3)_2]^{2-}$ layer.

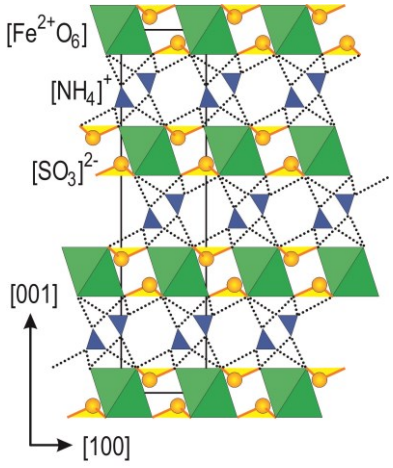

Figure 2. The crystal structure of $(NH_4)_2Fe^{2+}(SO_3)_2$

The crystal structure is topologically equivalent to the buetschliite-type selenites $K_2Mn(SeO_3)_2$ and $K_2Co(SeO_3)_2$ (Wildner 1992a,b). Also carbonates like eitelite and buetschliite $[Na_2Mg(CO_3)_2, K_2Ca(CO_3)_2]$, are representatives belonging to this connection schema; here the C atom of the CO_3 triangles are close to the O atom layers as only minor but significant aplanarities of the carbonate groups are verified (Knobloch et al. 1980; Effenberger & Langhof 1984). Like for in the sulfites and selenites, the apex of the carbonate points towards the octahedral layer; as pointed out by Zemann (1981) towards the smaller and higher charged cations where one expects stronger covalent contributions to the chemical bonds between the cations and oxygen atoms.

$(NH_4)_2Fe^{3+}(OH)(SO_3)_2{\cdot}H_2O$ (Fig. 3) crystallizes in space group *Cmcm* and exhibits $[Fe^{3+}(OH)(SO_3)_2]^{2-}$ chains. The Fe^{3+} ions are octahedrally coordinated to four O atoms belonging to sulfite groups (O_s atoms) and to two oxygen atoms belonging to hydroxyl groups (O_h atoms). These FeO_6 octahedra are corner linked to buckled chains; each two *trans*-arranged O_h atoms are shared and represent the backbone of the $[Fe^{3+}(OH)(SO_3)_2]^{2-}$ chains. The shape of these chains is related to a wind wheel with the selenite groups pointing off the $[Fe(O_s)_4O_h]^{7-}$ columns. About 8 % of the Fe^{2+} ions are displaced along the *c* axis (the Fe' position is 0.64 Å apart from the Fe atom).

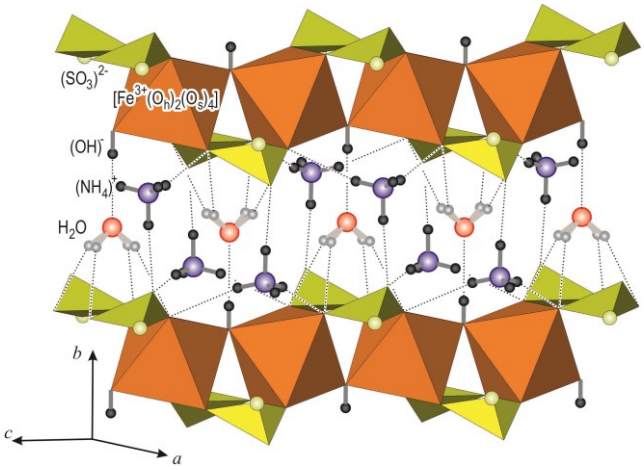

Figure 3. The crystal structure of the new mineral kollerite, $(NH_4)_2Fe^{3+}(OH)(SO_3)_2{\cdot}H_2O$

Intercalated between the $[Fe^{3+}(OH)(SO_3)_2]^{2-}$ chains are the water molecules and the ammonium cations. Linkage is achieved by hydrogen bonds only. Despite this loose connection, the $(NH_4)^+$ group is ordered and forms clearly defined hydrogen bonds. As the O_w atom has site symmetry *m*2*m*, the water molecules exhibit a site disorder with respect to the H atoms at least for the structure model in space group *Cmcm*. As only two H atoms per formula unit are affected, order (neither by a reduction of symmetry nor by an enlargement of the unit cell) could be proved.

It is remarkable that for a crystal size of 6×7×65 μm^3 it was possible to refine the half occupied H atom position without any restrictions (*i.e.*, with variable atomic coordinates and a variable isotropic displacement parameter). The H_2O molecules – like the Fe' atoms – exhibit an orientational disorder violating at least locally the *centro*-symmetry. X-ray data were collected at 220 K using a Stoe-StadiVari diffractometer equipped with a Dectris Pilatus 300 K pixel detector. It was operated with monochromatized MoKα radiation from a 100 W air-cooled Incoatec IμS micro-focus X-ray tube (50 kV, 1 mA).

Effenberger H, Langhof H (1984): On the aplanarity of the CO_3 group in buetschliite, dipotassium calcium dicarbonate, $K_2Ca(CO_3)_2$. A further refinement of the atomic arrangement. - Acta Cryst C40, 1299-1300

Erämetsä O (1943): Über Ammonisulfitoferriate. - Ann Acad Sci Fenn Ser A LIX, 5-30

Erämetsä O, Valkonen J (1972): Ammonium ferric sulfites. Suomen Kemistilehti 45, 91–94

Knobloch D, Pertlik F, Zemann J (1980): Crystal structure refinements of buetschliite and eitelite: a contribution to the stereochemistry of trigonal carbonate minerals. N Jb Mineral Mh 1980 230-236

Kocsis T, Magyari J, Sajó IE, Pasinszki T, Homonnay Z, Szilágyi IM, Farkas A, May Z, Effenberger H, Szakáll S, Pawar RP, Kótai L (2018): Evidence of quasi-intramolecular redox reactions during thermal decomposition of ammonium hydroxodisulfitoferriate(III), $(NH_4)_2[Fe(OH)(SO_3)_2]{\cdot}H_2O$. - J Therm Anal Calorim 132, 493–502

Larsson LO, Niinistö L (1973): The crystal structure of ammonium hexasulphito-ferrrate(III), $(NH_4)_9[Fe(SO_3)_6]$. - Acta Chem Scand 27, 859–867

Wildner M (1992a): Structure of $K_2Mn(SeO_3)_2$, a further buetschliite-type selenite. - Acta Cryst C48, 595

Wildner M (1992b): Isotypism of a selenite with a carbonate: structure of the buetschliite-type compound $K_2Co(SeO_3)_2$, a further selenite. - Acta Cryst C48, 410-412

Zemann J (1981): Zur Stereochemie der Karbonate. - Fortschr Mineral 59 95–116

Petrology and geochemistry of the Haddo House – Arnage district contact aureole, Aberdeenshire / Scotland

A. Fehleisen[1], C.A. Hauzenberger[1], J. Booth[1]

[1]University of Graz, Department of Earth Sciences, Universitätsplatz 2, 8010 Graz
e-mail: anna.fehleisen@edu.uni-graz.at

In Aberdeenshire, NE Scotland, a suite of gabbroic intrusions was intruded roughly contemporaneous to peak regional metamorphism during the middle Ordovician Grampian orogenic event. This study is based on samples collected from the Belhelvie, Haddo House, Arnage and Huntly gabbro intrusions, their metamorphic aureoles and zones of contact anatexis. The intrusions are classified as various types of gabbro and norite, composed of anorthite-rich plagioclase, olivine (usually partially or completely altered) and pyroxenes. Many samples collected at the boundary of the intrusions are norites, with significant amounts of cordierite and biotite, indicating they probably formed from magma mixing with partial melts produced by anatexis of the country rocks. The parageneses of the overprinted metapelites of the country rock range from high grade hornfels within a few meters of the gabbro contact, with Opx+Grt+Sp+Plg+Bt+Crd+Cor assemblages, transitioning further out into middle-high grade Sill+Grt+Bt and calc-silicate rich assemblages, overprinting previous regional metamorphic assemblages that contained And+Cor. The high grade hornfels often contain thin, whispy, more leucocratic veinlets thought to be produced by partial melting. These mineral paragenesis, whole rock and mineral chemistry have been used to reconstruct PT-conditions. Preliminary geothermobarometric calculations indicate that the highest grade hornfels experienced peak conditions of around 900 °C and 4-6 kbar. Further studies are being conducted using trace elements distribution help to understand the role and origins of fluids involved in the metamorphism of the aureole and related anatexis. U-Pb age dating on zircons and monazites extracted from many samples will help constrain the absolute ages of both the gabbro intrusions and the adjacent regionally metamorphosed rocks. This range of methods should deliver new insights on the causal and temporal relationship between these intrusions and the regional metamorphic events (see Droop et al. 2003; Pattison et al. 2022).

Droop GTR, Clemens JD, Dalrymple DJ (2003): Processes and conditions during contact anatexis, melt escape and restite formation: the Huntly Gabbro Complex, NE Scotland. - J Petrol 44, 995-1029

Pattison DR, Goldsmith SA (2022): Metamorphism of the Buchan type-area, NE Scotland and its relation to the adjacent Barrovian domain. - J Geol Soc 179, https://doi.org/10.1144/jgs2021-040

P-T-t evolution of the Pulkau and Pleißing Nappes from the Moravo-Silesian Thaya Window, Lower Austria

M.J. Findl[1], C.A. Hauzenberger[1], E. Skrzypek[1], D. Gallhofer[1], M. Linner[2]

[1]Department of Earth Sciences - NAWI Graz Geocenter,
University of Graz, Universitätsplatz 2, 8010 Graz, Austria
[2]Department of Hard Rock Geology, GeoSphere Austria,Neulinggasse 38, 1030 Vienna, Austria
e-mail: martin.findl@edu.uni-graz.at

The Moravo-Silesian Zone in the Bohemian Massif is a ~300 km long deformation zone that formed through underthrusting of the Brunia microcontinent beneath the Moldanubian–Lugian domain. The Moravo-Silesian zone crops out in three tectonic windows which are from north to south: (1) the Silesian zone, (2) the Svratka and (3) the Thaya windows, the last two being known as the Moravian zone sensu stricto. The Svratka and Thaya windows consist of a parautochthonous basement, a ~7 km thick pile of two nappes (the Lower and Upper Moravian Nappes) (Štípská et al. 2015). In relation to local ductile and brittle-ductile shear zones, only one major regional thrust runs through the Thaya Window, which separates the tectonically upper Pleißing (Lower and Upper Moravian Nappes) from the tectonically lower Pulkau Nappe (basement) (Linner et al. 2021). The research area is located in the Austrian part of the Thaya Window.

Samples taken along two SE-NW trending profiles (A and B) were used to constrain the P-T-t evolution of the Thaya Window using petrological modelling together with U-Pb zircon and Th-U-Pb monazite dating. Profile A, northern Thaya window: P-T estimates for the Pulkau Nappe are ~600 °C and 6.5-7.5 kbar and for the Pleißing Nappe slightly higher conditions of 550 °C up to 630 °C and 11 kbar. Graphite thermometry indicates 550±30 °C for the Pleißing Nappe. Two phase garnets can be clearly recognised in one sample. Inner garnet cores indicate P-T conditions of ca. 550 °C/5 kbar and inner garnet rims ca. 630 °C and 6 kbar.

Profile B, central Thaya Window: P-T estimates for the Pulkau Nappe are 600 °C and 8 kbar. Temperature is estimated to 603±30 °C (graphite thermometry) and 606±15 °C (Zr in rutile thermometry). The Pleißing Nappe exhibits 650-660 °C and 10.5-11 kbar, while graphite thermometry points to lower temperatures of 570±30 °C and 530±30 °C.

The Ky-Grt micaschists from Meiseldorf (Upper Moravian Nappe after Štípská et al. (2015); northwestern part of the Pleißing Nappe after Linner et al. (2021)) indicate 680-720 °C and 8-8.5 kbar based on petrological modelling and Zr in rutile thermometry.

Zircon dating by LA-MC-ICP-MS yields a weighted mean protolith $^{206}Pb/^{238}U$ age of 588±7.8 Ma for a metatuffite belonging to the Pleißing Nappe (profile A) and 592±7.8 Ma for a metatuffite from the Pulkau Nappe (profile B). Monazite commonly occurs in metapelite with grain sizes from 10-50 µm. In rare cases monazite can reach up to 100 µm. Th-U- total Pb chemical dating of monazite by EPMA yields 301-344 Ma in the Pleißing Nappe. $^{206}Pb/^{238}U$ monazite dates by LA-MC-ICP-MS range from 312 to 356 Ma.

We provide the first evidence for Ediacarian magmatism and coeval sedimentation for the protoliths of the Moravian zone. We confirm the occurrence of regional metamorphism from lower amphibolite to lower granulite facies conditions in the Austrian part of the Moravian zone and propose that peak P-T conditions were attained between 312 and 356 Ma based on monazite dating.

Linner M, Rötzel R, Huet B, Hintersberger E (2021): A new subdivision for the Moravian Superunit - The redefined Pleißing and the newly defined Pulkau nappe. – In: Proceedings of the 4th Friends of the Bohemian Massif Meeting, October 7-10, Freistadt, Austria, 10

Štípská P, Hacker BR, Racek M, Holder R, Kylander-Clark ARC, Schulmann K, Hasalová P (2015): Monazite dating of prograde and retrograde P–T–d paths in the Barrovian Terrane of the Thaya Window, Bohemian Massif. - J Petrol 56, 1007–1035, url: https://doi.org/10.1093/petrology/egv026

Computational studies of zeolites as adsorbents for the removal of pharmaceuticals and personal care products

M. Fischer[1,2], J. Brauer[1,2]

[1]Crystallography & Geomaterials Research, Faculty of Geosciences, University of Bremen, Germany
[2]Bremen Center for Computational Materials Science and MAPEX Center for Materials and Processes, University of Bremen, Germany
e-mail: michael.fischer@uni-bremen.de

Pharmaceuticals and personal care products (PPCPs) have received considerable attention as emerging organic contaminants, with some members of this diverse group of compounds possessing a significant environmental hazard potential (Patel et al. 2019). Conventional wastewater treatment plants are not designed for the removal of these species, and a number of PPCPs show recalcitrant behaviour, entering water bodies and other environmental compartments. Adsorption-based processes constitute one possible technology that can improve the PPCP removal efficiency of wastewater treatment facilities. While carbon-based adsorbents are the most widely studied option, hydrophobic high-silica zeolites could be attractive alternatives due to their good regenerability and reduced co-adsorption of natural organic matter (Jiang et al. 2018). In this contribution, it will be discussed how atomistic modelling methods at different levels of theory can be employed to predict and understand the PPCP adsorption behaviour of these materials.

Given the diversity of zeolite frameworks that are available in highly siliceous form and the even larger number of PPCPs of possible environmental relevance, it is evident that an experimental investigation of all zeolite-PPCP combinations of potential interest would be extremely laborious. In previous work, it could be shown that relatively simple force field simulations deliver host-guest interaction energies that are well correlated with experimental removal efficiencies, providing a pathway to determine zeolite-PPCP combinations of potential interest prior to an experimental characterisation (Fischer 2020). Expanding upon this work, the implementation of a multi-step screening procedure allowed the exploration of a large number of combinations (>10 zeolites, >50 PPCPs) at relatively modest computational cost. Additionally, the capabilities of more sophisticated molecular dynamics simulations to calculate free energies of adsorption were explored. Such simulations allow direct predictions whether a given contaminant will be adsorbed in the zeolite or remain in solution.

Whereas the force field simulations are primarily employed for predictive purposes, dispersion-corrected density functional theory (DFT) calculations enable a more detailed understanding of the interactions that govern PPCP adsorption. Two recent studies dealt with the adsorption of carbamazepine (CBZ, Fig. 1a), an anticonvulsant medication, and triclosan (TCS, Fig. 1a), a disinfectant and preservative agent that is widely used in various products, in different zeolites (Fischer 2023a, Fischer 2023b). It was observed that the topology of the zeolite framework has a significant impact on the CBZ adsorption energy, whereas the interaction with TCS is largely determined by the pore size. This qualitative difference can be explained with the higher flexibility of TCS, which can adjust more readily to different pore shapes than the fairly rigid CBZ molecule. In addition to analysing factors that determine the strength of host-guest interactions, guest-guest interactions between co-adsorbed CBZ molecules were investigated. The study of TCS adsorption also addressed the competitive adsorption of the organic contaminant and water in zeolites having different framework compositions (all-silica zeolites and highly siliceous aluminosilicates, see Fig. 1b), permitting insights into the role of adsorbent hydrophobicity.

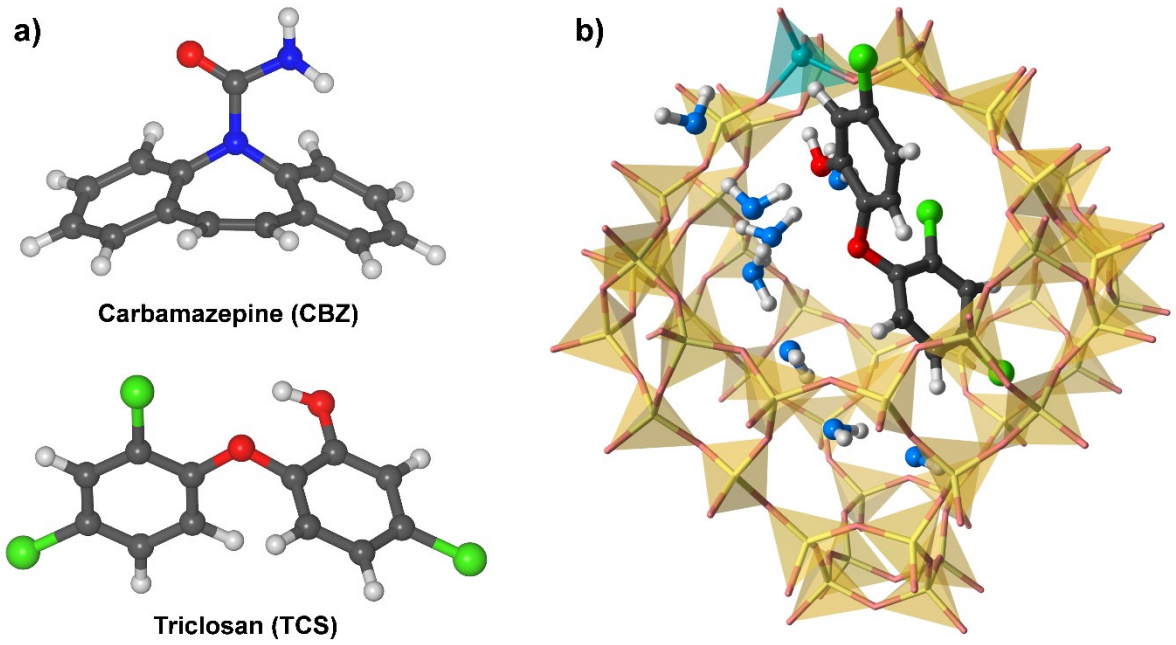

Figure 1. a) Molecular structures of carbamazepine and triclosan. b) Representative snapshot from a DFT-based molecular dynamics simulation addressing the co-adsorption of TCS and H_2O in protonated FAU-type zeolite.

Funding by the German Research Foundation (Deutsche Forschungsgemeinschaft) is gratefully acknowledged (projects 455871835 and 492604837).

Fischer M (2020): Simulation-based evaluation of zeolite adsorbents for the removal of emerging contaminants. – Mater Adv 1, 86

Fischer M (2023a): Adsorption of carbamazepine in all-silica zeolites studied with density functional theory calculations. – Chem Phys Chem 24, e202300022

Fischer M (2023b): Density functional theory study of hydrophobic zeolites for the removal of triclosan from aqueous solution. – Environ Sci Adv – accepted manuscript, DOI: 10.1039/D3VA00078H

Jiang N, Shang R, Heijman S G J, Rietveld, L C (2018): High-silica zeolites for adsorption of organic micro-pollutants in water treatment: A review. – Water Res 144, 145

Patel M, Kumar R, Kishor K, Mlsna T, Pittman C U, Mohan D (2019): Pharmaceuticals of Emerging Concern in Aquatic Systems: Chemistry, Occurrence, Effects, and Removal Methods. – Chem Rev 119, 3510

Twinning of götzenite and wöhlerite from the Fohberg phonolite, Kaiserstuhl

R.X. Fischer[1], J. Birkenstock[1], G. Biskup[2], L.A. Fischer[3], W.-A. Kahl[4], A. Klügel[1], S. Spürgin[5]

[1]FB 5 Geowissenschaften, Universität Bremen, Klagenfurter Straße, 28359 Bremen, Germany
[2]Breslauer Straße 6a, 75181 Pforzheim, Germany
[3]Institut für Geo- und Umweltwissenschaften, Geochemie, Albert-Ludwigs-Universität Freiburg, Germany
[4]MAPEX Center for Materials and Processes, University of Bremen, 28359 Bremen, Germany
[5]Hans G. Hauri KG, Mineralstoffwerke, Bergstraße 114, 79268 Bötzingen, Germany
e-mail: rfischer@uni-bremen.de

Götzenite and wöhlerite were found as part of a fissure assemblage in the Fohberg phonolite (Kaiserstuhl, SW Germany), in close association with natrolite and clinopyroxene (aegirine-augite). Both minerals have a similar appearance with yellowish brown prismatic crystals as shown in Fig. 1. Single species were separated and investigated by single-crystal X-ray diffraction (SXRD), electron probe microanalyzer (EPMA), laser ablation inductively coupled plasma mass spectrometry (LA-ICP-MS), and X-ray diffraction contrast tomography (DCT) showing the presence of two different phases, götzenite and wöhlerite.

Figure 1. Yellowish brown crystals of götzenite and wöhlerite in association with natrolite (white) and clino-pyroxene (black). Widths of figures are 11 cm (top) and 5.7 mm (bottom), respectively.

Götzenite has a chemical composition of $Na_{1.5}Ca_{5.1}Sr_{0.1}Zr_{0.1}Ti_{0.8}Nb_{0.2}(Si_2O_7)_2O_{0.4}F_{3.7}$ with additional Fe+Mn+REE < 0.3. SXRD revealed rotation twinning on [001] (twin matrix -**a**-1/2**c**, -**b**, **c**; twin components 40:60) with lattice parameters a = 9.6191(3) Å, b = 5.7342(2) Å, c = 7.3386(2) Å, α = 89.986(1)°, β = 101.040(1)°, γ = 100.485(1)°, triclinic, space group $P\bar{1}$, refined to R1 = 3.4 %.

Wöhlerite has a chemical composition of $Na_{1.6}Ca_{4.4}Fe_{0.2}Mn_{0.1}Zr_{0.6}Ti_{0.2}Nb_{0.8}(Si_2O_7)_2O_{2.4}F_{1.4}$ with additional Sr + REE < 0.05. SXRD revealed rotation twinning on [001] (twin matrix -**a**-**c**, -**b**, **c**; twin components 31:69) with lattice parameters a = 10.842(1) Å, b = 10.249(1) Å, c = 7.2673(8) Å, β = 109.344(4)°, monoclinic, space group $P2_1$, refined to R1 = 1.3 %.

The crystal structures closely resemble those of untwinned götzenite (Christiansen et al. 2003; Bellezza et al. 2004) and untwinned wöhlerite (Mellini et al. 1979; Biagoni et al. 2012), respectively.

Bellezza M, Merlino S, Perchiazzi N (2004): Chemical and structural study of the Zr,Ti-disilicates in the venanzite from Pian di Celle, Umbria, Italy. – Europ J Mineral 16, 957-969

Biagoni C, Merlino S, Parodi GC, Perchiazzi N (2012): Crystal chemistry of minerals of the wöhlerite group from the Los Archipelago, Guinea. – Canad Mineral 50, 593-609

Christiansen CC, Johnsen O, Makovicky E (2003): Crystal chemistry of the rosenbuschite group. – Canad Mineral 41, 1203-1224

Mellini M, Merlino S (1979): Refinement of the crystal structure of wöhlerite. – Tschermaks Mineral Petrogr Mitt 26, 109-125

Metamorphic reaction kinetics at anhydrous to water-saturated conditions

M. Franke[1], B.C. Schmidt[2], R. Stalder[1], B. Joachim-Mrosko[1]

[1]University of Innsbruck, Institute of Mineralogy and Petrography, Innrain 52, 6020 Innsbruck
[2]Department of Mineralogy and Petrology, Geoscience centre, Georg-August-University Göttingen, Goldschmidtstraße 1, 37077 Göttingen
e-mail: bastian.joachim@uibk.ac.at

Metamorphic coronas and reaction rim structures are examples of a net-transfer reaction, where pre-existing mineral phases react to new phases. Growth of these metamorphic structures indicates a change in physical parameters such as pressure or temperature. One of the most important parameters that controls reaction rim growth is the presence of volatiles, which can affect rim thicknesses, phase stabilities or rim microstructures (e.g., Gardés et al. 2012). This implies that reaction rims have the potential to decipher the P-T-t-X history of a sample of interest.

In this study, reaction rim growth experiments were performed between periclase and quartz at nominally anhydrous to water-saturated conditions between 3 to 4 kbar and 1100 to 1300 °C for 66-168 h. Controlled minute amounts of water were added through OH-doped periclase, which allowed to perform experiments at controlled water-undersaturated conditions. For water-saturated experiments that contain wt% amounts of H_2O, controlled amounts of water were added in the form of brucite powder to the samples.

At anhydrous conditions, no reaction rim formed implying that water acts as a catalyst, and a minimum fluid threshold is needed to initiate metamorphic re-equilibration. In all experiments that used either water-doped periclase or brucite as source of water, the rim sequence Per | Fo | En | Qz developed. At water-undersaturated conditions, addition of minute amounts of water results in an increase in the overall reaction rim growth rate by more than 2 orders of magnitude while the relative forsterite/enstatite ratio increases from 0.6 to 2.4. At water-saturated conditions, growth rates reach a plateau valeau between 10^{-15} and 10^{-14} m^2/s while forsterite/enstatite thickness ratios vary between 3 and 12.

This implies that reaction rim growth rates have the potential to monitor variations in water activity at those grain boundaries that serve as fast pathways for component transport at water-undersaturated conditions during metamorphic and metasomatic reactions in natural systems, allowing them to be used as sensitive “geohygrometers”. Additionally, the effect of water on relative layer thicknesses may provide an application for reaction rim microstructures to be used as new physico-chemical gauges that will allow us to discriminate between water-undersaturated and water-saturated conditions during metamorphic events.

Gardés E, Wunder B, Marquardt K, Heinrich W (2012): The effect of water on intergranular mass transport: New insights from diffusion-controlled reaction rims in the MgO-SiO_2 system. - Contr Mineral Petrol 164, 1–16

Bi-Te-S biomineralization in Precambrian Volyn biota (Ukraine)

G. Franz[1], R. Wirth[2], A. Schreiber[2], V. Khomenko[1,3]

[1]Institut für Angewandte Geowissenschaften, Technische Universität Berlin
[2]Deutsches GeoForschungsZentrum Potsdam
[3]Institute of Geochemistry, Mineralogy and Ore Formation, Academy of Sciences, Kyiv
e-mail: gefra548@gmail.com; gerhard.franz@tu-berlin.de

The Volyn biota represent an ancient subsurface lithautotrophic microecosystem with a minimum age of ca. 1.5 Ga (Franz et al. 2023). The fossils are exceptionally well preserved in 3D due to their occurrence in cavities of pegmatites of the 1.8 to 1.7 Ga old Korosten Pluton in NW Ukraine, which experienced no diagenesis, metamorphism or deformation, which is very often the case in sediments. The fossilization occurred during influx of hot, HF-bearing fluids from the granitic source into the large miarolitic cavities, producing a µm-wide rim of Al-silicate minerals (Franz et al., 2022). Some of the fossils were interpreted as biofilms (extracellular protein substance), others show similarities to filamentous fungi-like organisms, supported by the presence of chitosan, others are interpreted as methanogenic organisms.

In some of these filamentous and bulbous fossils we identified mineral inclusions with a size of approximately 50 to 100 nm. These nano-inclusions occur in the central part of the fossils, excluding their origin as post-mortem inclusions. Their composition is variable in the samples, but all are characterized by Bi-Te-S. In one sample they are randomly oriented in a distance of several micrometer. The composition is close to the minerals ingodite Bi(S,Te) or joseite $Bi_4(S,Te)_3$.

In another sample, they occur in a central channel of the organisms, characteristic for some of the filamentous fossils. These nanoparticles are up to approximately 200 nm large, concentrated in aggregates, and their composition is dominantly Bi-Cu-S with Te and Pb as additional components. Electron diffraction patterns of these mosaic crystals indicate an orthorhombic phase with a = 7.70 Å, b = 10.4 Å, c = 6.75 Å, consistent with the phase Cu_3BiS_3. Crystals away from the channel show the same composition Bi-Te-Pb-Cu.

In a bulbous fossil object, the nano-sized biominerals are arranged in groups of several crystals. Their composition is dominantly Bi-Te-S. These crystals are connected by a filament of amorphous material, a few nanometers wide, and similar filamentous extensions from the nanocrystals were observed (Fig. 1).

In modern fungi, Liang et al. (2019) observed the formation of Te- (and Se-) nanoparticles during growth experiments with different fungal species, and microbial reduction of Te (and Se) species shows the immobilization of these elements in intracelular and extracelular nanoparticles (Liang et al., 2020), supporting the interpretation of the fossils as fungi-like organisms.

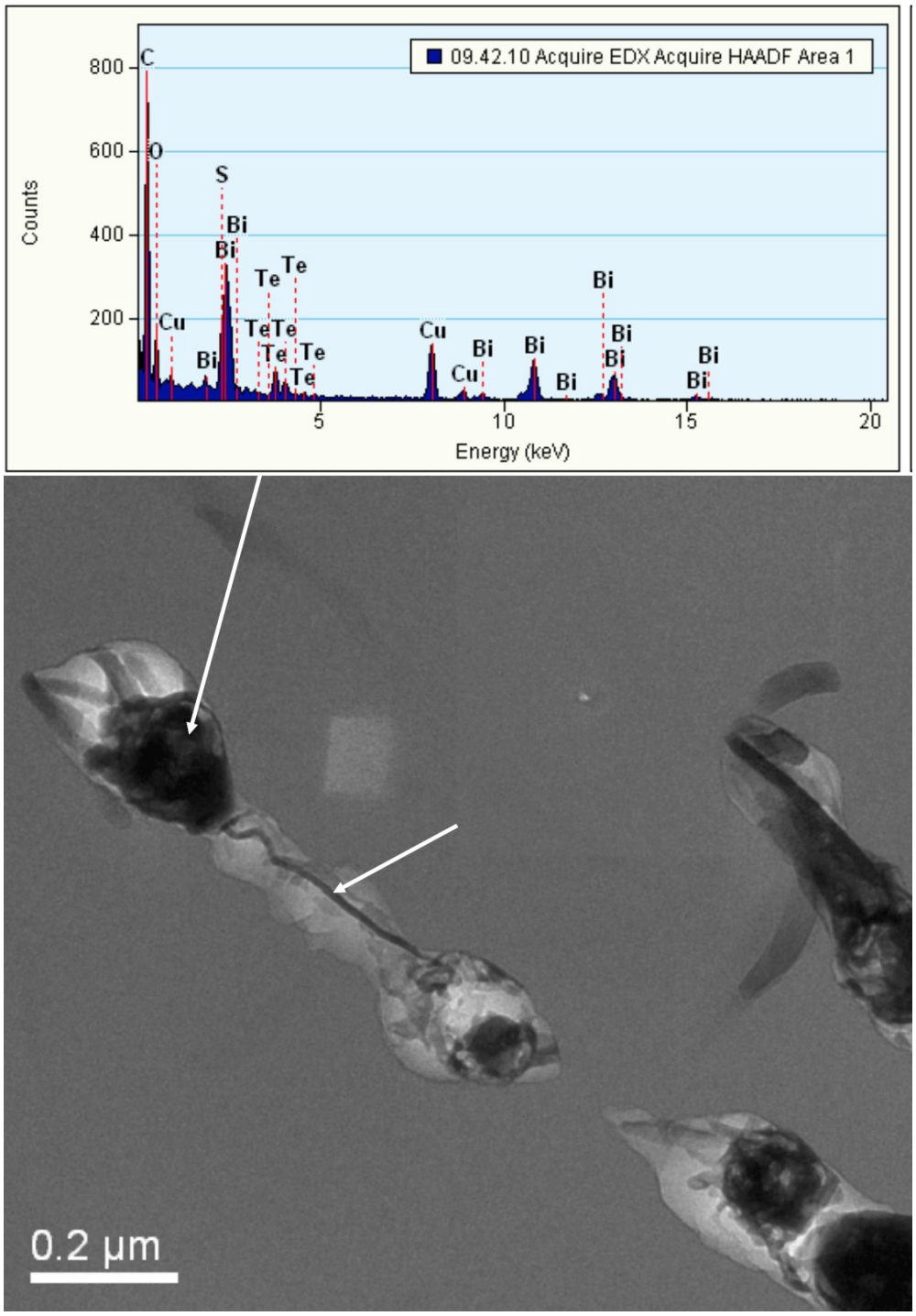

Fig. 1: TEM image and EDS analysis of biominerals in the Volyn biota. Arrows point to the location of the analysis and the thin connection of the nanoparticles.

Franz G, Lyckberg P, Khomenko V, Chournousenko V, Schulz H.-M, Mahlstedt N, Wirth R, Glodny J, Gernert U, Nissen J (2022): Fossilization of Precambrian organic matter (kerite) from the Volyn pegmatite, Ukraine. - BioGeosciences 19, 1795

Franz G, Khomenko V, Lyckberg P, Chernousenko V, Struck U, Wirth R, Gernert U, Nissen J (2023): The Volyn biota (Ukraine) – indications for 1.5 Gyr old eucaryotes in 3D-preservation, a spotlight on the 'boring billion'. - BioGeosciences 20, 1901

Liang X, Perez MAM-J, Zhang S, Song W, Armstrong JG, Bullock LA, Feldman J, Parnell J, Csetenyi L, Gadd GM (2019): Fungal formation of selenium and tellurium nanoparticles. - Appl Microbiol Biotech 103, 7241

Liang X, Perez MAM-J, Zhang S, Song W, Armstrong JG, Bullock LA, Feldman J, Parnell J, Csetenyi L, Gadd GM (2020): Fungal transformation of selenium and tellurium located in a volcanogenic sulfide deposit. Env Microbiol 22, 2346

Extreme chemical disequilibrium patterns in hydrothermal vein minerals – a case study from Columbian emeralds

G. Franz[1], V. Khomenko[1,2], F. Schiperski[1], U. Gernert[3], J. Nissen[3]

[1]Institut für Angewandte Geowissenschaften, Technische Universität Berlin
[2]Institute of Geochemistry, Mineralogy and Ore Formation, Academy of Sciences, Kyiv
[3]Zentraleinrichtung Elektronenmikroskopie Technische Universität Berlin
e-mail: gefra548@gmail.com; gerhard.franz@tu-berlin.de

Chemical zoning in metamorphic and igneous minerals has been shown to be a very powerful tool for reconstruction of pressure-temperature-time condition of growth of minerals. Vein minerals have also been in the focus because of their common occurrence with economically interesting mineralizations. Columbian emeralds formed in veins in low-grade metamorphic black shales; they are known as highly-prized gemstones and have been studied extensively over the years (e.g., Pignatelli et al. 2015; Schmetzer & Martyan 2023). We present data about their growth phenomena, from combined element distribution mappings with µ-XRF and the electron microprobe EMPA in oriented thin sections, and from scanning electron microscopy SEM.

External growth phenomena are small indentations on the basal plane (0001), which are interpreted as an expression of skeletal growth along the *c*-axis of the beryl, and rare sceptre growth. Chemical zoning shows very unusual patterns with sector zoning, which is however variable for different elements in different crystals. Sector boundaries are in some instances straight, or curved, or serrate (Fig. 1). In addition to sector zoning, stripes in the a- and c-sector were observed with alternating chemical composition. Most unusual are chemical patterns produced by the substitution Al+□(channel) = Mg+Na, with straight borders, but neither parallel nor perpendicular to the *c*-axis (Fig. 2). Another unusual feature was observed in the root zone of the crystals with cone-shaped structures extending in *c*-direction from a homogeneous zone.

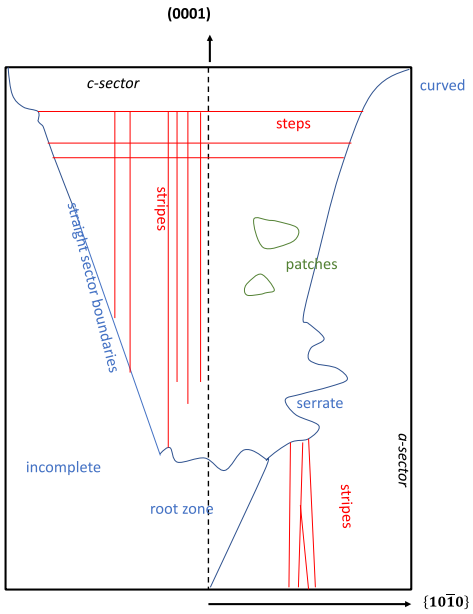

Fig. 1: Chemical zoning patterns in Columbian emerald

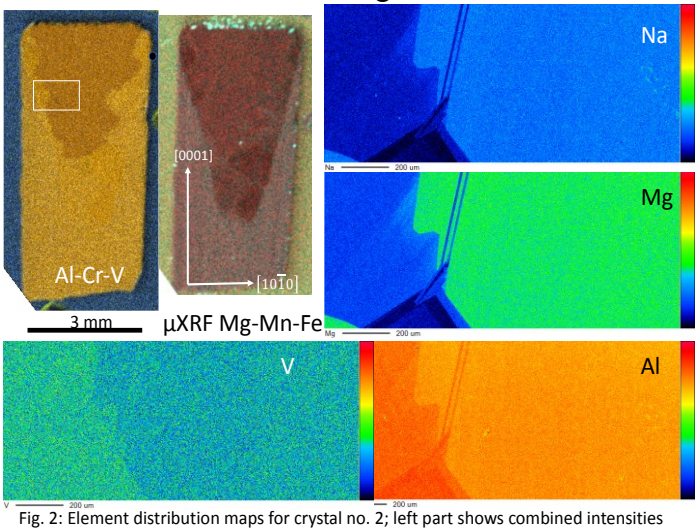

Fig. 2: Element distribution maps for crystal no. 2; left part shows combined intensities for µXRF for the whole crystal, other images results from EMPA mapping of a selected area (white frame in Al-Cr-V-mapping).

Freely grown crystals, such as beryls in open veins are often characterized by dissolution-formed etch pits. The Columbian emeralds also show such etch pits, with different shapes (rectangular, diamond-shaped), originating from point- as well as line-defects. They are typically arranged in chains, parallel and oblique to the beryl's *c*-axis (Fig. 3), what has not been observed in pegmatitic beryls (Kurumathoor & Franz 2018). These chains of etch pits point to screw-dislocation arrays and are another indication for rapid growth of the crystals. In summary, both features of growth and dissolution phenomena point to extreme disequilibrium.

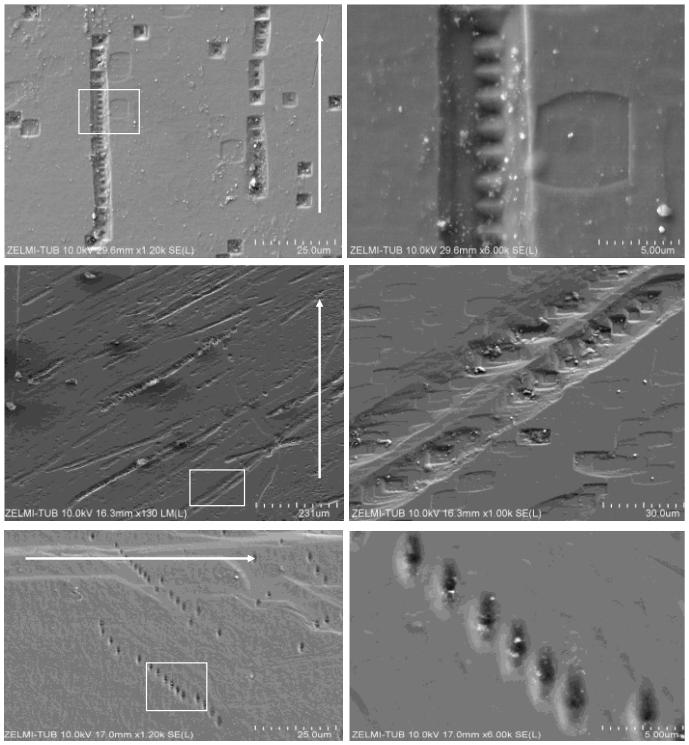

Fig. 3: SEM images of the first-order prism face of Columbian emeralds. Etch pits are arranged in chains, indicating dislocation arrays. Direction of c-axis is indicated by the arrow.

Kurumathoor R, Franz G (2018): Etch pits in beryl as indicators for dissolution behaviour. – Eur J Miner 30, 107-124

Pignatelli I, Giuliani G, Ohnenstetter D, Agrosi G, Mattheu S, Moriot C, Branquet Y (2015): Colombian trapiche emeralds: Recent advances in understanding their formation. - Gems & Gemology 51, 222-259

Schmetzer K, Martayan G (2023): Morphology of Columbian emerald: some less-common cases and their growth and dissolution history. – Gems & Gemology 59, 46-71

High-Ti Paleozoic basalts in NE Bavaria

G. Franz[1], F. Lucassen[2], F. Schiperski[1], M. Kutzschbach[1]

[1]Institut für Angewandte Geowissenschaften, Technische Universität Berlin
[2]MARUM-Center for Marine Environmental Sciences-Universität Bremen
e-mail: gefra548@tu-berlin.de; gerhard.franz@tu-berlin.de

The Paleozoic sedimentary rocks, surrounding the Münchberg Massif with its relict high-pressure nappe pile in NE Bavaria, host Ordovician to Devonian mafic volcanic and subvolcanic rocks (commonly named diabase in the German literature) that formed timely close to the deposition of the sediments. In the W and SW of the Münchberg Massif, these rocks were previously studied for age, structure and chemical composition by Höhn et al. (2018); similar rocks can be found in the E of the Münchberg Massif. Late Carboniferous granites of the Fichtelgebirge represent the next magmatic pulse, and post-Variscan mafic dikes intruded these granites as well as the metamorphic series of the Münchberg Massif.

The focus of this study is the elemental composition of stratigraphically well-defined mafic volcanic rocks from the (meta)sedimentary Thuringian facies E of the Münchberg Massif (E-domain) and post-Variscan mafic dikes from this Massif, and the Sr, Nd, and Pb isotope compositions of these mafic volcanic rocks and comparison with previously studied mafic rocks from the W domain (Höhn et al. 2018). Of special interest are the unusually high Ti-contents.

The Ordovician diabase rocks from the E and the Devonian rocks from the W are characterized by high TiO_2-contents up to almost 6 wt%, accompanied by high $Fe_2O_{3(tot)}$-contents of up to almost 20 wt%. The initial $^{87}Sr/^{86}Sr_i$ of E Ordovician samples are variable (0.7031 to 0.7107) and most initial εNd_i (+2.8 to +6.3) closely scatter around +5 irrespective the locality and without covariation of Nd and Sr isotopes. The E post-Variscan dikes show a similar range of $^{87}Sr/^{86}Sr_i$ (0.7052 to 0.7081) but, compared with E Ordovician, much lower εNd_i between -1.3 and +0.9. The W Ordovician-Silurian samples show only a small variation $^{87}Sr/^{86}Sr_i$ (0.7033 to 0.07039) and εNd_i (+2.8 to +3.4). The $^{87}Sr/^{86}Sr_i$ (0.7042 to 0.7046) of the W Devonian rocks is rather uniform, but εNd_i is variable in two clusters, + 4.8 to +6.1 and +2.3 to +2.5, that resemble the εNd_i of E and W Ordovician rocks. Initial uranogenic Pb isotope compositions of most Ordovician and Devonian samples from both domains plot in overlapping arrays above or near the crustal Pb-evolution line (Stacey and Kramers, 1975). The W Silurian rocks are different and show the highest $^{207}Pb/^{204}Pb_i$ and $^{206}Pb/^{204}Pb_i$ of the whole sample suite. The initial $^{208}Pb/^{204}Pb$ of all sample groups plot in a similar array except the Silurian samples with the two the highest and the lowest $^{208}Pb/^{204}Pb_i$ values. The E post Variscan dikes have a chemical signature which is clearly different from the Ordovician rocks.

The data are discussed in the context of the paleotectonic position of the rocks, the southern passive margin of the Rheic ocean bordering northern Gondwana or alternatively a separate Saxo-Thuringian Ocean between a Gondwana derived microcontinent and Gondwana.

Höhn S, Koglin N, Klopf L, Schüssler U, Tragelehn H, Frimmel H, Zeh A, Brätz H (2018): Geochronology, stratigraphy and geochemistry of Cambrian, Ordovician, Silurian and Devonian volcanic rocks of the Saxothuringian in NE Bavaria (Germany). – Int J Earth Sci 107, 359-377

Stacey JS and Kramers JD (1975): Approximation of terrestrial lead isotopic evolution by a two-stage model. – Earth Planet Sci Lett 26, 207-221

Enzymatically induced apatite formation as a key mechanism in fish fossilization – an experimental study

F. Gäb[1], S. Karačič[2], R. Wirth[3], G. Bierbaum[2], C. Bultmann[4]

[1]Institut für Geowissenschaften, University of Bonn,
[2]Institut für medizinische Mikrobiologie, University Hospital
[3]GFZ Potsdam
[4]Radiomed Gemeinschaftspraxis für Radiologie und Nuklearmedizin, Wiesbaden
e-mail: fgaeb@uni-bonn.de

Exceptionally preserved fish fossils are known from various locations and throughout most of Earth's history. They play an important role in understanding the history of life and process of evolution, yet the process that leads to their formation remains mostly unclear. Phosphorous is a scarce resource in the whole modern ocean and there is no evidence for this being different over the Phanerozoic. Nevertheless there are numerous examples for fish fossils preserved in apatite e.g. Solnhofen Plattenkalk (Jurassic of S' Germany), Gogo Fm. (Devonian of N' Australia) or Santana Fm. (Cretaceous of E' Brazil). Hence there is a need for a mechanism that provides exceptionally high amounts of P to facilitate the precipitation of large quantities of apatite.

In this study we investigate the role of microbially produced alkaline phosphatase (AP) as a source for the needed phosphate. AP is an ubiquitous enzyme throughout the world of bacteria and liberates phosphate from organic (macro)-molecules. It is known to provide phosphate for the formation of apatite *in vitro* (Cosmidis et al. 2015).

We conducted experiments, where AP was used to liberate phosphate from organic matter and, through oversaturation of the surrounding fluid, ultimately precipitated inorganically as apatite on fish scales. This might be the first step towards permineralization of the organic matter that is needed for fossilization. To strengthen the hypothesis the resulting apatite crystals were compared using TEM analysis with existing fossils. The result of these investigations showed a striking mineralogical similarity between the laboratory made and natural apatite crystals. This suggests that inorganic precipitation of apatite from an oversaturated solution indeed is a possible pathway for permineralization of a carcass which would ultimately lead to an exceptionally preserved fossil. Additionally this could mean that the fossil itself could be used as a geochemical and petrological indicator for the surrounding conditions, both of the sediment and the seawater, during its formation.

Cosmidis J, Benzerara K, Guyot F, Skouri-Panet F, Duprat E, Férard C, Guigner J-M, Babonneau F, Coelho C (2015): Calcium-phosphate biomineralization induced by alkaline phosphatase activity in Escherichia coli: localization, kinetics, and potential signatures in the fossil record. – Frontiers in Earth Science 3, 84

Relationships between fluid-flow, fluid-rock-interaction, and evolving microstructures in a polyphase system – results from experimental approaches using synthetic impure carbonates

J. Gätjen[1], B. Rose[1], D. Sorger[1], S. Piazolo[2], T. Müller[1]

[1]Geoscience Centre Göttingen, Georg-August-University, Germany
[2]School of Earth and Environment, The University of Leeds, United Kingdom
e-mail: jochen.gaetjen@uni-geottingen.de

In polyphase materials (e.g., porous rocks), fluid-mineral-reactions typically result in complex microstructural changes – including a spatial and temporal evolution of fluid pathways. However, a full quantitative understanding of the accompanied processes governing the development of such microstructures remains elusive. In this experimental study, we focus on the wollastonite forming reaction in a synthetic impure carbonate system with two reactants (calcite + quartz) and two products (wollastonite + CO_2) phases. This decarbonation reaction causes a negative 33 % volume change of the solid phase.

The experiments were carried out using a rapid quench cold seal apparatus. In a first step, a $CaCO_3$-SiO_2-mixture (~ 7:3) was pressurized to 0.2 GPa together with a fluid phase (~ 5 wt% H_2O, initial $X(CO_2)$ = 0.5) and heated to 600 °C for one week allowing the powder to recrystallize and anneal prior to overstepping of the reaction (initial porosity = ~ 13 vol%). In a second step, we increased the temperature (700 °C or 800 °C) to trigger the decarbonation reaction for an additional week.

Preliminary results indicate that variations in the reaction affinities govern the resulting microstructures. Experiments with conditions close to the equilibrium state (T = 700 °C, final $X(CO_2)$ = 0.56, final porosity = ~ 20 vol%) exhibit low nucleation rates in combination with relative high growth rates resulting in a slightly more porous microstructure with a few idiomorphic wollastonite grains growing in the pore space. Here, only a small amount of SiO_2 and $CaCO_3$ reacted to form $CaSiO_3$ and CO_2 as the system reached the equilibrium state due to the evolving $X(CO_2)$ fluid composition in the internally buffered system. Experiments conducted at conditions far away from the equilibrium state (T = 800 °C, final $X(CO_2)$ = 0.86) exhibit very high nucleation rates combined with comparatively low growth rates. Here, the reaction went to completion consuming all of the SiO_2 without reaching the equilibrium state. The remaining $CaCO_3$ grains are interconnected by a very porous (~ 35 vol%) nano- to microcrystalline mass of wollastonite.

Future experimental work will include piston cylinder experiments, fluid-flow experiments and time series. Quantitative orientation analysis using EBSD (Electron Backscatter Diffraction) will provide information about the micro/nano-structure of the material while serial sectioning within an SEM or NanoCT scanning will allow for porosity and permeability assessment. The experimental setup will be extended to include a mineral reaction with positive volume change (periclase + H_2O = brucite) – as well as a combination of both reaction types.

Mineral assemblage, geochemistry and geochronology of the Kawisigamuwa carbonatite, Sri Lanka

D. Gallhofer[1], E. Skrzypek[1], C.A. Hauzenberger[1], G. Auer[1], G.W.A.R. Fernando[2]

[1]Institute for Earth Sciences, University of Graz
[2]Department of Physics, The Open University of Sri Lanka
e-mail: daniela.gallhofer@uni-graz.at

The Kawisigamuwa and Eppawala carbonatites in Sri Lanka are located within upper amphibolite to granulite facies metasedimentary and metaigneous rocks of the Wanni Complex. Both occurrences have previously been interpreted as mantle-derived carbonatites, however, a recent study has shown that the Eppawala carbonatite was derived from melting of a sedimentary carbonate protolith (Wang et al. 2021). Since the origin and formation of the Kawisigamuwa carbonatite is still unclear, this study investigates its mineral paragenesis, geochemistry (XRF, EPMA, IRMS), and geochronology (LA-ICPMS).

Textural relationships indicate the following sequence of mineral formation: 1) calcite, olivine, zircon 1, phlogopite, apatite, baryte, celestine, and spinel (?) form the primary mineral assemblage, 2) dolomite, monazite, zircon 2, baddeleyite, magnetite, spinel, ilmenite, and sulfides, 3) zirconolite, allanite, and Th-rich phases and a late stage of 4) serpentinization of olivine and weathering products of Fe-oxides and other minerals.

The Kawisigamuwa carbonatite is dominated by calcite (48-51.7 wt.% CaO), has low SiO_2 (<2.3 wt.%) and P_2O_5 (<0.14 wt%) and elevated Sr (4497-4930 µg/g), La (56-188 µg/g), and Ce (164-422 µg/g) contents. Olivine has moderately high x_{Mg} (0.85-0.91) and is surrounded by reaction coronae of tremolite and/or diopside and dolomite. Phlogopite has x_{Mg} ranging from 0.88 to 0.92, elevated Ba (0.04-0.19 apfu) and moderate F (0.35-0.56 apfu) contents. Oxygen ($\delta^{18}O_{VSMOW}$ = 13.75 to 14.14) and carbon ($\delta^{13}C_{VPDB}$ = -2.73 to -2.52) isotopes of calcite from Kawisigamuwa overlap those of Epawala and are slightly lower than those of Sri Lankan marbles. Fractionation of oxygen isotopes between calcite and zircon indicate an equilibrium temperature of ~850 °C.

Geochronological data support a multi-stage evolution of the mineral assemblage at Kawisigamuwa: 1) oscillatory zoned zircon 1 yields the crystallisation age of 532.39 ± 0.66 Ma, 2) recrystallisation lead to partial resetting of U-Pb ages and formation of zircon 2 at 518 Ma or later and 3) a late stage of (re-)crystallisation is recorded by allanite (U-Pb ca.474 Ma).

While the Kawisigamuwa carbonatite shows mineral assemblages and some geochemical characteristics consistent with mantle-derived carbonatites, the mineral chemical and isotopic characteristics do not support a mantle origin. We suggest that the Kawisigamuwa carbonatite is another example of a crustal-derived anatectic carbonate body.

Wang J, Su B-X, Chen C, Ferrero S, Malaviarachchi, SPK, Sakyi, PA, Yang Y-H, Dharmapriya, PL (2021): Crustal Derivation of the ca. 475 Ma Eppawala Carbonatites in Sri Lanka. – J Petrol 62, 11, 1-18

Zircon preservation in hybrid magmas from Mt. Hasan stratovolcano, Central Anatolia, and implications for magma mixing dynamics

G. Gencoglu Korkmaz[1,2], K.A. Cionoiu[2], A.K. Schmitt[2,3]

[1]Konya Technical University, Department of Geological Engineering, Konya, Turkey
[2] Heidelberg University, Institute of Earth Sciences, Heidelberg, Germany
[3]Curtin University, John de Laeter Centre, Perth, Australia
e-mail: Gulin.Gencoglu@geow.uni-heidelberg.de

Mt. Hasan, or Hasan Dağ, is a prominent stratovolcano within the Cappadocian Volcanic Province of central Anatolia. It experienced recurrent eruptions of mostly andesitic-dacitic lava flows from its main edifice on average every 5,000 to 15,000 years over the past 100 ka (Friedrichs et al. 2020). The northeastern flank of Mt. Hasan is dissected by a strand of the Tuz Gölü fault zone (TGFZ) with significant vertical and dextral offsets that in part have displaced lava coulees erupted from the eastern vent region of Mt. Hasan (little Mt. Hasan, or Küçük Hasan Dağ) from their respective source vents (Krystopowicz 2015). The volcano is underlain by a long-lived evolved magma reservoir that has remained viable for producing explosive and effusive eruptions since at least 550 ka (Friedrichs et al. 2020). Mafic magma recharge as evident by the presence of abundant rounded enclaves in Mt. Hasan lavas and geochemical mixing trends (Aydar & Gourgaud 1998) plays an important role in maintaining the magma system viable for such protracted durations. Here, we report mineral and whole-rock geochemical results for a suite of five lava flows from the eastern part of Mt. Hasan which were sampled on both sides of the TGFZ to provide piercing points for fault reconstruction. All lava flows yielded zircon, despite whole-rock compositions and mineral temperatures being clearly outside zircon saturation conditions. The implications of this observation on the timescales and processes of magma mixing are discussed here; geochronological analysis of zircon using U-Th and (U-Th)/He methods to determine crystallization and eruptions ages, respectively, is ongoing.

The investigated lavas compositionally span from basaltic andesite to dacite. They show hypocrystalline porphyritic textures with varying amounts of glass. Basaltic andesites primarily consist of plagioclase, olivine, pyroxene, Fe-Ti oxides, and additionally quartz, which based on embayments and ocellar textures is considered xenocrystic. In the andesites, plagioclase, pyroxene, and Fe-Ti oxide minerals are commonly present, along with amphibole (often with breakdown textures), and rare olivine. Dacites, on the other hand, contain plagioclase, amphibole, pyroxene, Fe-Ti oxides, and scarce quartz microphenocrysts. Apatite and zircon are present as accessory minerals in all lavas. Plagioclase pheno-microphenocrysts in almost all investigated rocks generally show inverse and oscillatory zoning with An-contents between 33 and 70 mol% and total FeO between 0.19 and 0.75 wt%. They typically display various types of sieve textures. Amphibole is ubiquitous in the lavas, and is mostly classified as Mg-rich hornblende. However, the degree of preservation in the basaltic andesite-andesite lavas is low as indicated by intense opacification and thick breakdown rims (4–8 μm). In the dacite lavas, amphibole represents the primary mafic phase and is mostly intact. Except in the most mafic lava flow, minor amounts of biotite are present in the groundmass, typically surrounded by breakdown reaction rims. Olivine with Fo = 89–86 mol% in basaltic andesite-andesite lavas is compositionally in disequilibrium with their host. In comparison, the andesitic lavas contain olivine with lower Fo contents ranging from 79 to 84 mol%. Diopsidic augite and enstatitic orthopyroxenes are commonly present, and they are variably zoned.

Mineralogical and petrographic features of Mt. Hasan lavas indicate a hybrid nature, where evolved magmas were reheated by mafic recharge. The evolved magma resided at comparatively low temperatures in an upper crustal magma reservoir (T = 800–835 °C, P = 110–150 MPa, based on amphibole geothermobarometry using the calibration of Ridolfi (2021), whereas eruption temperatures based on Fe-Ti-oxide pairs are up to 910°C. Taking new and published data for Mt. Hasan (e.g., Aydar & Gourgaud 1998) into account, kinked trends in major element oxides variation diagrams indicate a combination of magma mixing and fractional crystallization. Magma mixing between basaltic and dacitic endmembers can explain the hybrid basaltic andesites, whereby the basaltic endmember is more primitive than the erupted compositions of Mt. Hasan as indicated by the preservation of high-Fo (Fig. 1) and high-Ni olivine in the hybrid lavas. A compositional equivalent to the mafic endmembers in these mixing scenarios are basaltic scoria cones erupted in the vicinity of Mt. Hasan (Gencoglu Korkmaz et al. 2022; Reid et al. 2017). Zircon is preserved in even the most mafic hybrid lavas, where strong undersaturation and high Zr diffusivity in the melt would nominally dissolve zircon at rates of ~10^{-11} m/s (900 °C), so that a zircon sphere 50 µm diameter would become completely resorbed by the melt within ca. 7 weeks. This implies that zircon was either shielded as inclusions in phenocrysts, or that mixing and hybridization occurred only briefly before eruption.

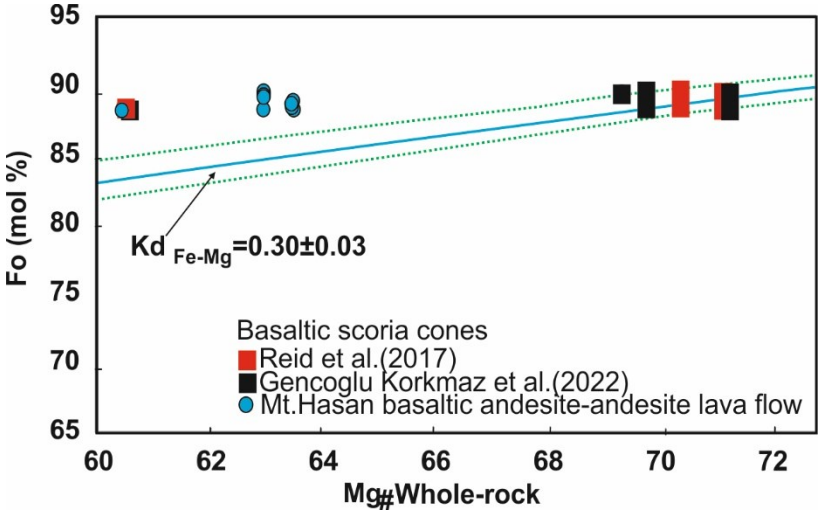

Figure 1. Whole-rock Mg≠ versus Fo (mol%) for olivine from northeastern Mt. Hasan basaltic andesite and andesite lava flows. Whole-rock and olivine compositions from scoria cones from the southwestern part of the Cappadocian Volcanic Province (Reid et al. 2017; Gencoglu Korkmaz et al. 2022) are shown for comparison.

Aydar E, Gourgaud A (1998): The Geology of Mount Hasan Stratovolcano, Central Anatolia, Turkey. - J Volcanol Geotherm Res 85, 129-152

Friedrichs B, Atıcı G, Danisik M.A, Çobankaya M, Harvey JC, Yurteri E. Schmitt AK (2020): Late Pleistocene eruptive recurrence in the post-collisional Mt. Hasan stratovolcanic complex (Central Anatolia) revealed by zircon double-dating. - J Volcanol Geotherm Res 404, 107007

Gencoglu Korkmaz G, Kurt H, Asan K, Petrelli M, Leybourne M (2022): The role of peridotite and pyroxenite melts in the origin of the Karapınar basalts, Cappadocia Volcanic Province, Central Anatolia. - J Geosci 67, 311-329

Krystopowicz NJ (2015):Constraining deformation, uplift, and activity along the Tuz Gölü fault zone, Central Anatolia, Turkey. - Master Thesis, Applied Science: University of Toronto

Reid MR, Schleiffarth WK, Cosca MA, Delph JR, Blichert-Toft J, Cooper KM (2017): Shallow melting of MORB-like mantle under hot continental lithosphere, Central Anatolia. - Geochem Geophys Geosyst 18, 1866-1888

Ridolfi F (2021): Amp-TB2: An updated model for calcic amphibole thermobarometry.- Minerals 11, 324

Eveslogite – Decoding the complexity of eveslogite through three-dimensional electron diffraction

E. Götz[1], M. Klementová[2], W. Depmeier[3], S. V. Krivovichev[4,5], M. Czank[3], M. Schowalter[6], L. Palatinus[2], U. Kolb[1,7]

[1]Institute of Applied Geosciences, Geomaterial Science, Technical University of Darmstadt, Germany
[2]Department of Structure Analysis, Institute of Physics of the Czech Academy of Sciences, Prague, Czech Republic
[3]Institute of Geosciences, Kiel University, Germany
[4]Kola Science Centre, Russian Academy of Sciences, Apatity, Russia
[5]Department of Crystallography, St. Petersburg State University, St. Petersburg, Russia
[6]Institute of Solid State Physics, University of Bremen, Germany
[7]Centre for High-Resolution Electron Microscopy, Johannes Gutenberg University, Mainz, Germany
e-mail: Emilia.goetz@tu-darmstadt.de

Eveslogite is an exceptionally complex mineral, found exclusively at Mt. Eveslogchorr, located in the Khibiny alkaline massif, Kola peninsula, Russia. It occurs as a late-hydrothermal formation in veins breaching a poikilitic nepheline syenite, called rischorrite. Despite its discovery in 2003, the structure of eveslogite remained elusive due to its intricacies and the limitations of available methods and instruments at that time (Men'shikov et al. 2003). It was originally thought that the structure resembled that of a heterophyllosilicate (Ferraris & Gula, 2005), but doubts regarding the applicability of the modular approach arose after the crystal structure of a similar mineral, yuksporite, was determined (Krivovichev et al., 2004).

To overcome these challenges, advanced techniques such as three-dimensional electron diffraction (3DED; Gemmi et al., 2019) was used to determine the structure and high-angle annular dark-field scanning transmission electron microscopy (HAADF-STEM) was employed to verify it. These methods allowed the investigation of the eveslogite structure at the nanoscale, as the small crystal size and complex twinning prevented the use of traditional X-ray diffraction techniques. Additionally, energy dispersive X-ray spectroscopy (EDS) provided valuable insights into the elemental composition of the mineral.

Contradictory previous findings (Men'shikov et al., 2003) new cell parameters were proposed (a = 14.2359 Å, b = 44.8242 Å, c = 15.9058 Å, α = 90°, β = 109.658°, γ = 90°, with a cell volume of 9558.08 Å^3) and the space group $P2_1$ was unambiguously assigned. This revised cell facilitated the structure determination of eveslogite, which comprises 345 symmetrically independent atom positions [see Figure 1(A)]. Based on the average elemental composition the sum formula of eveslogite is $K_{17.5}(Ba,Sr)_8(Na,Ca)_{40}[(Ti,Nb,Fe,Mn)_{11}Si_{62}O_{179}(OH,F)_{12}(O,OH)_{13}](H_2O)$. The essential building blocks that make up the eveslogite structure are heterosilicate tubular chains (see Figure 1(B) and (C)) as well as double-tubes (see Figure 1(D) and (E)), extending along the a-axis. Zig-zag rows of the tubular building units are interconnected by ribbons of $(Ca,Na)O_x$ polyhedra likewise extending along [100]. The heterosilicate tubular building units of eveslogite show a certain degree of similarity with silicate-only modules occurring in charoite and denisovite (Rozhdestvenskaya et al., 2010; Rozhdestvenskaya et al., 2017). Additional diortho-silicate groups are always connected with the heteroatoms. The double-tubes consist of unbranched dreier double silicate chains connected via (Ti,Nb,Fe,Mn)-heterocations (M) to diortho-silicate groups, resembling the structure of yuksporite. Notably, the M positions form MO_6 octahedra or MO_5 square pyramids within the double-tubes.

The findings of this research shed light on the complex structure of eveslogite, emphasizing the importance of avoiding twinning and acquiring data from single nm-sized crystals using 3DED. This study not only contributes to a deeper understanding of this remarkable mineral but also showcases the power of advanced electron microscopy techniques in unravelling the intricate structures of minerals.

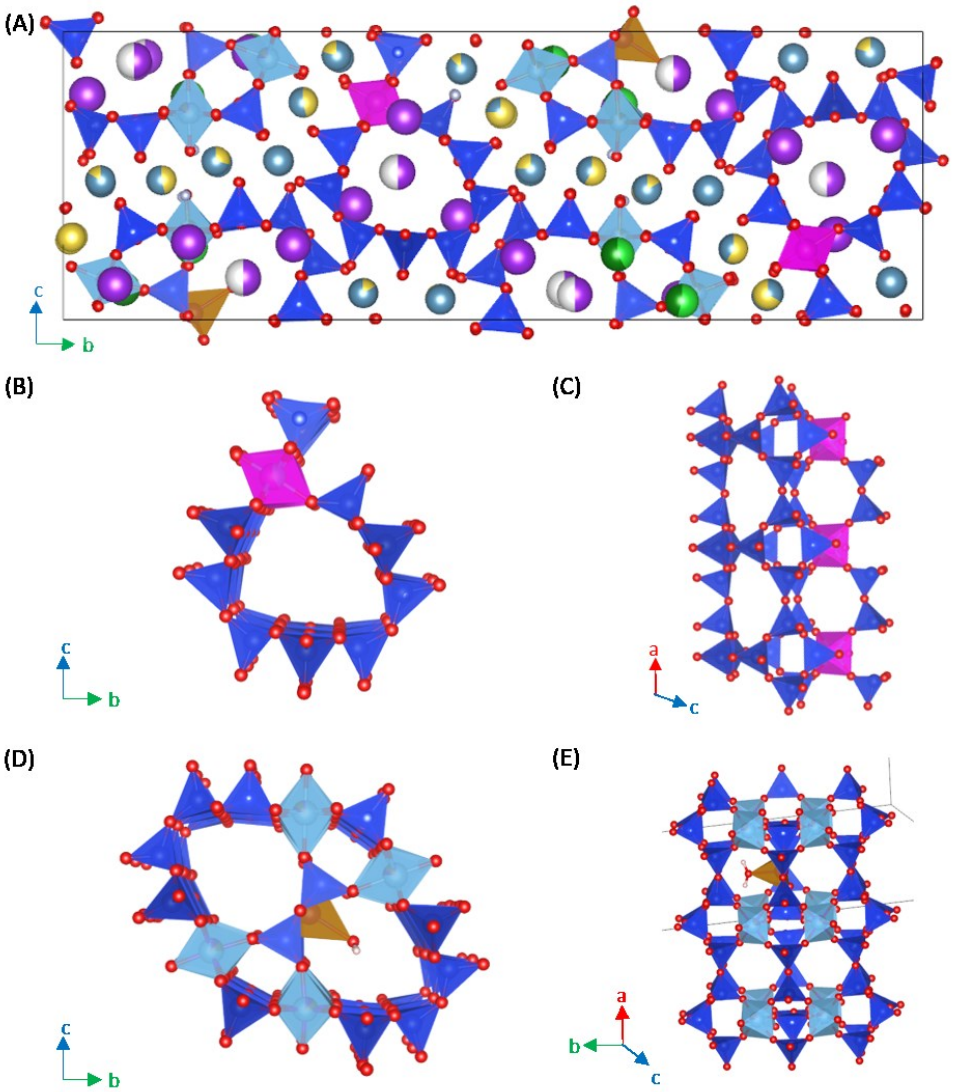

Figure 1: (A) Structure of eveslogite along [100]. The unit cell is marked by a black box. The heterosilicate tubular chains are shown along [100] in (B) and along the [010] in (C). (D) and (E) show the double-tube along [100] and along [329], respectively. Si is displayed in dark blue, M in light blue, (Ti,Nb) in pink, (Fe,Mn) in orange, Ba in light green, Sr in dark green, K in purple, Ca in blue-grey, Na in yellow, O in red, F in grey and H in white

Ferraris G, Gula A (2005): Polysomatic aspects of microporous minerals – heterophyllosilicates, palysepioles and rhodesite-related structures. – Rev Min Geochem 57, 69-104

Gemmi M, Mugnaioli E, Gorelik TE, Kolb U, Palatinus L, Boullay P, Hovmoller S, Abrahams JP (2019): 3D electron diffraction: The nanocrystallography revolution. – ACS Central Science 5, 1315-1329

Krivovichev SV, Yakovenchuk VN, Armbruster T, Döbelin N, Pattinson P, Weber H-P, Depmeier W (2004): Porous titanosilicate nanorods in the structure of yuksporite, $(Sr,Ba)_2K_4(Ca,Na)_{14}(Mn,Fe)\{(Ti,Nb)_4(O,OH)_4[Si_6O_{17}]_2[Si_2O_7]_3\}(H_2O,OH)_n$, resolved using synchrotron radiation. – Amer Min 89, 1561-1565

Men'shikov Y, Khomyakov A, Ferraris G, Belluso E, Gula A, Kulchitskaya E (2003): Eveslogite, $(Ca,K,Na,Sr,Ba)_{24}[(Ti,Nb,Fe,Mn)_6(OH)_6Si_{24}O_{72}](F,OH,Cl)_7$, a new mineral from the Khibina alkaline massif, Kola Peninsula, Russia. – Zap Vseross Mineral Obshch 132, 59-67

Rozhdestvenskaya IV, Mugnaioli E, Czank M, Depmeier W, Kolb U, Reinholdt A, Weirich T (2010): The structure of charoite, $(K,Sr,Ba,Mn)_{15-16}(Ca,Na)_{32}[Si_{70}(O,OH)_{180}](OH,F)_4.nH_2O$, solved by conventional and automated electron diffraction. - Min Mag 74, 1, 159-177

Rozhdestvenskaya IV, Mugnaioli E, Schowalter M, Schmidt MU, Czank M, Depmeier W, Rosenauer A (2017): The structure of denisovite, a fibrous nanocrystalline polytypic disordered 'very complex' silicate, studied by a synergistic multi-disciplinary approach employing methods of electron crystallography and X-ray powder diffraction. - IUCrJ 4, 3, 223-242

A machine learning force field for albite and the diffusion mechanisms of its defects

A. Gorfer[1,2], R. Abart[2], C. Dellago[1]

[1]Faculty of Physics, University of Vienna, Boltzmanngasse 5, 1090, Vienna, Austria
[2]Department of Lithospheric Research, University of Vienna, Josef-Holaubuek-Platz 2, 1090, Vienna, Austria
e-mail: alexander.gorfer@univie.ac.at

Feldspar is the most abundant mineral in the Earth's crust and the nature of its diffusive phase transformations are essential for reconstructing the thermal histories of magmatic and metamorphic rocks. Due to the large timescales over which these transformations proceed, the mechanism responsible for sodium diffusion and its possible anisotropy has remained a topic of debate. To elucidate the process, we have developed a machine learning force field (MLFF) (reviewed in Unke et al. 2022) trained on first-principle calculations of Albite (Na-feldspar) and its charged defects.

The MLFF has been trained to accurately predict a range of experimental macroscopic properties as well as defect formation energies, incorporating electrostatic corrections of the underlying first-principle calculation. Notably, we have discovered a new type of dumbbell interstitial defect, which is found to be the most favorable interstitial, and its formation free energy at finite temperature has been computed using thermodynamic integration.

Using the force field to drive molecular dynamics (MD) simulations allowed us to gain unprecedented insight into the diffusion mechanisms, as depicted in Figure 1. Through the analysis of jump rates, diffusion coefficients and tracer correlation factors we have determined that correlation plays a significant role, particularly in the $\perp(010)$ direction due to a distinct dumbbell/interstitialcy mechanism. Moreover, we have observed a high degree of anisotropy in diffusion, with variations up to 27-fold at 1000K, as illustrated in Figure 2. The strong agreement between our results and experimental diffusion coefficients leads us to conclude that MLFFs represent a mature and powerful methodology for investigating the dynamical properties of feldspar and other silicates.

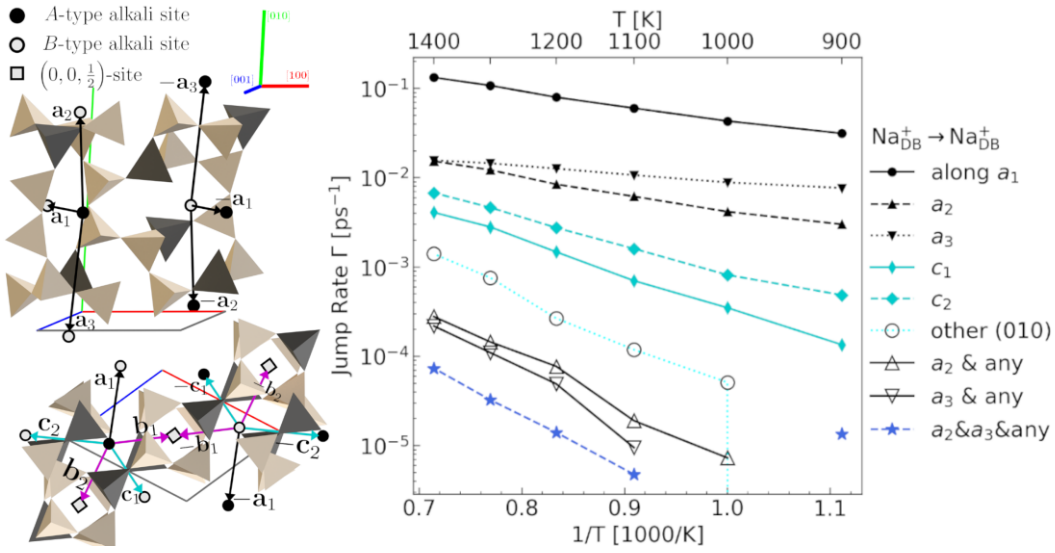

Figure 1. Left: diffusion pathways connecting the different sites. Right: jump rates for paths between alkali sites measured during an MD simulation using the MLFF. The dominance of diffusion along $\mathbf{a}_{1,2,3}$ leads to the high anisotropy.

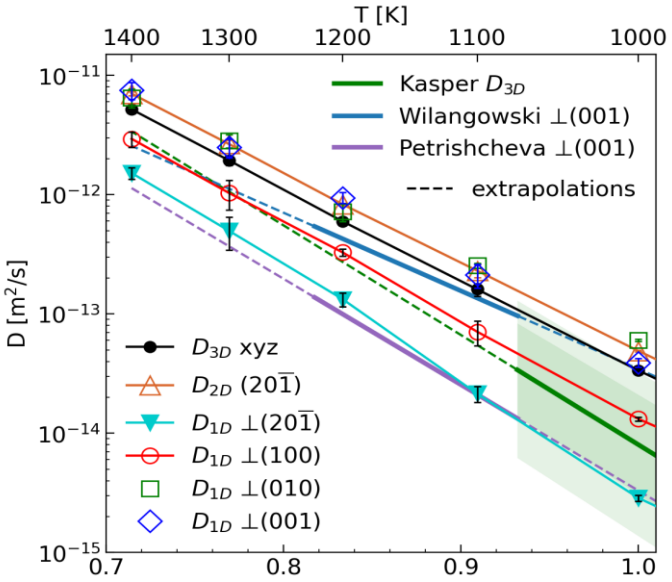

Figure 2. Diffusion coefficients for an interstitial defect measured over all dimensions D_{3D} and projected onto two D_{2D} or one dimension D_{1D} including experimental data of Kasper (1975), Wilangowski et al. (2015), and Petrishcheva et al. (2020)

Unke O, Chmiela S, Sauceda E, Gastegger M, Poltavsky I, Schütt K, Tkatchenko A, Müller KR (2021): Machine Learning Force Fields. - Chem Rev 121 (16), 10142-10186

Kasper RB (1975): Cation and Oxygen Diffusion in Albite - Ph.D. Thesis, Brown University.

Wilangowski F, Divinski S, Abart R, Stolwijk NA (2015) (1962): Radiotracer experiments and Monte Carlo simulation of sodium diffusion in alkali feldspar: evidence against the vacancy mechanism. - Defects Diffus Forum 363, 79–84

Petrishcheva E, Tiede L, Heuser D, Hutter H, Giester G, Abart R (2020): Multicomponent diffusion in ionic crystals: theoretical model and application to combined tracer- and interdiffusion in alkali feldspar. - Phys Chem Minerals 47, 35

Redox processes and metal sources recorded by Se and S isotopes of black smoker sulfides and host rocks

A. Grosche [1], M. Keith[1], R. Klemd[1], H. Strauss[2], S. König[3]

[1]GeoZentrum Nordbayern, Friedrich-Alexander-Universität Erlangen-Nürnberg, Schlossgarten 5, 91054 Erlangen, Germany
[2]Institut für Geologie und Paläontologie, Westfälische Wilhelms-Universität Münster, 48149 Münster, Germany
[3]Instituto Andaluz de Ciencias de la Tierra (IACT), Consejo Superior de Investigaciones Científicas (CSIC) and Universidad de Granada (UGR), Avenida las Palmeras 4, Armilla, 18100 Granada, Spain
e-mail: anna.grosche@fau.de

Black smoker chimneys are products of submarine hydrothermal venting and have a complex internal zoning that is the result of mineral precipitation and maturation at evolving fluid conditions. The composition of the hydrothermal sulfides is thereby controlled by the fluid composition (e.g., temperature, pH, salinity), processes like fluid boiling, and the potential input of magmatic fluids. Advances in analytical techniques allow the quantitative analysis of stable isotope ratios of heavy elements, such as Se, which can provide new insights into the cycling of chalcophile elements in magmatic-hydrothermal systems (König et al. 2019; Rosca et al. 2022).

We sampled different zones of black smoker chimneys from the Nifonea vent field (New Hebrides Arc, W Pacific) from the inner chalcopyrite lining towards the outer rim. Homogeneous sulfide powders were analyzed for high-precision Se isotopes using a double spike and hydride generation sample introduction system attached to a ThermoFisher Scientific® *NeptuneXT*™ MC-ICP-MS at the IACT, Granada. Fractions of the same powders were also analyzed for S isotopes and the resulting data was combined with in-situ trace element data of genetically related sulfides.

The $\delta^{82/76}$Se values (relative to NIST-3149) of chimney sulfides range from -3.7 ‰ to 0.6 ‰ ± 0.2 ‰ (2SD) (Fig. 1), in accordance with previously reported values of seafloor hydrothermal sulfides (Rouxel et al. 2004). The δ^{34}S values (relative to VCDT) range between 2.1 ‰ and 4.0 ‰ reflecting typical mixing of H_2S derived from the host rocks and from thermochemical seawater sulfate reduction lacking any evidence for magmatic fluid input. The highest $\delta^{82/76}$Se values occur in chalcopyrite that precipitated from high temperature fluids (370 °C) and overlap with $\delta^{82/76}$Se values of fresh basaltic glass from the surrounding Nifonea caldera (Fig. 1). This suggests that metals were leached from the host rocks and that no significant isotope fractionation occurred during high temperature precipitation of chalcopyrite.

Decreasing Se/Tl and Co/Tl ratios of pyrite from the inner to the outer chimney wall record a temperature decrease. A coupled decrease of $\delta^{82/76}$Se and δ^{34}S values towards the outer and low temperature zones (Fig. 1) can be related to local temperature-dependent isotope fractionation during redox reactions induced by mixing of the hydrothermal fluid with seawater. Understanding Se isotope fractionation during hydrothermal sulfide precipitation is crucial to subsequently identify the metal sources and the effect of fractionation processes in the upflow zone of submarine hydrothermal systems.

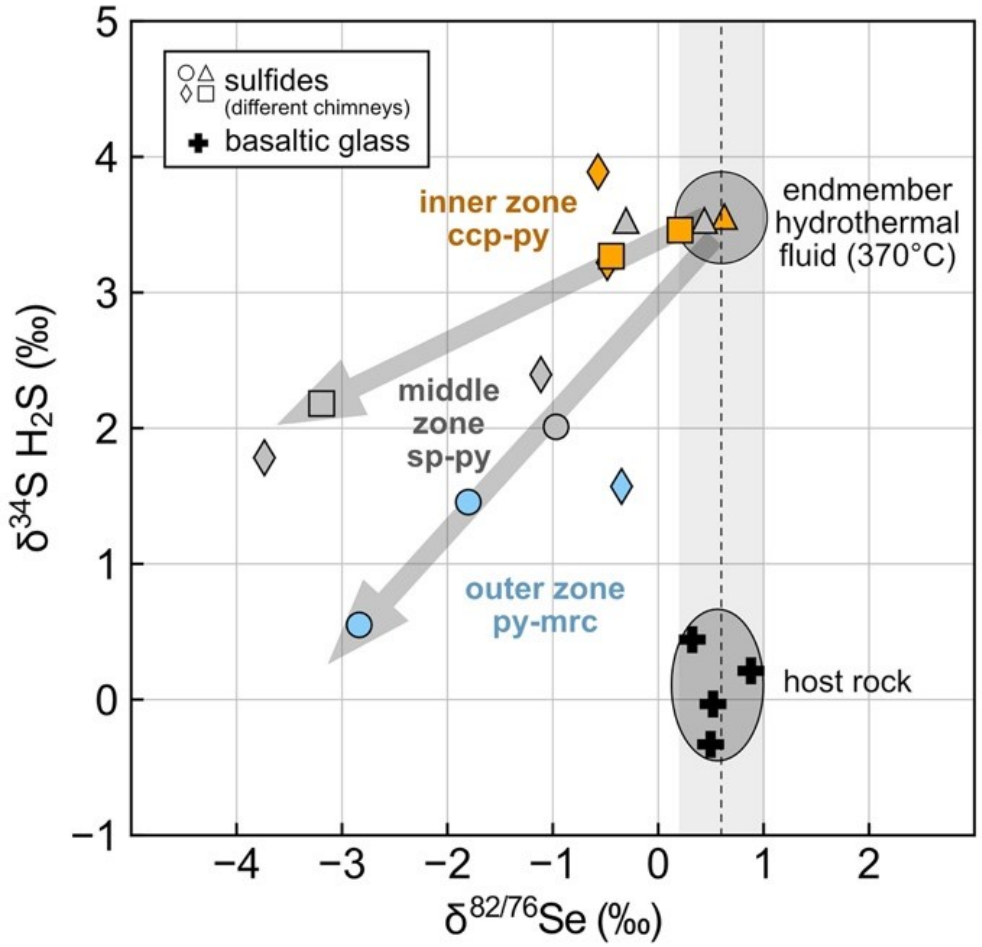

Figure 1. $\delta^{82/76}$Se (relative to NIST-3149) versus δ^{34}S (relative to VCTD) values of black smoker sulfides and volcanic glass from Nifonea. The colors indicate whether the sulfide powder was derived from the inner, middle, or outer chimney zone. The symbols mark different vent sites. The δ^{34}S values of H_2S were calculated from the δ^{34}S value of the sulfide powder using the equilibrium isotopic fractionation factors by Ohmoto & Rye (1979) for the dominant sulfide phase at estimated fluid temperatures of 370°C (inner zone), 270 °C (middle zone), and 200 °C (outer zone). ccp = chalcopyrite, py = pyrite, sp = sphalerite, mrc = marcasite.

König S, Eickmann B, Zack T, Yierpan A, Wille M, Taubald H, Schoenberg R (2019): Redox induced sulfur-selenium isotope decoupling recorded in pyrite. - Geochim Cosmochim Acta 244, 24–39

Ohmoto H, Rye RO (1979): Isotopes of sulfur and carbon. - In: Barnes HL (ed) Geochemistry of Hydrothermal Ore Deposits. J Wiley and Sons, 509-567

Rouxel O, Fouquet Y, Ludden JN (2004): Subsurface processes at the Lucky Strike hydrothermal field, Mid-Atlantic Ridge: Evidence from sulfur, selenium, and iron isotopes. - Geochim Cosmochim Acta, 68, 2295–2311

Rosca C, Vlastélic I, Varas-Reus MI, König S (2022): Isotopic constraints on selenium degassing from basaltic magma and near-surface capture by fumarolic deposits: Implications for Se redistribution onto the Earth's surface. - Chem Geol 596, 120796

Real structure of mineral kenyaite, $Na_2Si_{20}O_{40}(OH)_2 \cdot 8\ H_2O$

I. Grosskreuz[1], B. Marler[1]

[1]*Dept. of Geology, Minerlogy and Geophysics, Ruhr University Bochum; Germany*
e-mail: isabel.grosskreuz@rub.de

Only very few natural occurrences of the rare mineral kenyaite are known. Named after Kenya, the country where the first sample had been discovered, kenyaite is known since 1967 with a composition of the type material $NaSi_{11}O_{20.5}(OH)_4 \cdot H_2O$ according to Hans Eugster [1]. Different compositions, however, have been determined due to the fact that i) a part of the sodium cations can easily be leached from the structure with water and ii) the content of structural water seems to depend on the relative humidity and temperature of the environment and/or the pre-treatment of the sample prior to chemical analysis. The structure of kenyaite remained hidden for a long time because of very small crystals, a complex structure and a certain degree of structural disorder. Only in 2021, the crystal structure of synthetic kenyaite was published [2]. Kenyaite is a layered silicate and belongs to the group of Hydrous Layer Silicates (HLSs) [3] similar to minerals kanemite [4], $Na_4[H_4Si_8O_{20}] \cdot 12\ H_2O$, magadiite [5], $Na_2[Si_{14}O_{26}(OH)_6] \cdot 6\ H_2O$, and makatite [6], $Na_8[Si_{16}O_{32}(OH)_4] \cdot 16\ H_2O$.

Experimental data: Natural kenyaite samples from Lake Magadi were kindly provided by K. Beneke and G. Lagaly, Kiel, Germany. In all samples, kenyaite was associated with either magadiite, quartz or both phases. For structure analysis, a fairly well crystalline sample (Fig. 1) was chosen which contained quartz as an impurity. Powder XRD data were recorded in modified Debye-Scherrer geometry using $CuK\alpha_1$ radiation. The average structure of kenyaite was refined using the FullProf 2K program [7].

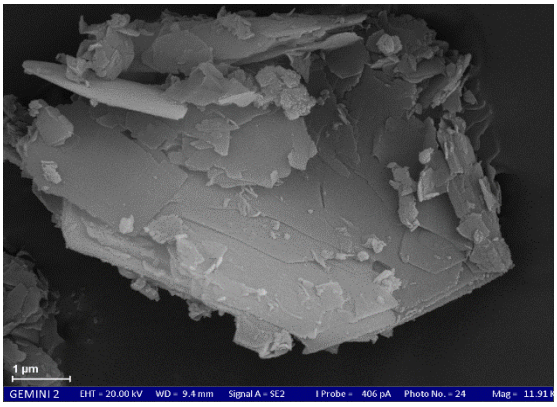

Fig. 1: Plate-like morphology of kenyaite crystals.

Subsequently, the disordered real structure was studied by comparing experimental powder XRD patterns with simulated ones calculated with the program DIFFaX [8]. In order to simulate the broadened reflections in the XRD powder diagram illustrating the disorder, various structure models were constructed based on a stacking disordered arrangement of layers.

The average structure

Nearly identical to synthetic kenyaite, the structure of the kenyaite mineral contains thick silicate layers (thickness: 15.9 Å) and bands of edge-sharing $[Na(H_2O)_{6/1.5}]$ octahedra which are intercalated between these layers (Fig. 2). The dense layers (six layers [3]) have the same topology as the layers of RUB-6 [9] and synthetic kenyaite and possess a high silicon Q^4 to Q^3 ratio of 4.0. One half of the terminal ≡Si-O units form silanol groups (≡Si-OH) while the other half forms siloxy groups (≡Si-O^-) to compensate the charge of the sodium cations. Interestingly, quite strong hydrogen bonds (d(O···O) = approx. 2.5 Å) exist (confirmed by ^{1}H MAS NMR spectroscopy) between the terminal silanol/siloxy groups themselves as intra-layer interactions, but also between the silanol/siloxy groups and water molecules of the octahedra.
The kenyaite mineral crystallizes with space group symmetry *F*2*dd* (No. 43, setting 3) and lattice parameters a = 10.604(1) Å, b = 10.080(1) Å, c = 79.383(8) Å.

Analysis of the real structure

The structure of kenyaite is slightly disordered typical for hydrous layer silicates which possess only weak ionic interactions between the alternating blocks of silicate layers and cations (in this case: $Na(H_2O)_{6/1.5}$ octahedra). The silicate layers of kenyaite (six layers) and inter-layer regions containing the octahedra are stacked perpendicular to the ***ab***-plane.

The type of stacking disorder was investigated in detail by calculating hypothetical powder diagrams corresponding to various stacking sequences. The regular (average) structure of kenyaite possesses an ordered ABCD… stacking sequence of identical six layers with a sequence of shift vectors of 0.5 *a* + 0.5 *b* => -0.5 *a* + 0.5 *b* => 0.5 *a* + -0.5 *b* => 0.5 *a* + 0.5 *b* between successive layers. In addition, successive layers are rotated by 90° against each other (Fig. 2). However, other shift vectors are also possible (e.g., 0.25 *a* + 0.25 *b* **or** -0.25 *a* + 0.25 *b*) without distortion of structural building blocks. Figure 3 shows a comparison between the experimental PXRD diagram and simulated diagrams.

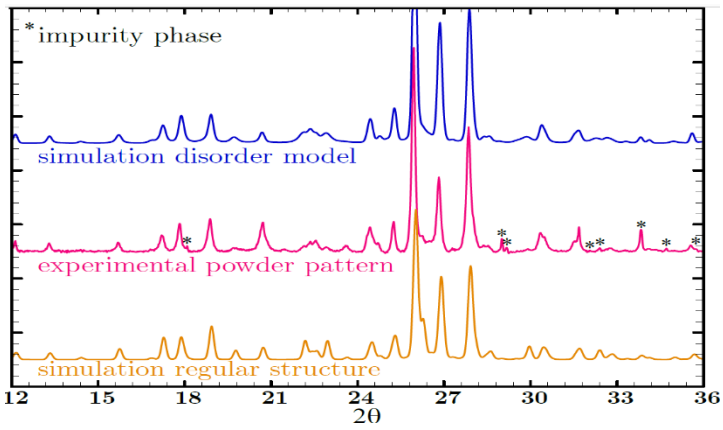

Fig. 3: Section of the experimental PXRD diagram of mineral kenyaite (quartz subtracted) and the simulated diagrams of the regular and disordered structure.
* indicate reflections of the impurity phase Trona.

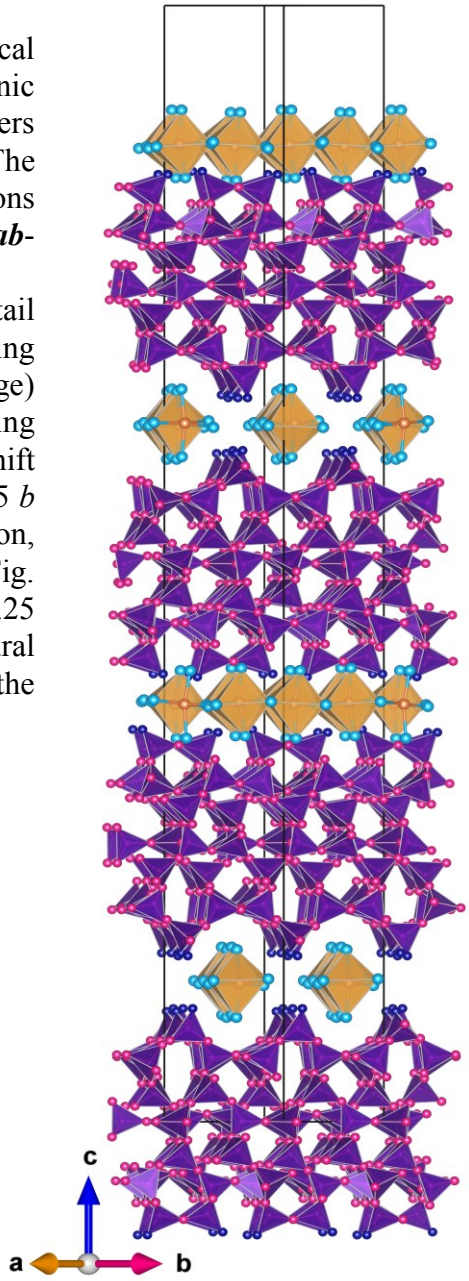

Fig. 2: Average structure of mineral kenyaite.

[1] Eugster HP (1967): Hydrous sodium silicates from Lake Magadi, Kenya: precursors of bedded chert. - Science 157 (3793) 1177–1180

[2] Marler B, Großkreuz I, Gies H (2021): The crystal structure of synthetic kenyaite, $Na_2Si_{20}O_{40}(OH)_2 \cdot 8\ H_2O$. - J Solid State Chem 300, Article No. 122215

[3] Marler B, Grünewald-Lüke A, Ikeda T, Zuber P, Heimes H, Gies H: Database of hydrous layer silicates - https://www.hls-database.com

[4] Vortmann S, Rius J, Marler B, Gies H (1999): Structure solution from powder data of the hydrous layer silicate kanemite, a precursor of the industrial ion exchanger SKS-6. - Eur J Mineral 11 125–134

[5] Marler B, Krysiak Y, Grosskreuz I, Gies H, Kolb U (2022): The crystal structure of mineral magadiite, $Na_2Si_{14}O_{28}(OH)_2 \cdot 8\ H_2O$. - Amer Mineral 107, 211-2110

[6] Annehed H, Faelth L, Lincoln LJ (1982): Crystal structure of synthetic makatite $Na_2Si_4O_8(OH)_{2.4} \cdot H_2O$. - Z Kristallogr 159, 203–210

[7] Rodríguez-Carvajal J (1993): Recent advances in magnetic structure determination by neutron powder diffraction. - Physica B: Condensed Matter 192, 55–69

[8] Treacy MMJ, Deem MW, Newsam JM: *DIFFaX*, https://www.public.asu.edu/~mtreacy/DIFFaX.html

[9] Krysiak Y, Marler B, Barton B, Plana-Ruiz S, Gies H, Neder RB, Kolb U (2020): New zeolite-like RUB-5 and its related hydrous layer silicate RUB-6 structurally characterized by electron microscopy. - IUCrJ 7, 522-534

Origin of ultramafic rocks associated with carbonatites and their bearing on the formation of HFSE-deposits

D. Gudelius[1, 2, 3] *, M. W. Marks[3], G. Markl[3], T. F. D. Nielsen[4], J. Kolb[1, 2], B. Walter[1, 2]

[1]Karlsruhe Institute of Technology, Chair of Geochemistry and Economic Geology, Institute for Applied Geosciences, Adenauerring 20b, 76131 Karlsruhe, Germany
[2]Laboratory for Environmental and Raw Materials Analysis (LERA), Adenauerring 20b, 76131 Karlsruhe, Germany
[3] Eberhard Karls University, Institute of Geosciences, Schnarrenbergstrasse 94-96, 72076 Tübingen, Germany
[4] Geological Survey of Denmark and Greenland, Department of Petrology and Economic, 16 Geology, Øster Voldgade 10, Copenhagen, Denmark
e-mail: b.walter@kit.edu

Many carbonatites occur together with large amounts of ultramafic rocks, melilitolites, foidolites and (foid)syenites. There is an ongoing debate if and how these contrasting lithologies were formed by differentiation of a common, mantle-derived silicate magma or rather by metasomatic processes between carbonatite and country rocks (Vasyukova & Williams-Jones, 2022). In order to find petrological evidence for one or the other, two key examples, the Gardiner (E Greenland) and Kovdor (Russia) complexes are compared in this study (Fig. 1). Despite their similar tectonic setting and succession of rock types, they show significant differences in the texture and mineral composition of ultramafic rocks.

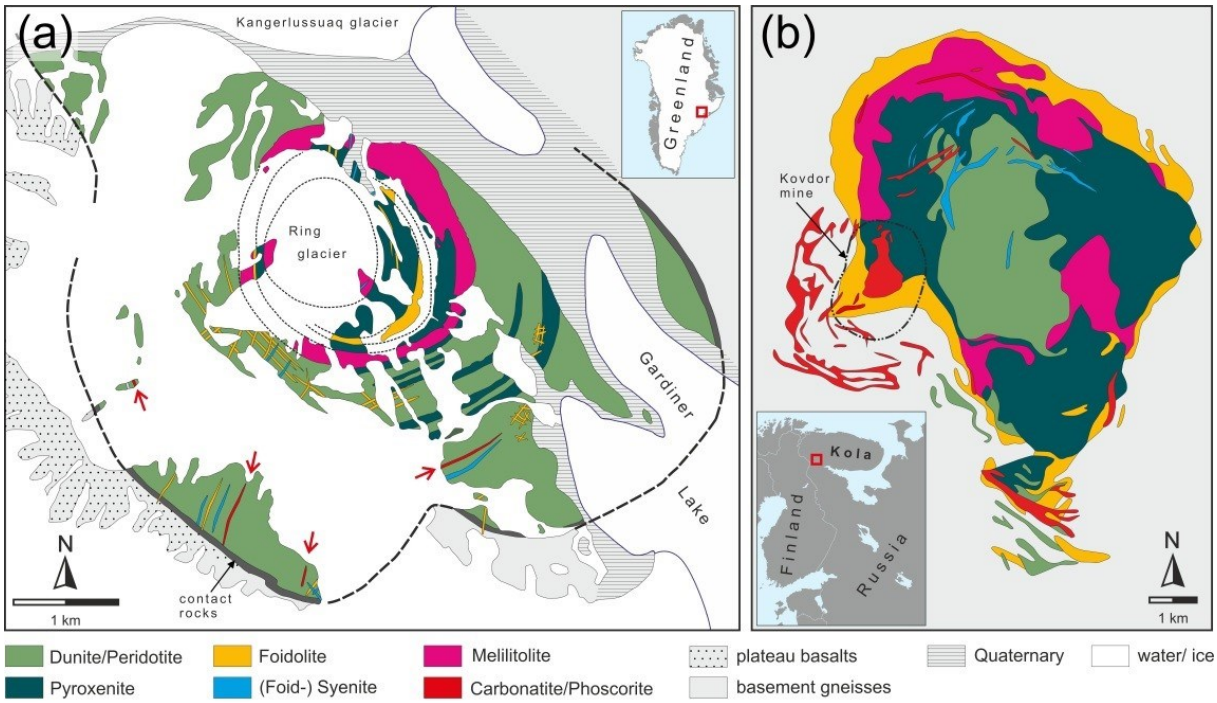

Figure 1: Geological maps of (a) Gardiner (E Greenland) and Kovdor (Russia), taken from Gudelius et al. (2023).

Ultramafic rocks from Kovdor include calcite- and biotite-rich dunites and pyroxenites without typical cumulate textures. They partly consist of Ni-poor forsterite (Fig. 2), Cr-poor diopside and Ni-Cr-poor spinel and are therefore interpreted as metasomatic reaction products between mantle-derived carbonatite melts and silicic host rocks. Similar ultramafic rocks are associated with carbonatites (e. g. at Palabora - South Africa, Afrikanda - Russia, and Salitre - Brazil). In contrast, the ultramafic rocks from Gardiner show well-preserved cumulate textures and consist

of Ni-rich forsterite, Cr-rich diopside as well as Cr-Ni-Ti-rich spinel and also contain F-Cl-rich apatite.

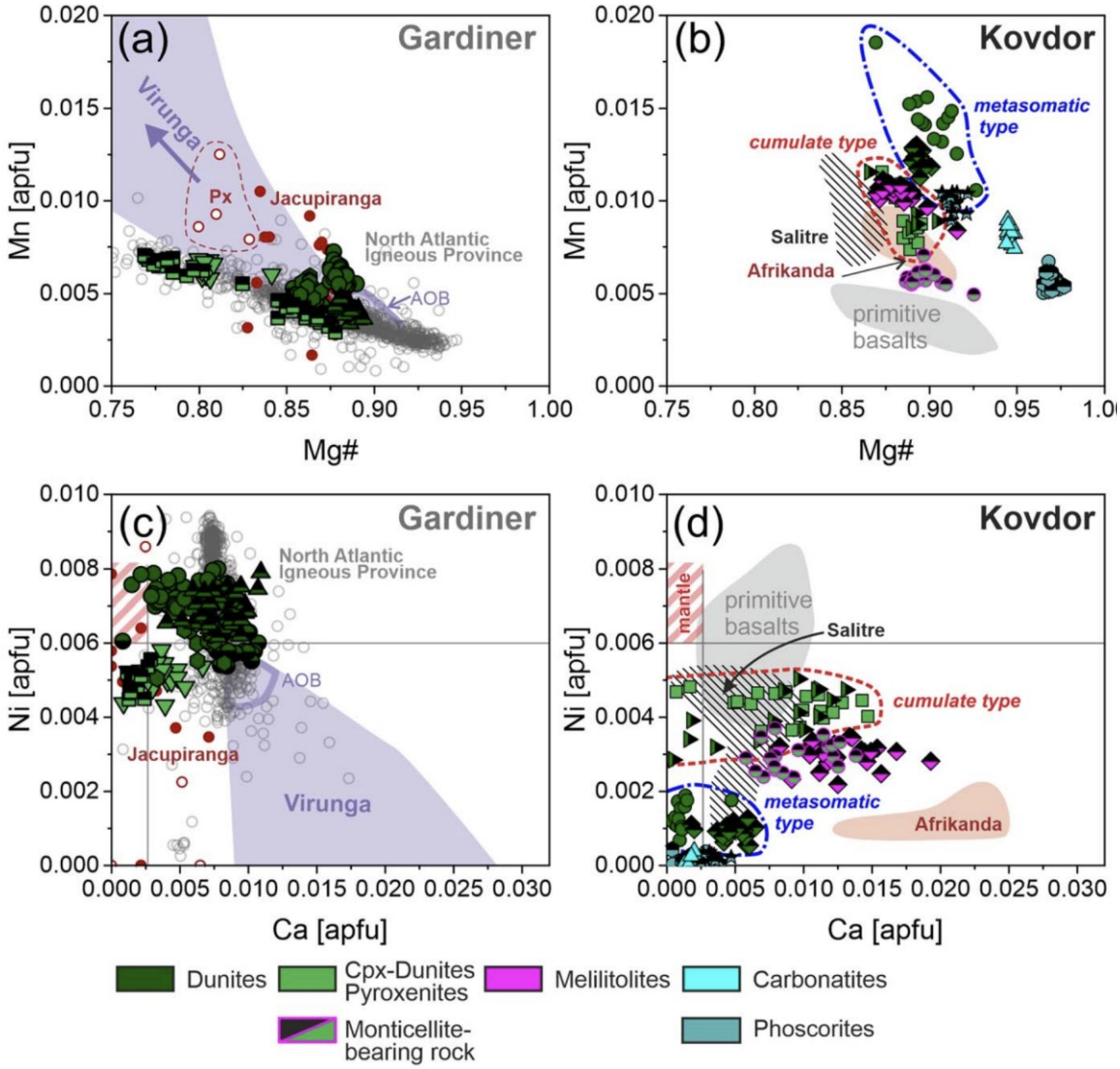

Figure 2: Comparison of olivine compositions from Gardiner (left column) and Kovdor (right column) with literature data (taken from Gudelius et al. 2023)

This indicates that these rocks represent cumulates of an evolving, mafic melt derived from Ti-rich mantle source, similar to other rocks of the North Atlantic igneous province (Fig. 2). In contrast to systems dominated by carbonatite metasomatism like Kovdor, Ti-rich parental silicate magmas can abundantly crystallize Ti phases, as recorded by massive perovskite cumulates in Gardiner melilitolites. This can effectively scavenge HFSE from the magmatic system early in its evolution and likely explains HFSE-barren carbonatites at Gardiner, while those from Kovdor are highly HFSE-enriched. In summary, ultramafic rocks in alkaline complexes can be of both cumulate and metasomatic origin; the specific type has an important bearing on their HFSE enrichment and on the types of ores present in such complexes.

Gudelius, D., Marks, M. W., Markl, G., Nielsen, T. F., Kolb, J., Walter, B. (2023): The origin of ultramafic complexes with melilitolites and carbonatites: a petrological comparison of the Gardiner (E Greenland) and Kovdor (Russia) intrusions. - J Petrol, egad036

Vasyukova, O.V. & Williams-Jones, A.E. (2022): Carbonatite metasomatism, the key to unlocking the carbonatite–phoscorite–ultramafic rock paradox. - Chem Geol 602, 120888